Spectral-domain Optical Coherence Tomography on a Silicon Chip

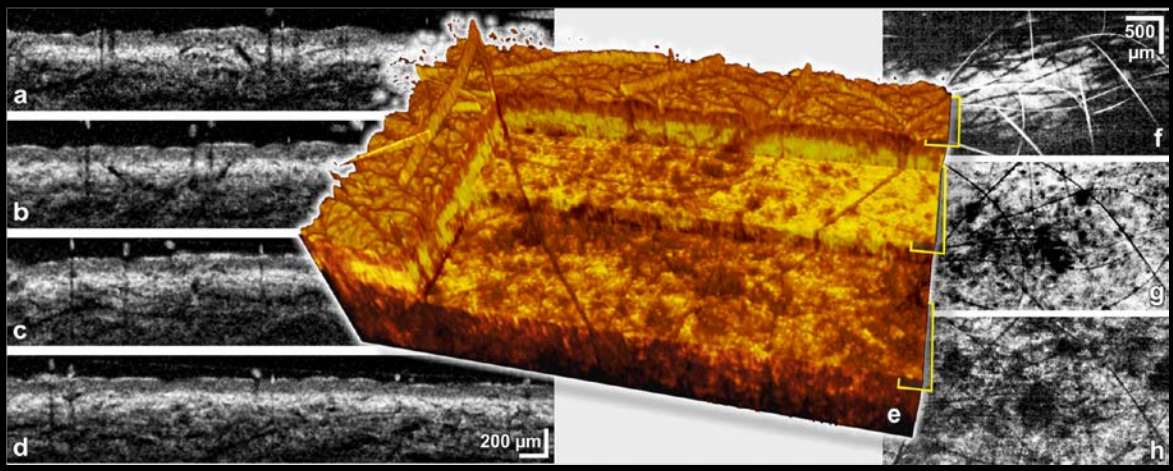

B. İMRAN AKÇA

Spectral-domain Optical Coherence Tomography on a Silicon Chip

B. İMRAN AKÇA

Graduation committee:

Chairman and secretary:

Prof. Dr. Ir. A. J. Mouthaan	University of Twente

Promoter:

Prof. Dr. M. Pollnau	University of Twente

Assistant promoter:

Dr. Ir. R. M. de Ridder	University of Twente

Members:

Prof. Dr. Atilla Aydınlı	Bilkent University
Prof. Dr. Wolfgang Drexler	Medical University of Vienna
Prof. Dr. Ir. Wiendelt Steenbergen	University of Twente
Assoc. Prof. Dr. Ir. Cees Otto	University of Twente

The research described in this thesis was carried out at the Integrated Optical MicroSystems (IOMS) Group, Faculty of Electrical Engineering, Mathematics and Computer Science, MESA+ Institute for Nanotechnology, University of Twente, P.O. Box 217, 7500 AE, Enschede, The Netherlands. It was financially supported funding through the Smartmix "Memphis" program of the Dutch Ministry of Economic Affairs.

Front cover: The OCT image of human skin taken by the developed on-chip SD-OCT system.

Back cover: 3D schematic illustration of the on-chip SD-OCT system.

Printed by

ISBN 978-90-365-3478-9
DOI 10.3990./1.9789036534789
URL http://dx.doi.org/10.3990/1.9789036534789

SPECTRAL-DOMAIN OPTICAL COHERENCE TOMOGRAPHY ON A SILICON CHIP

DISSERTATION

to obtain
the degree of doctor at the University of Twente,
on the authority of the rector magnificus,
prof. dr. H. Brinksma
on account of the decision of the graduation committee,
to be publicly defended
on Wednesday the 5th of December 2012 at 12:45

by

BAKİYE İMRAN AKÇA
born on the 1th of June 1982
in Aksaray, Turkey

This dissertation is approved by:
the promoter: Prof. Dr. M. Pollnau
the assistant promoter: Dr. R. M. de Ridder

…to my husband, my parents, and my country

"If A equals success, then the formula is:
A = X + Y + Z, X is work, Y is play, Z is keep your mouth shut"

Albert Einstein

Contents

List of Abbreviations

AWG	Arrayed waveguide grating
AW	Arrayed waveguide
BS	Beam splitter
BPM	Beam propagation method
CCD	Charge coupled device
CT	Computerized tomography
dB	Decibel
DC	Directional coupler
FD	Frequency domain
FPR	Free propagation region
FSR	Free spectral range
FT	Fourier transform
FWHM	Full width at half maximum
GVD	Group velocity dispersion
LCI	Low coherence interferometry
LPCVD	Low-pressure chemical vapor deposition
MI	Michelson interferometer
MRI	Magnetic resonance imaging
MZI	Mach-Zehnder interferometer
NA	Numerical aperture
OLCR	Optical low-coherence reflectometry
OCT	Optical coherence tomography
PECVD	Plasma-enhanced chemical vapor deposition
PM	Polarization maintaining
RIE	Reactive ion etching
SD	Spectral domain
SEM	Scanning electron microscope
SiON	Silicon oxynitride
SLD	Superluminescent diode
SNR	Signal to noise ratio
SS	Swept source
TE	Transverse-electric
TEOS	Tetraethyl orthosilicate
TM	Transverse-magnetic
TO	Thermo-optic
WDM	Wavelength-division multiplexing

WG	Waveguide

List of Figures

List of Tables

Preface

This dissertation is written as a partial fulfillment of the requirements to obtain the PhD degree at the University of Twente (UT). The PhD project was carried out at the Integrated Optical MicroSystems (IOMS) Group, MESA+ Institute for Nanotechnology, Faculty of Electrical Engineering, Mathematics and Computer Science (EEMCS) at UT in the period from the 1st of January 2009 to the 31st of December 2012.

The PhD project was financially supported funding through the Smartmix "Memphis" program of the Dutch Ministry of Economic Affairs and the Netherlands Ministry of Education, Culture and Science. The supervisors for the project were:

Professor Markus Pollnau, IOMS – UT
Promoter

Assistant Professor René M. de Ridder, IOMS – UT
Assistant promoter

Assistant Professor Kerstin Wörhoff, IOMS – UT
Supervisor

Abstract
Spectral-domain Optical Coherence Tomography on a Silicon Chip

Optical coherence tomography (OCT) is a non-invasive optical technique for high-resolution cross-sectional imaging of specimens, with many applications in clinical medicine and industry (e.g. materials testing, quality assurance, and process control). Current state-of-the-art OCT systems operate in the frequency-domain, using either a broad-band light source and a spectrometer, known as "spectral-domain OCT" (SD-OCT), or a rapidly tunable laser, known as "swept-source OCT" (SS-OCT). Both systems contain a multitude of fiber and free-space optical components which make these instruments costly and bulky. The size and cost of an OCT system can be decreased significantly by the use of integrated optics. A suitable fabrication technology and optimum design may allow one to fabricate extremely compact, low-cost, and rugged OCT systems. The main goal of this PhD project is miniaturization of an SD-OCT system by integrating its spectrometer and interferometer parts on a silicon chip. For this purpose an arrayed-waveguide grating (AWG) spectrometer and a Michelson interferometer (MI) comprising wavelength-insensitive 3-dB couplers were designed, fabricated, and characterized.

Although integration of a spectrometer on a chip is challenging, AWGs present a well-established way towards miniaturization. Besides their extensive usage in telecommunication for (de)multiplexing, AWGs are also ideally suited for applications such as OCT and spectroscopy, with their high spectral resolution, small form factor, large bandwidth, and low insertion loss. In addition to their advantages listed above, AWGs are cost-effective, which makes them favorable for integration with SD-OCT systems.

Wavelength-insensitive 3-dB couplers can be realized by either cascading two conventional couplers in a Mach-Zehnder configuration with a relative phase shift of $2\pi/3$ introduced between them (i.e. balanced coupler) or using two adiabatically tapered asynchronous waveguides (i.e. non-uniform adiabatic coupler). Such couplers can be designed to yield a maximally flat response with respect to deviations in wavelength, polarization, or uniform fabrication over a broad spectral range, with no excess loss. Therefore, these couplers are very good candidates for application in MIs.

In the first chapter of this thesis an overview is given of OCT systems. In chapter 2, the background, design, fabrication, and characterization of AWG spectrometers and their applications in OCT imaging are discussed. In chapter 3,

integrated MIs and wavelength-insensitive 3-dB couplers are presented; here, two different coupler designs (non-uniform adiabatic and balanced couplers) are analyzed in detail. The OCT measurements at 800 nm and 1300 nm are presented in chapter 4. Results of depth-range enhancement and polarization effect on signal roll-off are presented in chapter 5. In addition, an integrated field-flattening lens design and its characterization are discussed as a part of chapter 5 as well. In chapter 6, conclusions and outlook, based on the results presented in this thesis, are given.

1 Introduction

1.1 Optical coherence tomography (OCT) and its applications

Medical imaging refers to several different technologies, including magnetic resonance imaging (MRI), computerized tomography (CT), ultrasound, confocal microscopy, and optical coherence tomography (OCT), that are used to image (parts of) the human body for disease diagnosis, treatment planning, and surgical guidance [Dha10]. Their performance is often limited by a trade-off between the resolution and penetration depth. Table 1.1 provides an overview of the resolution and penetration depth of typical imaging methods. Among the aforementioned imaging methods, MRI and CT can provide the largest depth range (>50 cm) with the lowest resolution (~1 mm) which only allows the investigation of structures in a human body at the organ level. Ultrasound provides a large depth range (~15 cm) with poor resolution (~150 µm) whereas confocal microscopy offers higher resolution (~1 µm) for smaller depth ranges (~200-500 µm). OCT can typically acquire images of structures a few millimeters (~2-3 mm) deep within a sample with a resolution better than 10 µm, which fills the gap between ultrasound and confocal microscopy [Dha10].

OCT is an extension of optical low-coherence domain reflectometry (OLCR) which is a one-dimensional optical ranging technique based on low-coherence interferometry (LCI). It was first developed for measuring reflections in fiber optics and optoelectronic devices [You87]; in the following years the transverse scanning capability enabled cross-sectional imaging, i.e., OCT [Hua91]. OCT is a non-invasive optical technique for high-resolution cross-sectional imaging of, among other things, biological tissue, with many applications in clinical medicine.

OCT has been used to obtain images of several different kinds of biological tissue, such as skin, teeth, muscles, and others. The first OCT images were of the human retina and coronary arteries [Hua91]. To date, the most significant clinical impact of OCT has been in the field of ophthalmology. However in the past decade, applications in OCT have expanded into other medical fields such as gastroenterology [Tea97a], gynecology [Pit99], pulmonology [Pit98], urology [Tea97b, Lis10], cardiology [Bre96], and oncology [Jun05].

In this thesis the on-chip OCT systems are intended to be used in dermal and retinal (ophthalmic) imaging which necessitates two different designs depending

upon the wavelength range (i.e. 800 nm for retinal imaging and 1300 nm for dermal imaging).

Table 1.1: *Typical performance of principal biomedical imaging methods.*

Imaging methods	Average resolution	Maximum depth range
MRI	1 mm	>50 cm
CT	1 mm	>50 cm
Ultrasound	150 µm	15 cm
Confocal microscopy	1 µm	200-500 µm
OCT	< 10 µm	2-3 mm

1.2 Organization of the thesis

This thesis consists of 6 chapters:

Chapter 1: The remainder of this chapter will introduce the theory of OCT, starting from fundamentals of interferometry, and will briefly discuss the different types of OCT systems. System specifications related to design parameters such as axial resolution, imaging depth range, and sensitivity roll-off will be presented. The miniaturization of OCT systems and the pertaining integrated optics components will be discussed.

Chapter 2: The theory, design, fabrication, and characterization of AWG spectrometers will be presented. Performance-enhanced novel AWG designs, including cascaded AWG systems and broad-band flat-top AWGs will be discussed

Chapter 3: This chapter will discuss the integrated Michelson interferometer (MI) design consisting of wavelength insensitive 3-dB couplers. The theory, design, fabrication, and characterization of two different wavelength-insensitive 3-dB couplers, namely adiabatic and balanced couplers will be presented.

Chapter 4: Performance characterization of the 800-nm and 1300-nm OCT systems consisting of the AWG spectrometers and as well as the integrated MIs will be presented with *in vivo* image demonstrations. The measurement set-ups and the measurement procedure will be discussed.

Chapter 5: This chapter will discuss the performance improvement of the OCT systems in terms of depth range and polarization. Additionally, a new flat-focal-field AWG design using an integrated field-flattening lens will be presented.

Chapter 6: The final chapter will present the general conclusions of the thesis and the prospective discussion of future work and directions for possible developments of the on-chip OCT systems.

The work of this PhD project will/has produced 6 journal papers based on
Chapter 2, 3, and 4: B. I. Akca *et al.*, Optics Letters, 2011,
B. I. Akca *et al.*, Journal of Selected Topics in Quantum Electronics, 2012,
B. I. Akca *et al.*, Optics Express, 2012,
B. I. Akca *et al.*, in preparation.
Chapter 5: B. I. Akca *et al.*, Photonics Technology Letters, 2012,
B. I. Akca *et al.*, Optics Letters, 2012,

1.3 Working principle of OCT

The working principle of OCT is based on LCI which is commonly performed using a MI as depicted in Fig. 1.1. The MI consists of a light source, a beam splitter, two mirrors and a detector. Light emitted from the light source is divided by the beam splitter between the two arms of the interferometer. The reflections from the sample and reference arms merge at the beam splitter and are directed towards the detector. The superimposed waves produce interference fringes on the detector. These distinctive fringes enable one to determine the location at which light is reflected back and to measure the depth profile of the scattering amplitude. By performing multiple LCI measurements at different lateral coordinates on a sample, a three-dimensional cross-sectional image of the scattering amplitude can be constructed. For a low-coherence broadband light source, the interference fringes appear when the path length mismatch is within the coherence length of the light source.

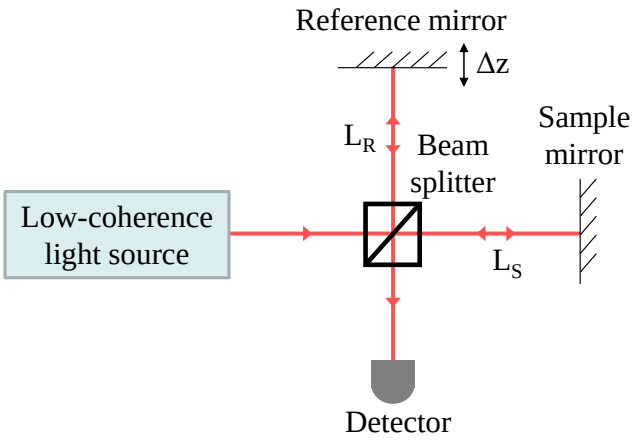

Fig. 1.1 Schematic diagram of a free space Michelson interferometer (MI).

The functional form of the interference signal of an MI using a monochromatic (single wavelength) light source is also applicable for the LCI using a broad bandwidth light source, however it requires some modifications. Light emitting from a monochromatic light source can be described as a plane wave propagating in the *z*-direction (omitting the explicit harmonic time dependence $e^{j\omega t}$)

$$E_{in} = E_0 e^{-jkz}, \tag{1.1}$$

where E_O is the amplitude of the field, k is the (angular) wavenumber ($k=2\pi/\lambda$), z is the optical propagation distance, ω is the angular frequency. The fields in the sample and reference arms, E_S and E_R respectively, are then

$$E_S = E_s e^{-jk(2L_S)}, \tag{1.2}$$

$$E_R = E_r e^{-jk(2L_R)}, \tag{1.3}$$

where E_s and E_r are the amplitudes of the field in the sample and reference arms after reflecting off the mirrors, L_S and L_R are the optical path lengths of the sample and reference arms, respectively, and j is the imaginary unit.

Optical detectors are square law intensity detection devices, where the recorded intensity is proportional to a time average of the electric field multiplied by its complex conjugate. The intensity of the interference signal can be written as

$$I_D \propto \left\langle \left| E_R + E_S \right|^2 \right\rangle = \left\langle (E_R + E_S)(E_R{}^* + E_S{}^*) \right\rangle$$
$$= \left\langle E_R E_R{}^* \right\rangle + \left\langle E_S E_S{}^* \right\rangle + \left\langle E_R{}^* E_S \right\rangle + \left\langle E_R E_S{}^* \right\rangle, \quad (1.4)$$

where $E_S{}^*$ and $E_R{}^*$ denote the complex conjugate of the fields in the sample and the reference arms, respectively and the angled brackets denote a time-average. Rearranging Eq. (1.4) yields

$$I_D = E_r{}^2 + E_s{}^2 + E_r E_s e^{jk2(L_R - L_S)} + E_r E_s e^{jk2(L_S - L_R)}, \quad (1.5)$$

With the use of the trigonometry identity $cos(\theta) = (1/2)[exp(j\theta) + exp(-j\theta)]$ Eq. (1.5) becomes

$$I_D = E_r{}^2 + E_s{}^2 + 2E_r E_s \cos(2k\Delta L), \quad (1.6)$$

where

$$\Delta L = L_R - L_S, \quad (1.7)$$

ΔL is the mismatch in distance between the reference and sample beam paths. The first two terms in Eq. (1.6) can be identified as self-interference (DC component), whereas the last term is the cross-interference (AC component). The interference signal varies periodically with ΔL.

Equation (1.6) gives a general formula for the MI using a monochromatic light source. To introduce LCI, using a broad bandwidth source, this formula needs to be modified slightly. The electric fields from the sample (E_S) and reference (E_R) arms can be represented as functions of frequency

$$E_S(\omega) = E_s(\omega) e^{-jk_s(\omega)2L_S}, \quad (1.8)$$

$$E_R(\omega) = E_r(\omega) e^{-jk_r(\omega)2L_R}, \quad (1.9)$$

The light intensity at angular frequency ω is

$$I_D \propto \left\langle \left| E_S(\omega) + E_R(\omega) \right|^2 \right\rangle$$
$$= \left| E_S(\omega) \right|^2 + \left| E_R(\omega) \right|^2 + 2\,\mathrm{Re}\left\{ E_R(\omega) E_S{}^*(\omega) \right\} \quad (1.10)$$

The last term (cross) provides the interference signal at ω. A low-coherence source can be represented as the sum of monochromatic sources, therefore the interference signal at all angular frequencies will be

$$I_D = 2\,\mathrm{Re}\left\{\int_{-\infty}^{\infty} E_R(\omega)E_S{}^{*}(\omega)d\omega\right\}, \tag{1.11}$$

Substituting Eq. (1.8) and Eq. (1.9) into Eq. (1.11) we obtain

$$I_D = 2\,\mathrm{Re}\left\{\int_{-\infty}^{\infty} E_r(\omega)E_s{}^{*}(\omega)e^{-j\Delta\varphi(\omega)}d\omega\right\}, \tag{1.12}$$

$$\Delta\varphi(\omega) = 2k_s(\omega)L_S - 2k_r(\omega)L_R$$

1.4 Types of OCT systems

Essentially there are two main types of OCT systems; time-domain (TD) OCT and frequency-domain (FD) OCT as depicted in Fig. 1.2. Although the operating mechanisms of TD-OCT and FD-OCT systems differ, the basic principle is the same. Both methods measure the interference of light reflected from the specimen with light reflected from a reference mirror. TD-OCT measures a path-length difference by observing white-light interference (all frequencies of the source simultaneously) as a function of the position of the reference mirror which is translated as a function of time. Depth resolution is obtained because interference only occurs when the path-length difference is within the coherence length of the light source. FD-OCT uses a fixed-position reference mirror, and resolves the interference as a function of light frequency. The depth structure can be reconstructed by observing that the interference fringes for different frequencies have different spacings, which translates into a frequency-dependent intensity distribution at a given z-location. This results in a superior sensitivity and speed performance of FD-OCT systems over TD-OCT systems.

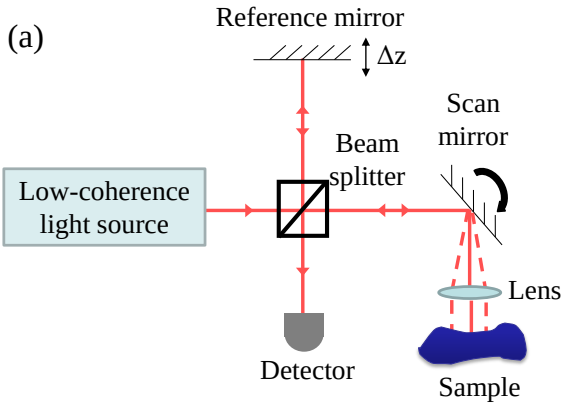

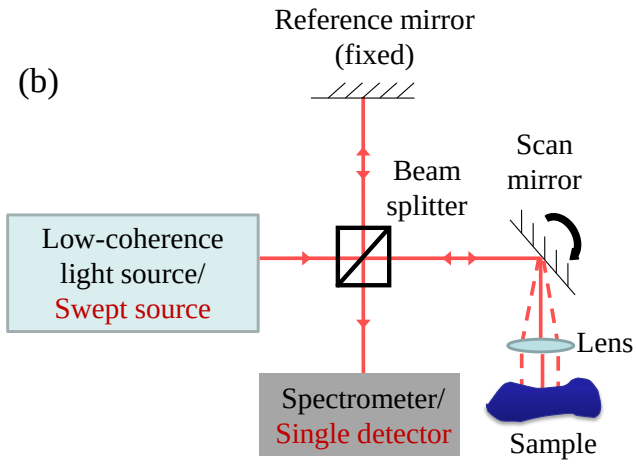

Fig. 1.2 Schematic diagram of **(a)** time domain optical coherence tomography (TD-OCT) and **(b)** Frequency domain optical coherence tomography (FD-OCT). The method involving a swept-source and a single detector is called swept-source optical coherence tomography (SS-OCT), whereas the method using a broadband source and a spectrometer is called spectral domain optical coherence tomography (SD-OCT).

Current state-of-the-art OCT systems operate in the frequency-domain, using either a broad-band light source and a spectrometer, known as "spectral-domain OCT" (SD-OCT), or a rapidly tunable laser, known as "swept-source OCT" (SS-OCT) as shown in Fig. 1.2(b). FD-OCT systems (SS-OCT and SD-OCT) were invented by Fercher et al. in 1995 [Fer95]. However, FD-OCT gained wide acceptance only after nearly 10 years, when it was realized that FD-OCT offered a significant sensitivity advantage over TD-OCT due to the long acquisition time of TD-OCT systems.

In SD-OCT systems the reference mirror is stationary, and the interference pattern is split by a grating into its frequency components and all of these components are simultaneously detected by linear detector. SS-OCT systems extract this spectral information by using a frequency scanning (tunable) light source. For both systems the depth profile (z-coordinate) of the sample is retrieved from the detected signal by performing a Fourier transform (FT) from k to z domain as shown in Fig. 1.3. The signal processing steps of an SD-OCT system are depicted in Fig. 1.4. The acquired spectra are processed by subtracting the reference-arm spectrum, i.e. the spectrum acquired from reference arm when sample arm is blocked, and resampling to k-space. FT algorithms yield accurate transforms when the sampling interval of the input data is constant. Most of the

spectrometers sample the light in evenly spaced intervals of wavelength (λ). However, the relevant FT pair for FD-OCT is space (x) and wavenumber (k), which is inversely proportional to wavelength ($k=2\pi/\lambda$). OCT data collected at evenly spaced wavelength intervals are thus unevenly spaced in k; hence, if the data are not re-sampled to be evenly spaced in wavenumber rather than wavelength prior to using the FT, the reconstructed axial profile will be severely degraded and suffer from inaccuracies.

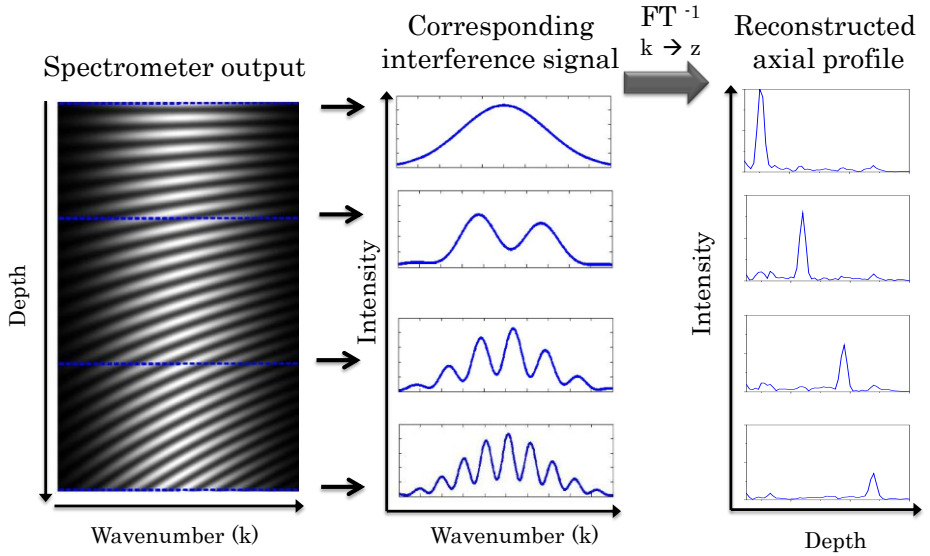

Fig. 1.3 Reconstruction of the depth profile in SD-OCT systems. Higher-frequency oscillation in the k domain, corresponding to reflections at deeper locations, have decreasing amplitudes in the detected intensity, even though the reflected powers from these locations are the same. This phenomenon, which is called signal roll-off, is discussed in section 1.5.

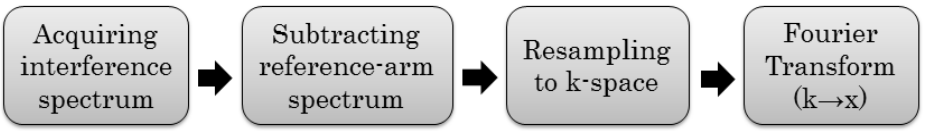

Fig. 1.4 Signal processing steps for SD-OCT.

SS-OCT systems are advantageous for their simple single-element detection and better sensitivity with imaging depth (lower sensitivity roll-off), but they typically have a lower axial resolution compared to SD-OCT due to limited bandwidth of the available tunable light sources [Zah05]. In addition, they require a more expensive light source. SD-OCT systems can utilize simple broadband sources, however they

suffer from severe signal roll-off in depth and require more complicated detection optics, i.e., linescan cameras and spectrometers [Ham11]. Ultrahigh axial resolution of 2.1 μm to 3.5 μm in the retina at 10 kHz to 29 kHz axial scan rates were demonstrated with SD-OCT systems [Cen04, Lei04, Woj04]. Recently, by using high-speed CMOS cameras in retinal imaging an axial scan rate of 312 kHz was obtained with an axial resolution of 8-9 μm in the 850 nm spectral range [Pot10]. Current commercial SD-OCT systems typically achieve ~5 μm axial resolution with ~25-27 kHz axial scan rates over an imaging range of ~2.0-2.6 mm. The fastest speed in retina imaging was demonstrated by Fujimoto et al. at 100,000-400,000 axial scans per second with an axial resolution of 5.3 μm, using a 1050 nm SS-OCT system [Pot10]. Although the current SS-OCT systems seem to perform better than SD-OCT systems due to the improved light sources, SD-OCT systems have been used quite extensively for polarization sensitive OCT, Doppler OCT, ultra-wide-bandwidth OCT, ultra-high-resolution OCT and, moreover, they represent the state of the art in commercial ophthalmologic OCT systems [Ham11].

1.5 Essential OCT parameters

The essential parameters that determine the imaging quality of FD-OCT systems are center wavelength, axial resolution, maximum imaging depth, signal-to-noise ratio (SNR), and sensitivity roll-off in depth.

Firstly, the OCT imaging depth is limited by the amount of scattering (higher at shorter wavelengths) and absorption (higher at longer wavelengths) in biological tissue. Therefore, the OCT imaging depth depends on the choice of center wavelength of the OCT system. Tissue is a non-homogeneous medium which is constituted of cells maintained in a lattice. As a consequence light is incident on tissue is scattered off these structures. Additionally tissue can absorb light by chromophores molecules that it contains [And08]. Therefore, the interaction of light with biological tissue occurs through scattering and absorption. The overall effect of scattering and absorption processes is the attenuation of ballistic light in depth which results in reduction of the imaging depth and contrast, and resolution of the OCT system. Only backscattered photons from a target layer selected by the coherence gate of the light source contribute to the useful depth information, whereas bulk backscattered photons increase the noise in the OCT signal [And08]. In this PhD project, two common OCT wavelengths (λ_c) are used, 800 nm for imaging ophthalmic structures where water absorption is dominant and 1300 nm for dermal imaging where scattering is dominant.

Secondly, the axial resolution of an SD-OCT system is determined by the effective bandwidth of the light that is detected. It depends on both, the bandwidth

of the light source and the bandwidth of the spectrometer. If the spectrum of the light source, as measured with the spectrometer, has a Gaussian envelope with full width at half maximum (FWHM) $\Delta\lambda_{FWHM}$, the axial (depth) resolution Δz is given by [Swa92]

$$\Delta z = \frac{2\ln 2}{\pi n}\left(\frac{\lambda^2}{\Delta\lambda_{FWHM}}\right), \tag{1.13}$$

where n is the (group) refractive index of the imaged tissue and λ is the center wavelength of the source.

Thirdly, the maximum imaging depth z_{max} in SD-OCT is determined by the spectral sampling interval (δk, k is the wavenumber). From Nyquists's sampling theorem, the spectral sampling at δk spacing leads to a maximum path length of $1/(2\delta k)$. However, since every path length corresponds to half the depth (light travels back and forth to the detector), the imaging depth becomes $1/(4\delta k)$. Considering the wavenumber-to-wavelength conversion, it becomes [Häu98]

$$z_{\max} = \frac{\lambda^2}{4n\delta\lambda}, \tag{1.14}$$

where $\delta\lambda$ is the wavelength resolution of the spectrometer.

Fourthly, the roll-off in depth of the SD-OCT signal is determined by the spectral content (i.e. full-width-at-half-maximum (FWHM) of the transmission response of a single channel) of the spectrometer and the camera pixel size. The imaging range of SD-OCT is limited by the signal roll-off, which is the attenuation of the OCT signal due to washout of the interference fringe visibility with increasing depth. The signal amplitude roll-off function is given by [Hu07]

$$A(z) = \frac{\sin(d_x \mathcal{R} z)}{(d_x \mathcal{R} z)} \exp\left[-\frac{a^2 \mathcal{R}^2 z^2}{4\ln 2}\right], \tag{1.15}$$

where d_x is the pixel width, $\mathcal{R} = \delta k/d_x$ is the reciprocal linear dispersion of the spectrometer, and a is the spot size. The sinc and Gaussian functions in Eq. (1.15) correspond to the Fourier transform (FT) of the square-shaped camera pixels and Gaussian beam profile in the spectrometer, respectively. Considering the sinc function, it is beneficial to have a small pixel size and large linear dispersion (small reciprocal dispersion) in order to get a better signal roll-off. In order to reduce the effect of Gaussian function on signal roll-off, the FWHM diameter of the focused spot size as well as the reciprocal linear dispersion should be reduced which necessitates a grating spectrometer with a high groove density (large number of

arrayed waveguides in an arrayed waveguide grating ,AWG, spectrometer). By applying wavenumber-to-wavelength conversion, Eq. (1.15) becomes

$$A(z)=\frac{\sin((2\pi n\delta\lambda/\lambda^2)z)}{(2\pi n\delta\lambda/\lambda^2)z}\exp\left[-\frac{\pi^2}{\ln 2}\left(\frac{an\delta\lambda z}{\lambda^2 d_x}\right)^2\right], \tag{1.16}$$

Rearranging Eq. (1.16) by using Eq. (1.14) yields

$$A(z)=\frac{\sin(\pi z/2z_{\max})}{(\pi z/2z_{\max})}\exp\left[-\frac{\pi^2\omega^2}{16\ln 2}\left(\frac{z}{z_{\max}}\right)^2\right], \tag{1.17}$$

z_{max} is taken from Eq. (1.14) and (a/d_x) is defined as ω in Ref. [Yun03], which is the ratio of the spectrometer FWHM transmission response of a single channel to the wavelength resolution.

Finally, for maximum SNR, the spectrometer loss should be minimized in the design stage which will be discussed in Chapter 2 for an AWG spectrometer. Typical SNR values for high-quality OCT imaging are on the order of 100-110 dB [Ham11, Cen04, Hu07].

1.6 Miniaturization of OCT systems

Commercial OCT systems contain a multitude of fiber and free-space optical components which make these instruments costly and bulky. Considering the size and cost of a commercial OCT system, it is essential to investigate different approaches for realizing a compact and cheap OCT system in order to make it accessible to a wider group of medical doctors and researchers. Integrated optics can provide a dramatic size and cost reduction for OCT systems while maintaining the imaging quality. A suitable material technology and optimum design may allow one to fabricate extremely compact and low-cost OCT systems. In addition to its low cost and small footprint, this approach provides mechanical stability due to its monolithic and alignment-free construction. Moreover integrated optics can enhance the performance of OCT by, for example, parallelization [Bou01, Bou05] of OCT devices on a chip. A generalized schematic of a miniaturized SD-OCT system is depicted in Fig. 1.5.

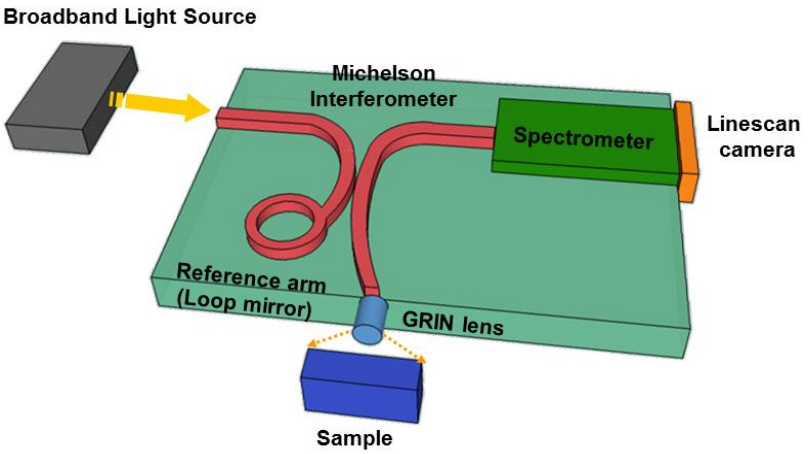

Fig. 1.5 Schematic diagram of the miniaturized spectral domain optical coherence tomography system (SD-OCT) with an external light source and a linescan camera. A loop mirror is used in the reference arm of the Michelson interferometer.

Two different on-chip SD-OCT system configurations will be discussed throughout of this thesis. They differ in the layout of their reference arm, as shown in Fig. 1.6 and Fig. 1.7. In the configuration given in Fig. 1.6, the reference arm is an external mirror which makes it more flexible whereas it is an on-chip delay line in the configuration given in Fig. 1.7 which makes it more compact and stable. Their working principle is the same. A 3-dB coupler is used to split the incoming light equally towards sample and reference arms. In the configuration given in Fig. 1.6 the light reflected off the sample and the reference mirror interfere in the 3-dB coupler where in the configuration given in Fig. 1.7 the light reflected off the sample passes twice the 3-dB coupler and it merges with the light coming from the reference arm in the Y combiner. The recombined light enters the input waveguide of the AWG. The AWG will disperse the light and it will be imaged onto the linescan camera by a lens.

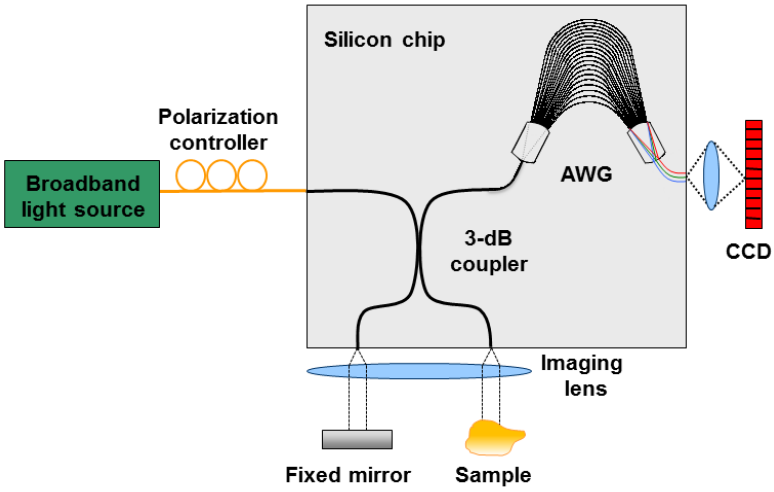

Fig. 1.6 Schematic of the partially-integrated SD-OCT system with an external mirror in the reference arm.

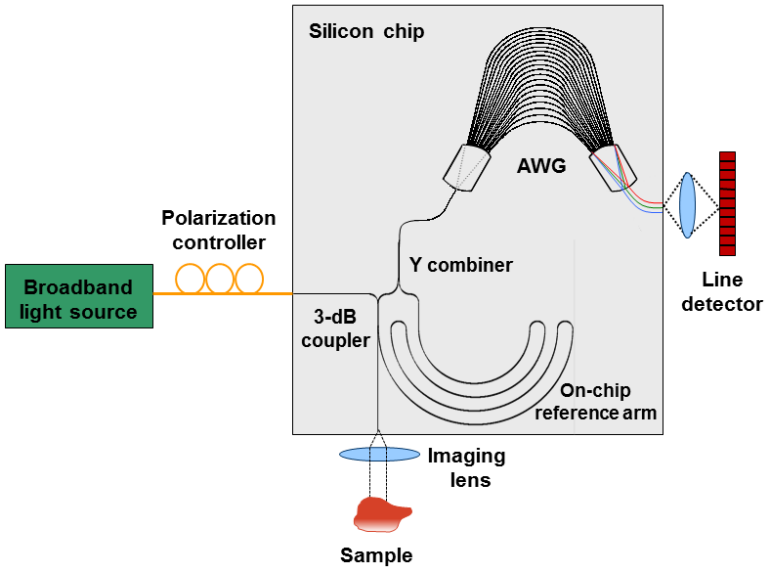

Fig. 1.7 Schematic of the partially-integrated SD-OCT system with an on-chip reference arm. The light reflected off the sample and the light coming from reference arm merge in the Y combiner.

1.6.1 Overview of SD-OCT components

In this project an SD-OCT system will be miniaturized on a silicon chip. Here we will discuss the different components of an SD-OCT system, their integrated optics counterparts, and the possibilities of integrating these components on a chip.

1.6.1.1 Beam splitter

This is the key component of any OCT system, which can be integrated on a chip. There are several types of integrated optical couplers, given in Fig. 1.8 that can be used as a beam splitter in an on-chip MI. Among all these couplers, directional couplers (DCs) are the preferable kind of couplers, for low to medium contrast waveguide technology, especially if optical efficiency is important. It is difficult to make mutli-mode interference (MMI) couplers lossless in low-contrast waveguide systems due to imperfect self-imaging properties. Two-mode interference (TMI) couplers are lossy due to the required sharp features that cannot be faithfully reproduced by current lithographic techniques. Single-mode interference (SMI) couplers are essentially lossy as two modes are inevitably excited at the junction, with equal intensities, of which one cannot be guided and is thus lost as radiation. DC's are essentially lossless. However, the splitting ratio of DCs is not constant (differs from 3-dB) over a broad spectral range. Wavelength-insensitive couplers such as Mach-Zehnder based or non-uniform adiabatic couplers could solve this problem by providing an almost constant splitting ratio over broad spectral ranges (>100 nm) without introducing any excess loss, as will be discussed in Chapter 3 in detail.

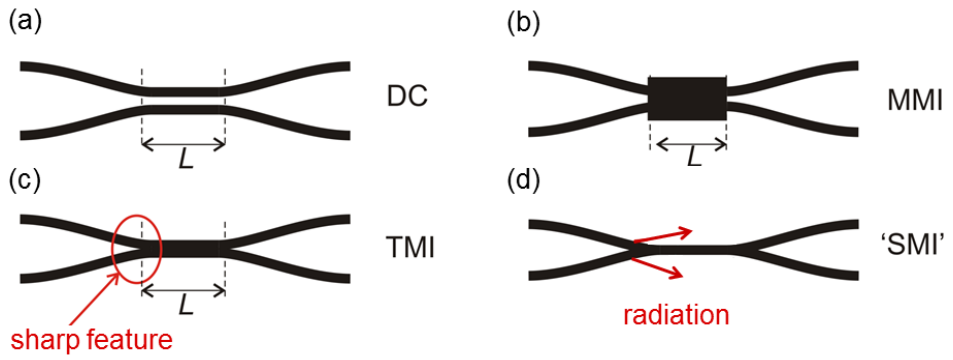

Fig. 1.8 Different types of integrated optical couplers: **(a)** Directional coupler (DC), **(b)** Multi-mode interferometer (MMI), **(c)** Two-mode interferometer (TMI), **(d)** 'Single-mode' interferometer (SMI). *L* is the coupling length.

1.6.1.2 Optical waveguides

Optical waveguides are the key components of integrated optical circuits. The spectrometer and MI of an on-chip SD-OCT system consist of multitudes of optical waveguides which should have good transmission characteristics for the wavelength range associated with the broadband source. They have to be single mode and the overall propagation losses and birefringence have to be low. The index contrast and the waveguide geometry determine the divergence of the free-space beam emerging from sample and reference arms. For the OCT application, the waveguides should be designed to produce a low-divergence output beam while maintaining a small device size.

Optical waveguides can be classified according to their geometry (planar, channel, rib/ridge waveguides), mode structure (single-mode, multi-mode), refractive index distribution (step or gradient index) and material (glass, polymer, semiconductor). Figure 1.9 depicts the commonly used optical waveguide geometries in integrated optics.

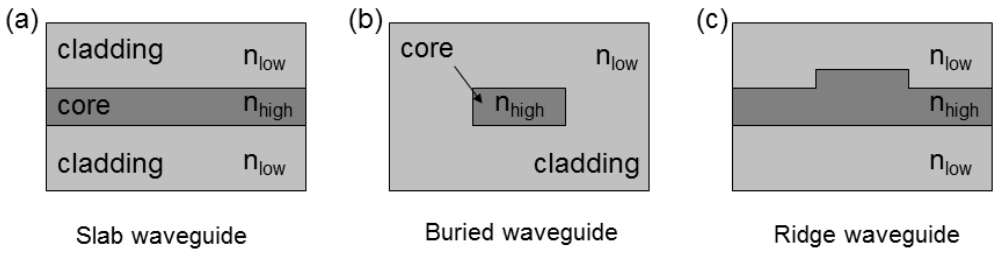

Fig. 1.9 Optical waveguides classified according to their geometry **(a)** slab, **(b)** buried, **(c)** ridge waveguide.

1.6.1.3 Light source

OCT imaging requires a source with a broad bandwidth and a short low-coherence length, which is needed to construct images with micrometer resolution. Several types of optical sources have been considered for OCT systems. Due to their relatively low cost, robustness and ease of use, superluminescent diodes (SLDs) have been most frequently used as a source for OCT systems. In integrated optics SLDs are commonly made in waveguide structures. As the light source requires the use of active materials which in most cases are not optimum for producing low-loss waveguides, it is generally manufactured on a different chip. However, with the use of hybrid integration (chip to chip connection), the light source chip can be integrated with the waveguide chip. The fabrication of an integrated broad bandwidth source is beyond the scope of this PhD project.

1.6.1.4 Spectrometer

The spectrometer is the principal component of SD-OCT systems. Each of its parameters can have a dramatic effect on overall system performance. The axial resolution, maximum imaging range, and signal roll-off of an SD-OCT system are all dependent on the spectrometer's design. It is an expensive component which usually consumes a lot of space. Additionally it is fragile and susceptible to miscalibration. Therefore this part has to be integrated on a chip. The complexity of the spectrometer and its desired resolution and efficiency make this component the most challenging one to fabricate on a chip. Monolithic spectrometers have been made, although not at the required spectral resolution [Gol90, Avr06, San96, San01]. Echelle grating spectrometers can provide high resolution, however there are several issues which limit the common use of echelle gratings such as facet-roughness related losses, polarization dependence of the grating efficiency, and birefringence [Che07b].

Although integration of a spectrometer on a chip is challenging, arrayed waveguide gratings (AWGs) present a well-established way towards miniaturization. Besides their extensive usage in telecommunication for (de)multiplexing [Smi88], AWGs are also ideally suited for applications such as OCT and spectroscopy [Ism11], with their high spectral resolution, small form factor, large bandwidth, and low insertion loss. In addition to their advantages listed above, AWGs are cost-effective, which makes them favorable for integration with SD-OCT systems. However, there are design limitations on resolution and free spectral range (FSR), which restrict the axial resolution and maximum imaging range of SD-OCT systems. By applying different approaches (e.g. cascading several AWGs), these limitations can be overcome.

1.6.1.5 Detector

The detector in an OCT system must have a high responsivity in the same spectral region as the light source. The fabrication of a light detector requires a different fabrication method and material platform than the waveguides. In this project we will use a commercially available linescan camera. To minimize the overall SD-OCT system size, the detector can be butt-coupled to the imaging plane of the spectrometer. However this necessitates a special spectrometer design with a flat-focal-field, since CCD pixels usually are manufactured on a planar surface, which is difficult to align with the curved focal surface of a conventionally designed spectrometer. Such an AWG design will be discussed in Chapter 5.

1.6.1.6 Sample station

The sample arm contains the transverse scanning mechanism and focusing optics. It is responsible for transmitting and receiving light between the sample and the system. Therefore it is important to choose components that will provide the necessary scanning range, transverse resolution, and scan speed. In this project a commercial optical scanner is used which can be custom made for the particular application, e.g. for the eye or for the skin. The laser beam is scanned across the surface of the sample by means of two galvanometer-based rotating mirrors (x and y directions). Integrated optics opens the possibility of considerably reducing the scanning requirements in one direction by using multiple output waveguides located close to each, thus providing parallel signal acquisition. This, however, is beyond the scope of this project.

1.6.2 Literature survey

Only limited data on the implementation of OCT components on a chip exist. Culemann et al. [Cul00] fabricated an integrated optical sensor chip in ion-exchanged low-index-contrast glass for time-domain OCT, with all other components external to the optical chip. Margallo-Balbas et al. realized a rapidly scanning delay line in silicon – based on the thermo-optic effect of silicon – for application in time-domain OCT. An operating line rate of 10 kHz and a scan range of nearly 1 mm have been reported [Bal10]. Yurtsever et al. [Yur10] demonstrated a silicon-based Michelson interferometer for a swept-source OCT system with 40 μm of axial resolution and a sensitivity of 25 dB, both insufficient for imaging. Nguyen et al. [Ngu10] demonstrated integrated elliptic couplers and applied them to Fizeau-based spectral-domain low-coherence depth ranging. Choi et al. were the first to demonstrate the performance of an AWG spectrometer in an SD-OCT system with a depth range of 3 mm and an axial resolution of 23 μm. However, they needed semiconductor optical amplifiers in order to obtain sufficient sensitivity for imaging [Cho08]. Recently InAs/InP quantum dot based waveguide photodetectors [Jia12] and a tunable laser source[Til12] for SS-OCT systems operating around 1.7 μm were presented, however OCT imaging has not been demonstrated yet.

2 Integrated spectrometers: Arrayed waveguide grating (AWG)

2.1 Working principle

There are several different ways for dispersing light into its different wavelength components. The arrayed waveguide grating (AWG), which was first proposed by Smit in 1988 [Smi88], is a powerful light dispersion technique with high accuracy and stability. The AWG is attractive not only for use in optical wavelength-division-multiplexed (WDM) networks but also for potential applications to various spectroscopic measurements. It was further developed in the following years by Takahashi [Tka90] and Dragone [Dra91], who extended the concept from $1 \times N$ demultiplexers to $N \times N$ wavelength routers. Since then, many AWGs have been designed in order to improve the crosstalk level, insertion loss, channel spacing, polarization independence, and total device size in different material systems [Hib02, Tak02[a], Tak02[b], Tri97, Fuk04, Che07a, , Sch00, Shi02, Gon05, Lee04].

An AWG consists of input/output waveguides, two focusing slab waveguides and a phased array of multiple waveguides with a constant path length difference ΔL between neighboring waveguides as shown in Fig. 2.1a. The operation of an AWG [Smi96] is briefly explained, referring to Fig. 2.1a. Light from an input waveguide becomes laterally divergent in a first free propagation region (FPR) and illuminates the input facets of an array of waveguides with a linearly increasing length that leads to their typical curved shape. For a central design wavelength λ_c the phase difference at the output facets of adjacent array waveguides is an integer multiple of 2π. Since these facets are arranged on a circle, a cylindrical wavefront is formed at the beginning of a second FPR, which generates a focal spot at the central output waveguide. The phase shift caused by the length differences between arrayed waveguides is linearly dependent on wavelength, the resulting wavelength-dependent phase gradient implies a tilt of the cylindrical wavefront at the beginning of the second FPR, which causes the focal spot to shift to a different output waveguide with wavelength.

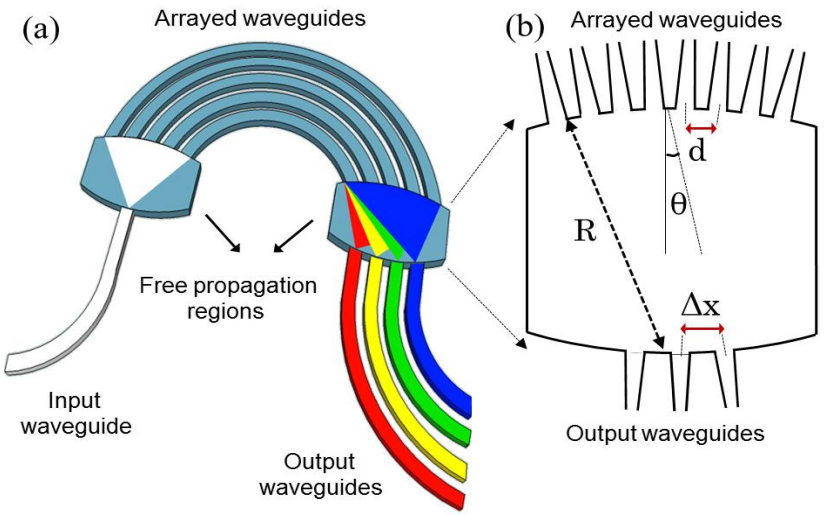

Fig. 2.1 (a) Schematic layout of an arrayed waveguide grating (AWG). **(b)** Geometry of the receiver side of the AWG (2nd FPR) and definition of parameters *Δx, d, R, θ*: see Table 2.1.

The fundamental optical parameters of an AWG, such as center wavelength (λ_c), wavelength channel spacing (δλ), and free spectral range (FSR), i.e. frequency difference between two adjacent spatial diffraction orders, can be derived by applying the grating equation to the AWG geometry which is given as [Pal05]

$$n_s d \sin(\theta_i) + n_c \Delta L + n_s d \sin(\theta_o) = m\lambda, \tag{2.1}$$

$$\theta_i = i\frac{\Delta x}{R}\ ,\ \theta_o = j\frac{\Delta x}{R},$$

where n_s is the effective refractive index of the slab region, n_c is the effective refractive index of the array waveguides, ΔL is the length difference between two adjacent waveguides in the grating, d is the separation between the array waveguides, Δx is the focal point deviation in the imaging plane from its central position (also known as the separation between output waveguides), R is the slab radius, m is the grating order, i and j are the number of the input and output waveguides, respectively, θ_i is the angle of the far-field diffracted light cone of the input waveguide, and is θ_o the acceptance angle of one of the output waveguides, and λ is the wavelength. The definitions of each AWG design parameter is given in Table 2.1.The fundamental design parameters of an AWG spectrometer can be extracted from Eq. 2.1 as given below. The derivations of these formulas are given in Appendix A1.

Center wavelength: $$\lambda_c = \frac{n_c \Delta L}{m}, \quad (2.2)$$

Wavelength resolution: $$\delta\lambda = \frac{n_s d^2}{mR}, \quad (2.3)$$

Free spectral range (FSR):[1] $$FSR = \frac{\lambda_c}{m}, \quad (2.4)$$

Table 2.1: *AWG design parameters*

Symbols	Description
λ_c	Center wavelength
m	Diffraction order
ΔL	Optical path length difference between adjacent arrayed waveguides
R	Focal length of slab waveguide (Radius of grating circle)
d	Separation between arrayed waveguides (center to center)
Δx	Focal point deviation in the imaging plane from its central position (Separation between output waveguides (center to center))
$\delta\lambda$	Wavelength spacing between adjacent output waveguides
FSR	Free spectral range
θ_i	Angle of the far-field diffracted light cone of the input waveguide
θ_o	Acceptance angle of one of the output waveguides
N	Number of output waveguides
M	Number of arrayed waveguides
i	Number of ith input waveguide away from center
j	Number of jth output waveguide away from center
n_s	Effective refractive index of slab waveguide
n_c	Effective refractive index of arrayed waveguides

[1] In given formulas the wavelength dependence of the refractive index is assumed to be zero, i.e. group refractive index is equal to effective refractive index of the waveguide ($n_g \sim n_c$).

2.2 Technology choice

2.2.1 Literature review

Silica waveguide technology is one of the important technologies used for the realization of AWGs due to its good stability, low fiber coupling loss, good channel uniformity, and high wavelength accuracy. To date, the smallest channel spacing of 1 GHz has been reported on a 16-channel silica AWG at a central wavelength of 1547 nm [Tak02[a]]. The non-adjacent crosstalk and loss values of that device ranged between -14 and -16 dB and between 8 and 11 dB, respectively. The largest free spectral range (FSR) of 215 nm has been achieved in a 25-GHz-spaced 1080-channel AWG using a tandem configuration [Tak02[b]]. The non-adjacent crosstalk and loss values of that device ranged from -45 to -28 dB and 4.5 to 10 dB, respectively. However, these good crosstalk values were obtained after phase compensation with ultraviolet irradiation through a metal mask which complicates the fabrication process. In addition, due to the low refractive index contrast ($\Delta n \approx$ 0.005-0.007), which is defined as $\Delta n = (n_{core}-n_{cladding})/n_{core}$, provided by silica, and consequently large required bending radius, these devices occupy a comparatively large area on a 100-mm wafer. However, by using higher-index-contrast waveguides, smaller silica-based AWGs have been realized [Hib02]. By employing waveguides with Δn = 0.0015, a 25-GHz-spacing 256-channel silica-based AWG was fabricated on a 100-mm silicon wafer, which would be more than 100 cm^2 when using conventional waveguides with Δn = 0.0075, [Hib00]. Silica-based AWG multi/demultiplexers have become commercially available from a number of different suppliers. Although the typical wavelength resolution is 50 or 100 GHz, NTT Electronics can provide AWGs with 25 GHz wavelength resolution. Non-adjacent crosstalk of -30 dB and 3 dB insertion loss are typical values for commercially available silica AWGs.

The silicon-on-insulator (SOI) technology provides a high refractive index contrast ($\Delta n \approx$ 0.6), resulting in a markedly reduced device size. The typical bending radius is on the order of several micrometers and is not the limiting factor for minimizing the device size. The first SOI AWG was reported by Trinh but the device size was still quite large [Tri97]. Fukazawa et al. reported a 6-nm-spaced 17-channel AWG at 1550 nm, using silicon photonic wires, with an overall device size of 110 μm × 93 μm [Fuk04]. They achieved a FSR of 90 nm, so far the largest value reported for SOI AWGs. Cheben et al. reported the highest resolution using silicon photonic wires [Che07]. The device had 50 channels with 0.2 nm of channel spacing at 1550 nm. The non-adjacent crosstalk level was -10 dB or better. Although SOI technology provides the opportunity of a very small footprint, the

crosstalk and fiber coupling loss suffer significantly from the high refractive index contrast. In addition, silicon-based integrated optical devices only can operate at wavelengths larger than 1000 nm.

Indium phosphite (InP) is a commonly used high-index-contrast material technology for operation in the telecom window. The most important advantage of InP-based AWGs is their monolithical integration with devices like lasers and semiconductor optical amplifiers. The biggest drawback of InP-based AWGs is their coupling losses to single-mode fibers which are in the order of 10 dB. InP layers are deposited by epitaxial growth which gives a precise control over the growth parameters, e.g. thickness, however it is a costly growth technique. The first InP-based AWG was reported by Zirngibl et al. with an insertion loss of 2-4 dB and a non-adjacent crosstalk <-18 dB [Zir92]. The InP-based AWG with the largest number of output channels was demonstrated by NTT with 64 channels [Koh97]. The device exhibited a non-adjacent crosstalk value better than -20 dB and an insertion loss value of 7 dB. Barbarin et al. was reported the smallest InP AWG with a footprint of 230×330 μm^2, an insertion loss of < 5dB, a high non-adjacent crosstalk value of <-12 dB [Bar04].

Silicon-oxynitride (SiON) is a promising material, considering the problems of insertion loss, crosstalk, and device size in the previously mentioned material technologies [Wör07]. Besides possessing excellent optical properties (e.g., optical loss below 0.2 dB/cm) it can be deposited with refractive indices varying over a wide range (1.45-2.0) by tuning the material composition. In the literature, there is only limited data on SiON-based AWG spectrometers [Sch00, Shi02, Gon05, Lee04]. Schauwecker et al. reported the smallest AWG on the SiON platform, with 5 nm channel spacing at 725 nm [Sch00]. With an overall chip size of 5 mm × 2 mm, a non-adjacent crosstalk value of -30 dB, and an insertion loss of 4.5 to 7 dB were obtained. The fiber-to-chip coupling loss of a 32 channel, 100 GHz spacing AWG has been reduced significantly with integrated spot-size converters [Lei04*]. The best performance in terms of resolution and FSR was reported by Shimoda et al. [Shi02]. Their AWG showed 100 GHz channel spacing, 32 nm FSR, -30 dB non-adjacent crosstalk, and 2.5 dB insertion loss at the central wavelength of 1550 nm. The state of the art of different AWG technologies is summarized in Table 2.2.

Table 2.2: *State of the art of different AWG technologies.*

δλ [GHz]	FSR [nm]	λ_c [nm]	*N*	Non-adjacent crosstalk [dB]	Loss[2] [dB]	Material	Device size (mm^2)	References
1	0.128	1547	16	-16	8***	SiO_2	100×100	[Tak02[a]]
25	215	1550	1080	-45	4.5***	SiO_2	100×100	[Tak02[b]]
237	7.6	1550	4	<-22	<6**	SOI	27×27	[Tri97]
750	90	1550	17	-10	<10***	SOI	0.11×0.093	[Fuk04]
25	10	1550	50	<-10	17**	SOI	8×8	[Che07[a]]
2845	25	725	5	<-30	5**	SiON	5×2	[Sch00]
100	32	1550	40	-30	2.5**	SiON	20×22	[Shi02]
100	25.6	1550	32	<-30	2**	SiON	Not specified	[Lei04*]
25 to200	1.6 to128	L-C bands	8 to 80	<-30	<3**	SiO_2	-	NTT
50	25.6	1550	64	-20	14.4**	InP	3.6×7	[Koh97]
400	12.8	1550	4	<-12	<5**	InP	0.23×0.33	[Bar04]
87	10.5	1560	15	<-18	2*	InP	10×10	[Zir92]

2.2.2 Silicon oxynitride

General requirements which have to be fulfilled for the realization of integrated optical devices are low propagation and insertion loss, efficient fiber-to-chip coupling, small bend radius, and low fabrication cost that should be met for successful realization of the technology. Most of the materials used in integrated optics are classified as either low contrast (e.g. silica, polymers) or high contrast (e.g. InP, SOI). The satisfaction of all of the above mentioned requirements simultaneously for both of these systems is rather difficult. In the low contrast

[2] * excess loss only, ** including fiber-to-chip coupling loss, *** not specified in the reference

systems the fiber-to-chip coupling efficiency is excellent (i.e. 0.1 dB [Ger00]) due to the large size of the single mode waveguides, but they have low integration density due to large bend radius (~15-20 mm [Bon99]) required for low loss operation whereas high contrast systems allow for very small bending radius (~1-100 μm [Lim99]) with low losses, but efficient fiber-to-chip coupling is difficult (3-10 dB [Che07[a]]) to obtain due to small mode field dimensions.

SiON is a very attractive material for integrated optics which is a combination of silicon dioxide (SiO_2) and silicon nitride (Si_3N_4). The refractive index of SiON can be tuned between the values of SiO_2 (1.45) and Si_3N_4 (2.0) by changing the ratio between oxygen and nitrogen in the film, thus allowing for a flexible and customized waveguide design [Wör07]. The bending radius can be reduced to several hundreds of micrometers by using the highest refractive index contrast with a proper waveguide geometry. Furthermore, since SiON is transparent in a broad wavelength range from 210 nm to beyond 2000 nm [Wör07], AWGs can be fabricated for both the visible and infrared wavelength ranges by use of the same material system. In addition, SiON is intrinsically compatible with the silicon processing technology which enables low cost mass production. Due to its excellent properties (e.g., optical loss below 0.2 dB/cm), SiON was chosen as the material platform for the realization of all integrated optical devices that will be discussed throughout this thesis.

The intrinsic compatibility of SiON thin film fabrication with silicon processing technology largely adds to the attractiveness of this waveguide material. Various, mature and low-cost mass-production enabling techniques are available such as plasma enhanced chemical vapor deposition (PECVD), low pressure chemical vapor deposition (LPCVD), and sputtering. Since PECVD is the fastest and most economical method of SiON processing, it was chosen as the deposition technique of this research. The maximum thickness and the corresponding refractive index for a crack-free PECVD grown SiON film is <1μm and 1.6, respectively. The limitation in the refractive index is due to the high-temperature annealing of the layers for propagation loss minimization. There are essentially three SiON layer parameters of interest that have to be well controlled for obtaining a high device performance. These are layer thickness, uniformity, and refractive index. Throughout this thesis two alternative measurement set-ups, namely Metricon 4-wavelength prism-coupling set-up and Woollam M44 spectroscopic ellipsometer, were used for the characterization of the thickness and the refractive index of the deposited SiON layers. The non-uniformity of the layer thickness and refractive index over the wafer were measured by Plasmos SD 2000 ellipsometer. The prism-coupling set-up provided measurements at wavelengths at 633, 830, 1300, and 1550 nm.

2.2.3 Waveguide design for OCT applications

A buried-channel waveguide geometry is chosen as the basic building block of all integrated optical devices in this thesis due to its smaller bending radius and high fabrication tolerance compare to a ridge/slab waveguide counterpart. There are three design parameters for a channel waveguide; waveguide width, height, and index contrast (index difference between core and cladding layers) as depicted in Fig. 2.2.

Depending upon the operation wavelength range of the OCT applications (around 800 nm for dermal and around 1300 nm for retinal imaging), different waveguide geometries were designed for these ranges. Besides single-mode, low-loss (0.1 dB/cm), and low-channel birefringence ($<10^{-4}$), which is defined as the difference between the effective index for the transverse-magnetic (TM) and transverse-electric (TE) polarizations, operation of these waveguides, their lateral and vertical beam divergence should be low (and preferably close to each other) in order to reduce chip-to-sample coupling losses.

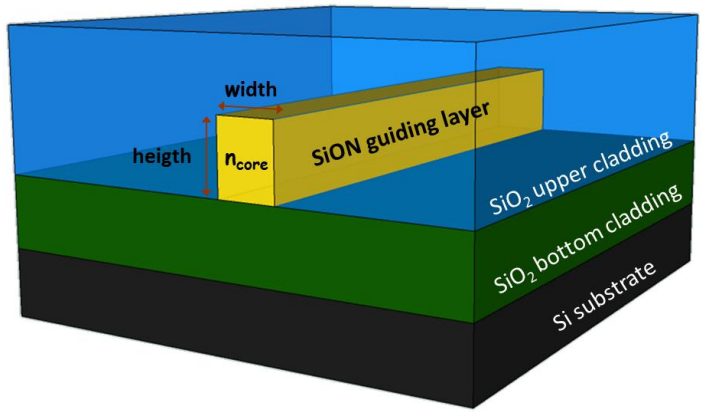

Fig. 2.2 Schematic diagram of a SiON channel waveguide with flexible design parameters of height, width, and core refractive index (n_{core}).

The simulations were performed using the Phoenix Field Designer [http://www.phoenixbv.com] and RSoft BeamProp [http://www.rsoftdesign.com] softwares. The effective refractive index, minimum bending radius, coupling and bending losses, and the minimum acceptable gap between waveguides were extracted from simulation results. Direct simulation of curved waveguides with large angles is difficult due to paraxial limitation of BPM. Therefore the simulated-bend method is applied which makes use of a coordinate transformation to map a curved waveguide onto a straight waveguide. This method gives reliable results for the waveguide widths << radius of curvature.

2.2.3.1 Waveguide design for dermal imaging (λ = 1300 nm)

A common OCT wavelength for imaging human skin is 1300 nm. Although water absorption is higher in this wavelength range compared to 800 nm, the penetration depth is much deeper due to reduced scattering which overcomes the effect of absorption.

Three different single-mode channel waveguide designs were implemented for skin imaging. The waveguide parameters as well as the performance of each waveguide design are summarized in Table 2.3. The first channel waveguide design was realized with the aim of preliminary AWG spectrometer testing to gain feed-back on potential fabrication issues and performance control rather than using it in OCT imaging. This also explains why it is not superior to other two designs in terms of OCT performance The single mode channel waveguide design with a width of 2 µm, a height of 0.8 µm , and a core refractive index of 1.535 (Design #1 in Table 2.3) built mainly on previous waveguide fabrication experience at IOMS [Wör99]. The minimum bending radius was obtained as 800 µm from beam propagation method (BPM) simulations as shown in Fig. 2.4a.

The second waveguide design (Design #2 in Table 2.3) was optimized towards minimized channel birefringence. The low channel birefringence was achieved by balancing the material and waveguide birefringence [Wör07]. Low-channel birefringent waveguides are necessary for eliminating the signal beating in on-chip OCT systems which will be discussed in detail in Section 2.5.3. The width and height of the channel waveguide were optimized by taking into account the fabrication tolerances, i.e. waveguide side wall angle (86^{o}), change in width due to optical lithography (±0.05µm), inaccuracy in waveguide height (±0.05µm), etc. BPM was used to simulate polarization dependency of the channel waveguides. The value of the core refractive index was a compromise between device size and low birefringence operation over a wide wavelength range. For the chosen core refractive index of 1.52, the waveguide height of 1 µm and the waveguide width of 2.2 µm resulted in an effective refractive index difference between TE and TM modes of 6×10^{-6} as given in Fig. 2.3. The waveguide heights of 0.8 µm and 1.2 µm have also low-residual birefringence values at specific waveguide widths, however for 0.8 µm the beam divergence is high whereas for 1.2 µm waveguide becomes multimode at the corresponding waveguide width. The minimum bending radius was simulated as 1200 as depicted in Fig. 2.4b. Although this approach requires a very high fabrication accuracy, it makes AWGs advantageous over conventional spectrometers, constructed with discrete optical components. Using polarization-independent AWG-spectrometers in OCT systems can reduce their size and cost further by eliminating the components for polarization control, as will be

discussed in detail in Chapter 5. However, the design of waveguides with low birefringence requires the choice of a relatively low refractive index contrast, leading to large bending radii and thus limiting the attainable integration density. AWGs are built from many curved waveguides, so their footprint depends strongly on index contrast. The combination of resolution and FSR, required for state-of-the-art OCT cannot be realized with a single AWG. This can be resolved by cascading several AWGs; however with low-contrast polarization-independent waveguides, the footprint of a cascaded-AWG system would exceed the available chip area. Therefore, for on-chip OCT systems priority is given to the high core refractive index rather than polarization-independent operation.

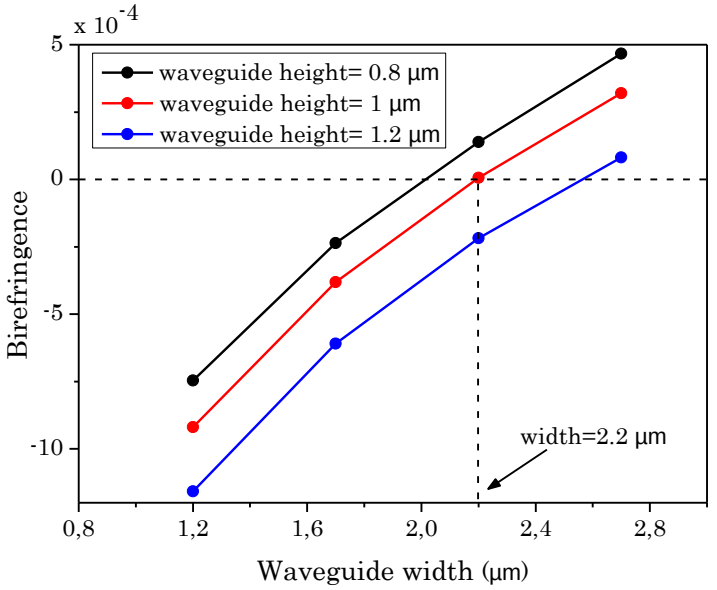

Fig. 2.3 Calculated channel birefringence as a function of waveguide width for different waveguide thicknesses for Design #2 given in Table 2.3. The low-residual birefringence (6×10^{-6}) is obtained for a waveguide width of 2.2 µm and a waveguide height of 1 µm.

The third waveguide geometry focusses on footprint reduction, i.e. minimization of bending radius, to facilitate the full integration of all components such as several cascaded AWGs as well as beam splitters on a single chip. The highly compact design is realized with 1.8 µm of channel width, 1 µm of height and 1.54 of core refractive index (Design #3 in Table 2.3). The minimum bending radius was simulated as 500 µm as shown in Fig. 2.4c. The main advantage of this waveguide design is its high potential integration density and the low divergence of the beam that is radiated from its end facet into free space. The design wavelength

was slightly changed from 1300 nm to 1250 nm due to availability of the light source in the collaborative research group at the Medical University of Vienna.

Table 2.3: *Design parameters of SiON channel waveguides for skin imaging.*

Parameters	Design #1	Design #2	Design #3
Wavelength (nm)	1300	1300	1250
Waveguide width (μm)	2	2.2	1.8
Waveguide height(μm)	0.8	1	1
Core refractive index (TE)	1.535	1.52	1.54
Cladding refractive index (TE)	1.4485	1.4485	1.4485
Channel birefringence ($\times 10^{-4}$)	7.1	0.06	3.1
Integration density	moderate	low	high
Minimum bending radius (μm)	800	1200	500
Remarks	High birefringence	Non-birefringent, low integration density	High integration density

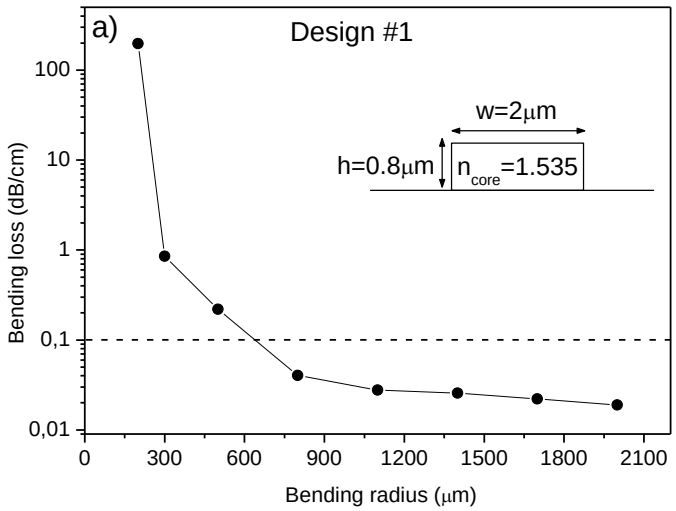

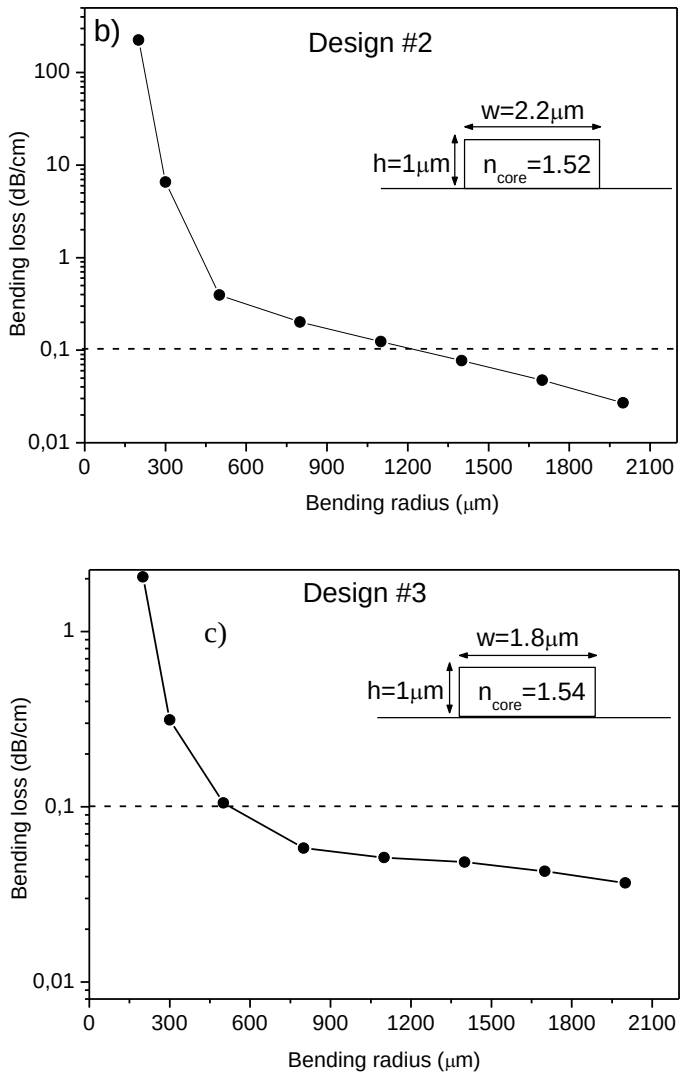

Fig. 2.4 Calculated bending losses as a function of bending radius for **(a)** the first **(b)** the second, and **(c)** third designs given in Table 2.3.

2.2.3.2 Waveguide design for retinal imaging (λ = 800 nm)

A typical center wavelength for the OCT systems used in ophthalmology is 800 nm, due to low absorption in the eye in this wavelength range. The aforementioned waveguide performance for skin imaging (i.e. low loss, high integration capacity, single mode, and low beam divergence etc.) are also valid for the waveguides to be

applied in retinal imaging. The optimized design parameters of the SiON channel waveguides for retinal imaging are listed in Table 2.4. BPM simulations were carried out to calculate the bending losses, as shown in Fig. 2.5.

The ultimate aim of this project is integrating the reference arm on the same chip with the other components, which will eliminate the need for an external mirror. Due to the limited space on the wafer, an on-chip reference arm can only be implemented for the retinal imaging system, which adds an extra waveguide design requirement for this application. The group velocity dispersion (GVD) mismatch between sample arm and reference arm should be low in order to have a good fringe visibility and high axial resolution as well. GVD is defined as the a frequency dependent delay of the different spectral components of the pulse which is given as [www.wikipedia.org]

$$D = \frac{\lambda}{c}\frac{\partial^2 n}{\partial \lambda^2}, \tag{2.5}$$

where c is the speed of light, n is the refractive index of the medium and λ is the wavelength.

According to BPM simulations the current waveguide design exhibits a GVD of -140 ps/km/nm around 800 nm as shown in Fig. 2.6. We do not expect any fringe loss or broadening in the axial resolution for this waveguide design. The detailed analysis and verification will be discussed in Chapter 3.

Table 2.4: *Design parameters of SiON channel waveguides for retinal imaging.*

Parameters	Values
Wavelength (nm)	800
Waveguide width (μm)	1.5
Waveguide height(μm)	0.8
Core refractive index (TE)	1.5
Cladding refractive index (TE)	1.456
Channel birefringence ($\times 10^{-4}$)	6.6
Minimum bending radius (μm)	800
Group velocity dispersion (ps/km/nm)	140

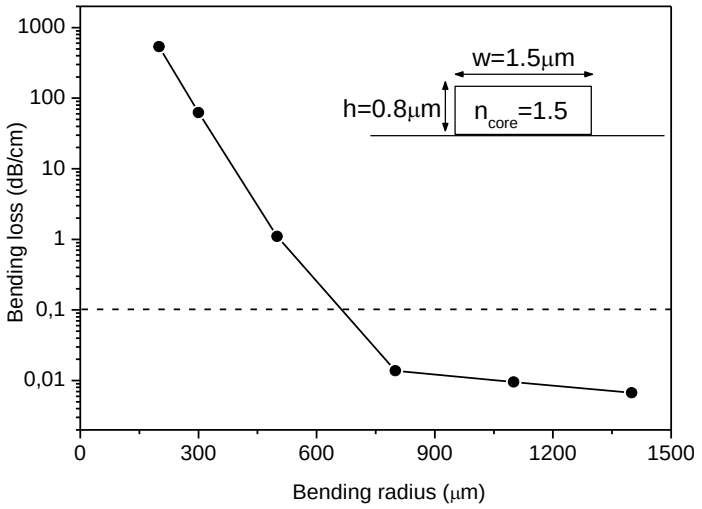

Fig. 2.5 Calculated bending losses as a function of bending radius at 800 nm.

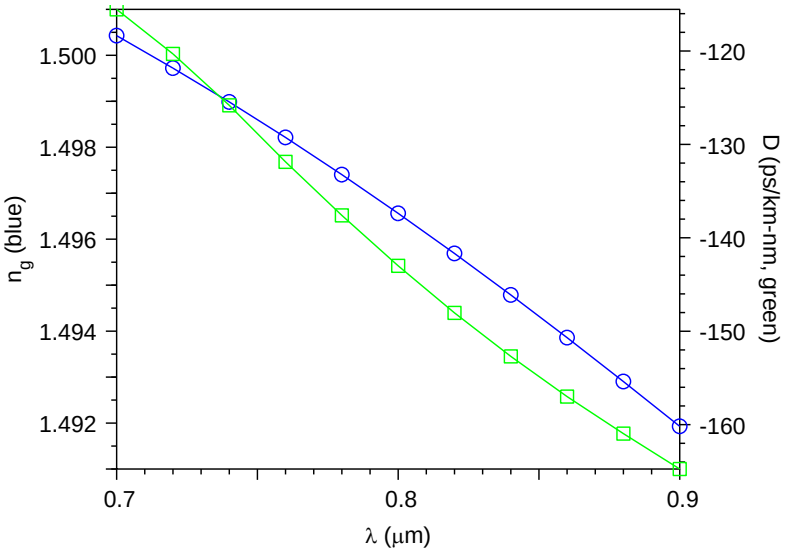

Fig. 2.6 Calculated group velocity dispersion (GVD) of the 800-nm waveguide geometry.

2.2.4 Fabrication

The fabrication process flow of the waveguides is displayed in Fig. 2.7.

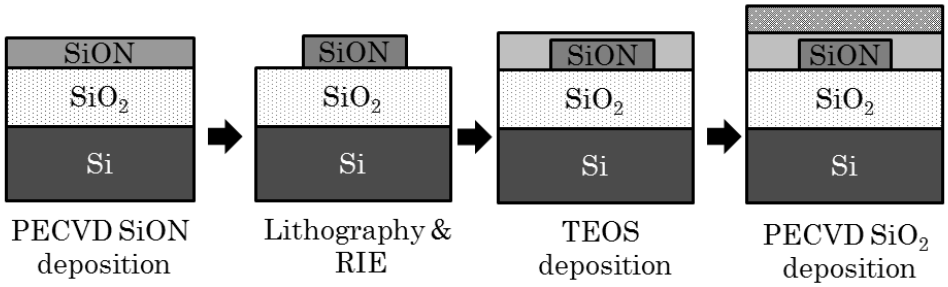

Fig. 2.7 Fabrication process flow of the waveguides.

An 8-μm-thick oxide layer, serving as bottom cladding of the waveguides, was thermally grown on 100-mm <100> oriented silicon substrates. A SiON core layer was deposited in either Oxford Plasmalab System 80 PECVD reactor or Oxford Plasmalab System 133 PECVD reactor at a substrate temperature of 300°C, and a power of 60 W (187.5 KHz). A chamber pressure of 650 mTorr and 500 mTorr was used in Oxford Plasmalab System 80 PECVD and Oxford Plasmalab System 133 PECVD, respectively. Silane (2% SiH_4 diluted in N_2) and nitrous oxide (N_2O) served as precursors in the deposition process. The relative gas-flow ratio N_2O/SiH_4 of each waveguide design as well as the parameters for the SiON layer deposition are summarized in Table 2.5. The wavelength dispersion of the SiON refractive index was measured at three discrete wavelengths (i.e. 633 nm, 830 nm, 1300 nm) by prism coupling method. Deposition processes were followed by thermal annealing at 1150^{o}C for 3 hours, for layer densification, stabilization of thickness and refractive index, and propagation loss minimization.

The waveguiding channels were defined photolithographically. For this, a 500-nm-thick photoresist masking layer was spin-coated on top of the core layer. The waveguide pattern was defined in the photoresist layer with standard lithography and a development step. Then the waveguide channels were etched in a Plasma Therm 790 RIE reactor applying a gas mixture of CHF_3 and O_2 (100 sccm / 2 sccm) at 28 mTorr pressure, 350 W plasma power, and 20^{o}C substrate temperature. Scanning electron microcopy (SEM) images of the test structures (w = 2 μm and h = 0.8 μm) before top oxide layer deposition are presented in Fig. 2.8.

Table 2.5: *Parameters for core and top cladding material deposition.*

		PECVD SiON	PECVD SiO_2	TEOS (LPCVD SiO_2)
Plasma power (W)		60	60	-
Plasma frequency (kHz)		187.5	187.5	-
Chamber pressure (mTorr)		650/500[3]	650	400
Substrate temperature (^oC)		300	300	710-740
2%SiH_4/N_2 flow (sccm)		1000	200	-
N_2O flow (sccm)	Design #1	300	710	-
	Design #2	250	710	
	Design #3	584	710	
	800 nm design	1406	710	
N_2 flow (sccm)		-	-	30
TEOS flow		-	-	40

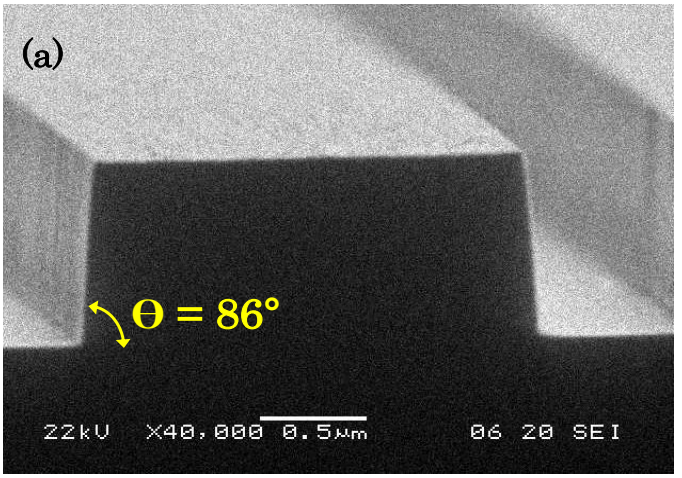

[3] The chamber pressure of 650 mTorr was used in Oxford Plasmalab System 80 PECVD whereas 500 mTorr was used in Oxford Plasmalab System 133 PECVD.

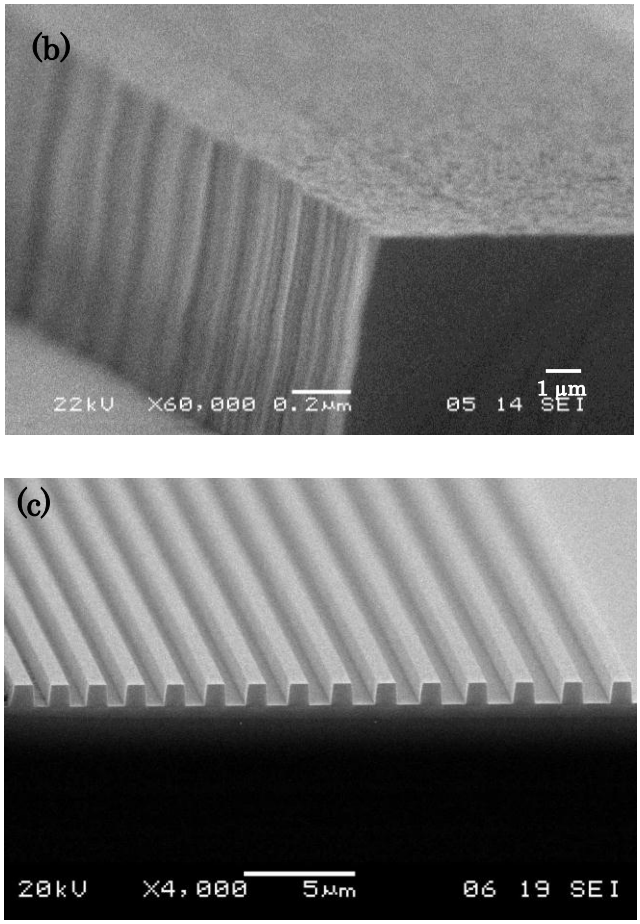

Fig. 2.8 SEM images of the test structures before top SiO_2 cladding deposition; **(a)** side wall angle (86°), **(b)** side wall roughness (≤40 nm), **(c)** arrayed waveguides.

According to the SEM images, a sidewall roughness of ≤ 40 nm and a sidewall angle of 86° were obtained for both spectral ranges. The sidewall angle of 86° results in an effective refractive index difference which causes a center wavelength shift between designed and fabricated devices which was taken into account in the device design.

After removal of the photoresist layer, the upper cladding oxide layers were deposited in two steps. In order to obtain a conformal coverage (i.e. eliminating

voids at the corners) of the channel waveguides, a 1-µm-thick oxide layer was first grown by LPCVD using tetraethyl orthosilicate (TEOS) as a precursor. Subsequently, a 3-µm-thick PECVD oxide layer was deposited to reach the designed thickness of the upper cladding. The SEM image of the test structure after top SiO_2 cladding deposition is given in Fig. 2.9. The 2D modal field distribution of the waveguide structure confirms the negligible overlap of the optical field with the voids. Each deposition process was followed by thermal annealing at 1150^{o}C for 3 hours. The parameters for the top cladding deposition are listed in Table 2.5.

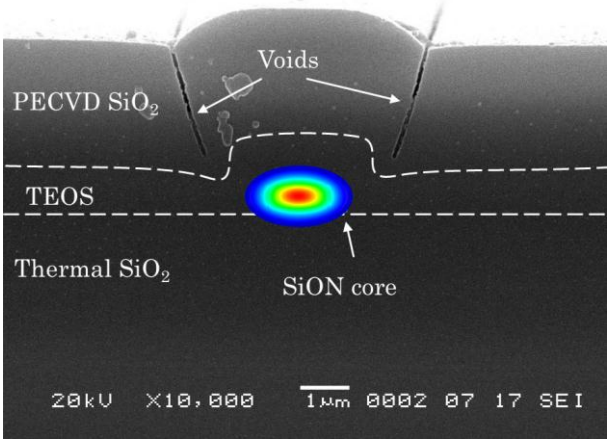

Fig. 2.9 SEM image of the test structure after top SiO_2 cladding deposition with 2D modal field distribution. The overlap of the optical field with the voids is negligible.

2.3 AWG parameters for OCT imaging

The axial resolution of an SD-OCT system using an AWG is determined by the effective bandwidth of the detected spectrum, which depends on both the bandwidth of the light source and the FSR of the spectrometer. Matching the bandwidth of the AWG transmission function with the bandwidth of the light source is the most economical configuration, since for a given source bandwidth the axial resolution will not improve if the bandwidth of the AWG transmission function is made much larger than this bandwidth, and vice versa. The maximum useful transmission bandwidth of an AWG is its FSR, which is valid for loss nonuniformity $\leq$ 3 dB. In practice, the FSR of an AWG is limited by the size of the device [Smi96]. By considering the design limitations, the optimum FSR values were chosen for each AWG design listed in Table 2.6 and Table 2.7, for retinal and dermal imaging, respectively. The corresponding axial resolution values were calculated by applying Eq. (1.13). In order to increase the FSR of AWG spectrometers, a tandem

configuration (cascaded) was applied which will be discussed in Section 2.6 in detail.

The choice for a maximum depth range is a compromise between various imaging performance parameters. Given a fixed size of the AWG imaging plane, according to (1.14) a larger imaging depth can be obtained by using an AWG with higher resolution; however this would result in a lower optical bandwidth and, hence, according to (1.13), lower spatial OCT resolution. Smaller spacing between adjacent waveguides results in an increased crosstalk and, consequently broader beam sizes (equivalent to the spot size *a* which goes into parameter ω in Eq. (1.17)) on the CCD and thereby more signal roll-off in depth. The optimum AWG wavelength resolutions and corresponding depth ranges are listed in Table 2.6 and Table 2.7, for retinal and dermal imaging, respectively.

Table 2.6: *AWG parameters and corresponding imaging range and axial resolution for retinal imaging.*

	AWG#1	AWG#2	AWG#3
λ_c (nm)	800	800	800
FSR (nm)	20	68	48
$\delta\lambda$ (nm)	0.16	0.4	0.1
z_{max} (mm)	1	~1.5	1.6
Δz in air (μm)	~14	~4	~6
Remarks	The first AWG design @800 nm	Diced output AWG (see Chapter 5)	Conventionally cascaded AWGs (see section 2.6.1)

Table 2.7: *AWG parameters and corresponding imaging range and axial resolution for skin imaging.*

	AWG#4	AWG#5	AWG#6
λ_c (nm)	1300	1300	1250
FSR (nm)	78	20	136
$\delta\lambda$ (nm)	0.4	0.4	0.8
z_{max} (mm)	1	1	~2.2
Δz in air (μm)	~19	~37	~7.5
Waveguide design # (from Table 2.3)	1	2	3
Remarks	The first AWG design @1300 nm	Non-birefringent AWG (see Chapter 5)	Diced output AWG (see Chapter 5)

For an SD-OCT system with an AWG spectrometer, the roll-off in depth is determined by the relative spectral content (i.e. FWHM of the transmission response of a single channel) of the AWG output channels. As the AWG spatially disperses the input light over the output plane of the second FPR, the spectral content is limited by the size of the output waveguides. However, this spectral content in a single output waveguide can be increased due to diffraction-limited focusing of the light onto the output channel, crosstalk between output waveguides, and fabrication imperfections which results in a degradation in signal roll-off. For an AWG-based SD-OCT system, light is sampled twice; firstly at the focal plane of the AWG by the discretely located output waveguides and secondly by the camera pixels. The first sampling due to AWG output channels adds an extra sinc factor to Eq. (1.15), which is the Fourier transform of the rectangular-shaped output waveguides. In the extra sinc term, caused by the AWG sampling, d_x is to be replaced by the width w_0 of the (tapered) output waveguide at its intersection with the focal plane of the AWG, and the reciprocal linear dispersion $\mathcal{R}$ is now defined as $\delta k/\Delta x$, where Δx is the spacing between adjacent output waveguides. Then, using the same conversions and substitutions that led from (1.15) to (1.17), the final formula of the extra sinc term becomes

$$\frac{\sin\left((w_o/\Delta x)(\pi z/2z_{\max})\right)}{(w_o/\Delta x)(\pi z/2z_{\max})}, \tag{2.6}$$

By inserting Eq. (2.6) into Eq. (1.17) the modified formula of sensitivity roll-off is obtained as

$$A(z)=\left[\frac{\sin(K\pi z/2z_{\max})}{(K\pi z/2z_{\max})}\right]\left[\frac{\sin(\pi z/2z_{\max})}{(\pi z/2z_{\max})}\right]\exp\left[-\frac{\pi^2\omega^2}{16\ln 2}\left(\frac{z}{z_{\max}}\right)^2\right], \tag{2.7}$$

where $K= w_o/\Delta x$ is the ratio of the width of the output waveguide to the separation between them at the focal plane of the AWG, see Fig. 2.10a. In order to avoid severe signal roll-off in depth, ω is chosen smaller than 1, which necessitates an adjacent-channel crosstalk value of less than 10 dB. The desired crosstalk value is achieved by setting the spacing between the output waveguides in the focal plane of the AWG spectrometers accordingly.

For maximum SNR, the AWG spectrometer loss is minimized by applying linear tapers at the interfaces of arrayed and input/output waveguides with the FPRs, as shown in Fig. 2.10a. Ideally, the gaps near the FPR between arrayed waveguides should approach zero in order to capture more light and, thereby, reduce the excess loss. This would, however, result in extremely sharp features that

cannot be accurately reproduced by our lithographic processes; therefore, the gap width was chosen to be 1 μm for the arrayed waveguides for all AWG spectrometers. The taper width of the input/output waveguides was determined as a compromise between loss and adjacent-channel crosstalk; the larger the taper width, the lower the excess loss and the higher the crosstalk, as shown in Fig. 2.10b, which is the simulation result of a typical AWG spectrometer.

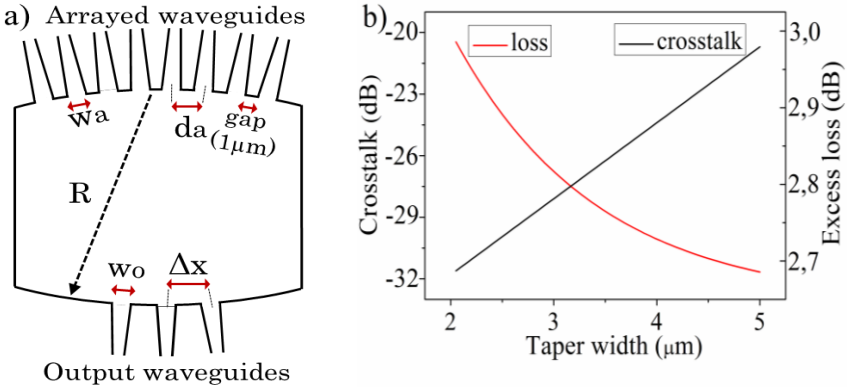

Fig. 2.10 (a) Geometry of the receiver side of the AWG (2nd FPR) and definition of parameters w_a, d_a, w_o, Δx, R: see Table 2.1, **(b)** adjacent crosstalk and excess loss versus output taper width, w_o.

As crosstalk arises from evanescent coupling between output waveguides, it decreases with increasing spacing. However, this leads to increased device size and, therefore, needs to be carefully designed. Acceptable minimum spacings between the arrayed waveguides and between the output waveguides were found by simulating device behavior using the 2-D BPM in order to have an excess loss value of $\leq$ 3 dB (for the central channels) and a crosstalk value of $\leq$ –20 dB. The simulation results of all devices confirm that our choice of taper width and waveguide spacing fulfills the above excess loss and crosstalk requirements.

2.4 AWG design

2.4.1 Geometrical parameters

The resolution and the FSR values of the AWGs are chosen depending upon the desired OCT imaging parameters as discussed in the previous section. The remaining geometrical design parameters of each AWG are calculated using standard AWG equations (section 2.1, Eqs. (2.2)-(2.4)) which are listed in Table 2.8 and Table 2.9, respectively, for the 800 nm and 1300 nm designs. The number of

arrayed waveguides is chosen in such a way that the diffracted light in the first slab is transferred into the second slab with minimum loss of image information.

Table 2.8: *Geometrical design parameters of the 800-nm AWG spectrometers.*

Parameters	AWG#1	AWG#2	AWG#3	
			Primary	Secondary
Diffraction order (m)	40	12	17	48
Focal length (R,mm)	11	14	0.2	14
Path length increment (ΔL, μm)	21.8	6.5	9.3	25.6
# arrayed waveguides (M)	500	510	10	480
# output channels (N)	125	170	3	165
Minimum bending radius (μm)	800	800	800	800
Arrayed waveguide spacing (d_a)	6	6.5	6	6.5
Output waveguide spacing (Δx, μm)	8	7	6	7
Taper width of arrayed waveguides (w_a, μm)	5	5.6	5.2	5.6
Taper width of input/output waveguides (w_o, μm)	3	4	5	4
Length of linear taper (μm)	400	500	200	300

Table 2.9 *:Geometrical design parameters of the 1300-nm AWG spectrometers.*

Parameters	AWG #4	AWG #5	AWG #6
Diffraction order (m)	17	65	9
Focal length (R, mm)	12	3.2	9.5
Path length increment (ΔL, μm)	15	57.4	7.6
# arrayed waveguides (M)	650	150	510
# output channels (N)	195	50	170
Minimum bending radius (μm)	800	1200	500
Arrayed waveguide spacing (d_a)	7	7	6.5
Output waveguide spacing (Δx, μm)	8	8	7
Taper width of arrayed waveguides (w_a, μm)	6	6.2	5.6
Taper width of input/output waveguides (w_o, μm)	4	5	6
Length of linear taper (μm)	200	200	500

2.4.2 BPM Simulations

As an example, two specific AWG spectrometers, namely AWG#1 in Table 2.6 (for 800 nm range) and AWG#4 in Table 2.7 (for 1300 nm range) will be analyzed in detail in order to emphasize the main design parameters. The performance of the AWGs is simulated using BPM. According to BPM simulations for the 800-nm

AWG, at the central channels, a crosstalk of -35 dB and an excess loss (with respect to a curved reference waveguide) of 2.6 dB were calculated. At the outermost channels these values are -27 and 5.35 dB, respectively. The 3-dB bandwidth was calculated as 0.052 nm. For the 1300-nm AWG, crosstalk values of -33 and -20 dB and excess loss values of 1.8 and 6.3 dB were simulated for the central and outermost channels, respectively. The 3-dB bandwidth was calculated as 0.22 nm. The simulation results are given in Fig. 2.11 and Table 2.11 shows a comparison of simulated and measured AWG parameters.

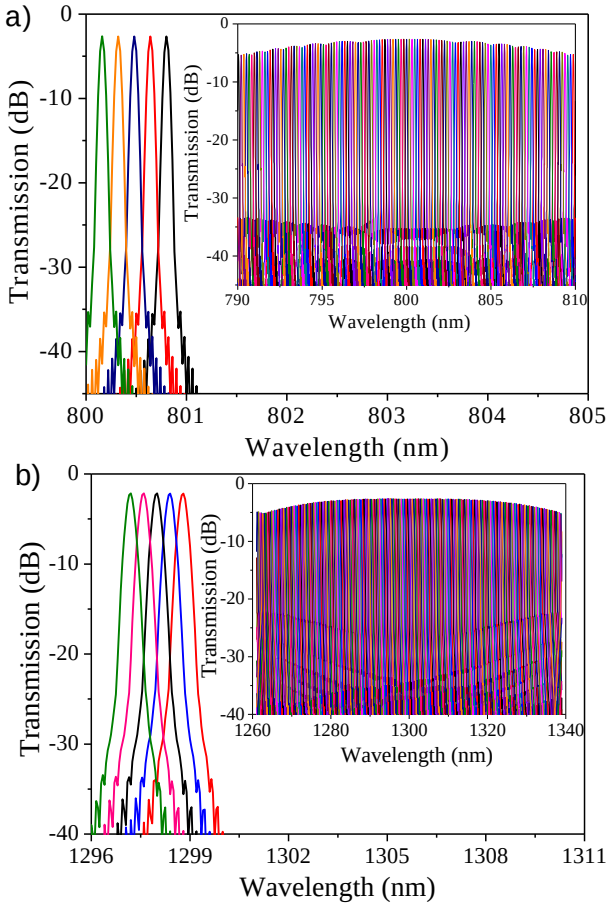

Fig. 2.11 AWG beam propagation simulation for TE-polarized light at the central channels for **(a)** the 800-nm AWG and **(b)** the 1300-nm AWG. The insets show the spectrum over the complete FSR of 20 nm and 78 nm, respectively.

2.4.3 Tolerance analysis

The AWG performance is affected mainly by the process non-uniformity and limitations in reproducibility. The refractive indices of core and cladding layers can have non-uniformities of up to ± 3×10^{-4} in refractive index, and the core layer can show thickness variations up to ± 0.5% over the wafer. The waveguide width can vary by ± 0.1 μm. The refractive index was measured by the prism-coupling method from a 7 cm × 7 cm area of a 100-mm wafer, which is the useful area for device fabrication. The reproducibility in thickness is ± 1.2% and in refractive index ± 1.5×10^{-3}, which is within the measurement error.

The simulation results of the effects of these process-dependent deviations are summarized in Table 2.10. A uniform change in effective refractive index emerges as a spectral shift in the transmission spectrum and a nonuniform change increases the overall crosstalk level. Although for both devices the maximum resulting variation of the effective refractive index of the waveguiding channel is low, an AWG is a very sensitive device and even small changes could lower the performance of the device dramatically. The central wavelength and the crosstalk are much more sensitive to variations in the core layer thickness and the waveguide width, than to variations in core and cladding refractive indices.

By exploiting the thermo-optic (TO) effect of SiON, the shift in central wavelength of the transmission spectrum can be compensated by heating the whole chip. The TO coefficient of SiON is reported as 2.35×10^{-5} / K in Ref. [Chu09]. Thus, a temperature rise of 5 K, for example, will increase the refractive index by $\Delta n \sim 10^{-4}$.

As a proof-of-concept, the TO effect was investigated only for the 1300-nm AWG, since the TO coefficient and the corresponding relative temperature-induced wavelength shift have the same order of magnitude for the 800 nm and 1300 nm wavelength ranges. Figure 2.12 shows the temperature-induced shift of the central wavelength of the AWG in the temperature range of 0-30 K.

Table 2.10: *Calculated effects of technological tolerances on AWG performance*

Parameters	**AWG @ 800 nm**			**AWG @ 1300 nm**		
	Δn_{eff} ($\times10^{-3}$)	$\Delta\lambda_c$ (nm)	$\Delta_{crosstalk}$ (dB)	Δn_{eff} ($\times10^{-3}$)	$\Delta\lambda_c$ (nm)	$\Delta_{crosstalk}$ (dB)
$\Delta w = \pm 0.1$ μm	1.7	0.92	6	1.85	1.63	9
$\Delta n_{core} = \pm 3\times10^{-4}$	0.4	0.22	0.5	0.3	0.26	1.2
$\delta d_{core} = \pm 0.5$ %	1.97	1.07	8	3.6	3.18	14
$\Delta n_{cladding} = \pm 3\times10^{-4}$	0.12	0.06	0.4	0.17	0.15	0.7

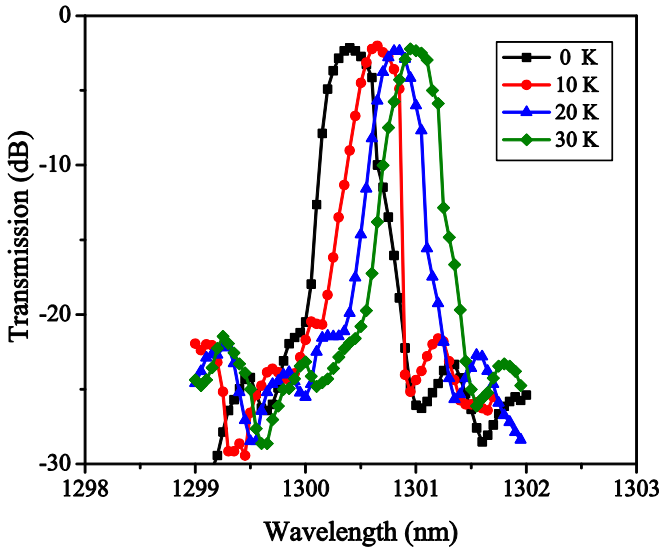

Fig. 2.12 Measured thermo-optic tuning characteristic of the 1300-nm AWG.

A wavelength shift of 0.65 nm for 30 K of temperature change, i.e., a shift rate of 0.022 nm/K was observed. With this shift rate, the experimental TO coefficient of SiON was obtained as 2.06×10^{-5}/K, which agrees well with the theoretical value. Using such AWG spectrometers in an on-chip OCT system require temperature stabilization of the AWG in order to prevent imaging degradations due to variations in ambient temperature.

The increase in crosstalk, also indicated in Table 2.10, reduces the device performance. Moreover, compensation of this type of performance degradation is not very easy or not even feasible. The fluctuations in the waveguide width and thickness of the core layer result in significant increments in the crosstalk levels of both devices. The tolerance analysis reveals that for a high-performance AWG, we need not only a good design but also a very good fabrication facility that provides waveguides with an effective refractive index within a tolerance lower than 10^{-4} in order to keep the shift in the transmission spectrum and the change in crosstalk lower than 0.2 nm and 2 dB for both devices, respectively.

The fiber-to-chip coupling loss was estimated to be about 3.5 and 5.5 dB/facet for the 800-nm and 1300-nm waveguides, respectively. This loss is mainly due to the difference in core size between the waveguides and the optical fibers. However, it is possible to reduce the coupling loss to 0.25 dB/facet by splicing the standard telecom fiber to a high-NA small-core fiber, as previously demonstrated [Wör07].

2.5 Characterization of AWG spectrometers

A straightforward procedure was used to characterize all AWG spectrometers. As an example, two specific AWG spectrometers, namely AWG#1 in Table 2.6 (for 800 nm range) and AWG#4 in Table 2.7 (for 1300 nm range) will be analyzed in detail in order to emphasize the main characterization steps and important performance parameters. More detailed design parameters of these AWG spectrometers are given in Table 2.8 and Table 2.9.

2.5.1 Measurement set-up

Optical transmission measurements were performed by coupling TE-polarized light from a supercontinuum light source (Fianium SC450) into the input waveguide with a single-mode polarization-maintaining (PM) fiber. The output signal was sent to an optical spectrum analyzer (iHR 550, Horiba Jobin Yvon) through a butt-coupled single-mode fiber. The schematic of the optical measurement set-up is depicted in Fig. 2.13.

The complete FSR was measured by moving the fiber successively along all output channels (step & optimize transmission for each channel). Results were reproducible within ±20%, the inaccuracy being mainly due to fiber-chip alignment errors. The transmission spectra measured at the output channels were normalized with respect to the transmission spectrum of a curved channel waveguide with the same radius and propagation length as the longest arrayed waveguide in the AWGs.

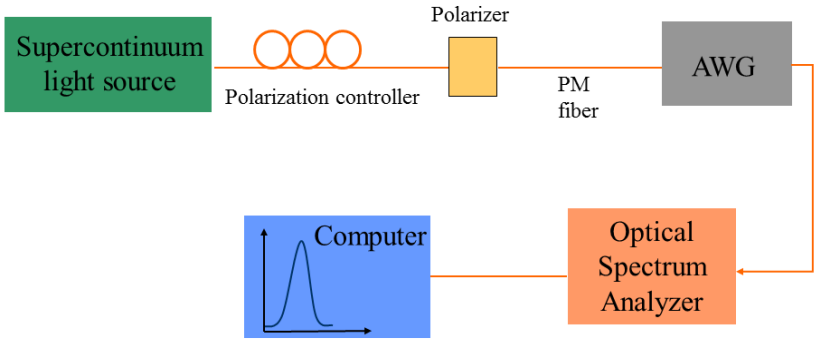

Fig. 2.13 Optical measurement set-up used to characterize the AWG spectrometers. PM refers to polarization maintaining.

2.5.2 Optical transmission measurements

The measured transmission spectra of the central output waveguides of the 800-nm AWG are displayed in Fig. 2.14a. The inset shows the complete set of 125 transmission spectra of the device. As predicted, each channel works as a band-pass wavelength filter. The measured values of resolution and FSR are consistent with the simulation results. However, a 10-dB difference between the simulated and measured crosstalk values was found. The relatively high crosstalk is attributed mainly to phase errors due to nonuniformity of the refractive index and thickness of the core layer, which was a major problem for the devices that were fabricated after a failure of PECVD and RIE machines.

Figure 2.14b displays the measured transmission spectra of the central output waveguides of the 1300-nm AWG. The inset of Fig. 2.14b represents the complete set of 195 transmission spectra of the device. The measured values of resolution and FSR are consistent with the simulation results. An 8-dB difference between the calculated and measured crosstalk values and a center wavelength shift of 2 nm was found due to the same cause as explained above for the 800-nm AWG. Table 2.11 provides the simulation and measurement results of the fabricated AWGs.

For both AWG spectrometers, we observed random differences between the peak values of the transmission spectra of the different output channels, arising from a limited reproducibility of the used measurement method. The optical transmission of each output channel was measured using a single butt-coupled fiber which had to be repositioned to the next channel after each measurement. Although the fiber-chip coupling efficiency was maximized each time, the intensity variations were not eliminated completely. However, for the OCT imaging measurements the light coming out of the output channels will be imaged onto the camera by using free-space coupling, which eliminates fiber-chip-coupling related problems completely if the variations are not due to the facet quality.

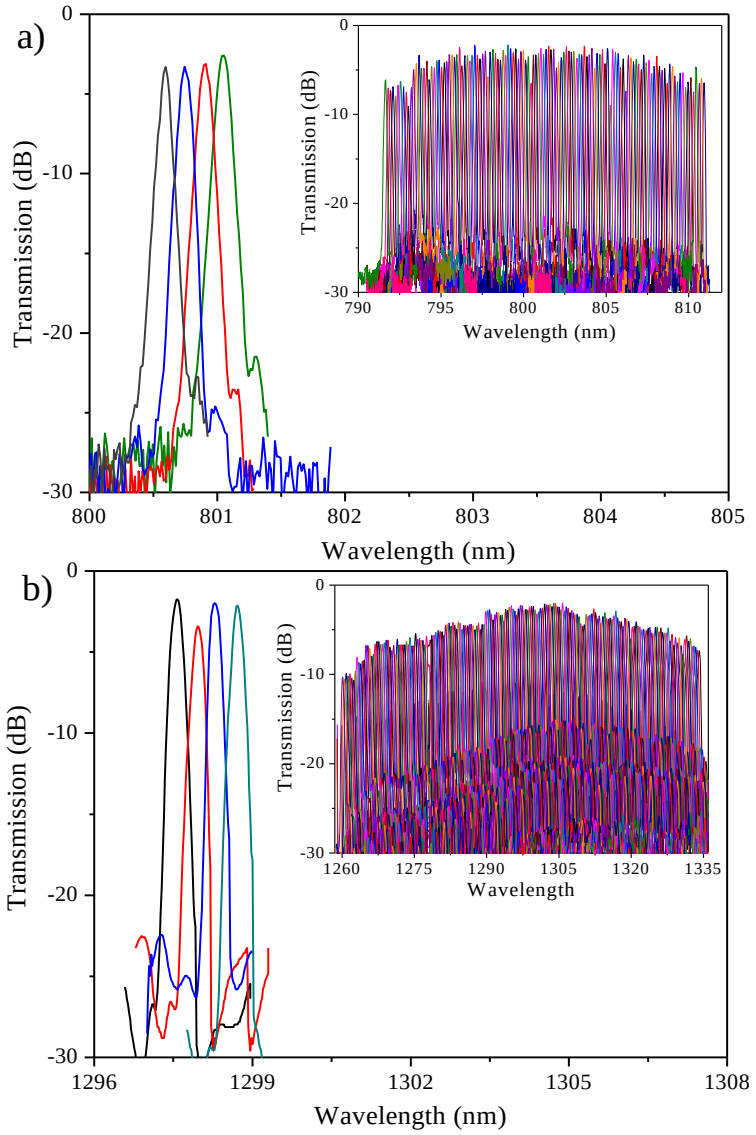

Fig. 2.14 AWG performance for TE-polarized light at the central channels for **(a)** the 800-nm AWG and **(b)** the 1300-nm AWG. The insets show the spectrum over the complete FSR of 19.4 nm and 77 nm, respectively. All spectra are normalized with respect to that of a curved reference waveguide.

Table 2.11: *Measurement and simulation results of fabricated AWG spectrometers.*

Parameter		AWG @ 800 nm		AWG @ 1300 nm	
		Simulated	**Measured**	**Simulated**	**Measured**
Channel spacing (nm)		0.16	0.16	0.4	0.4
FSR (nm)		20	19.4	78	77
Polarization-dependent shift (nm)		0.55	0.5	0.6	0.5
Non-adjacent crosstalk (dB)	Center	-35	-22	-33	-25
	Outermost	-27	-18	-20	-16
Excess loss (dB)	Center	2.6	3.2	1.8	2.5
	Outermost	5.35	6.5	6.3	8
3-dB bandwidth (nm)		0.052	0.07	0.22	0.23

2.5.3 Polarization dependency of AWGs

An AWG is polarization independent if the propagation constants for the fundamental TE and TM modes of its arrayed waveguides are equal. However, due to the (stress-induced) material birefringence, the effective refractive indices and thereby the propagation constants for TE and TM modes will be different which results in a polarization-dependent focus shift for a single wavelength. The formula for the focus shift can be extracted by solving Eq. (2.1) under the assumption of single input and single output waveguide (i = 1. j = 1). It is given as

$$\Delta x_{TE-TM} = \Delta x_{TE} - \Delta x_{TM} = \frac{R\Delta L\Delta n_c}{2n_s d}, \tag{2.8}$$

where $\Delta x_{TE\text{-}TM}$ is the polarization-dependent focus shift for a single wavelength and $\Delta n_c = n_{TE} - n_{TM}$ is the difference in effective refractive index of the core layer for TE and TM polarizations. The derivations of the formulas are given in Appendix A1.

It is also possible to extract the polarization-dependent center wavelength shift by differentiating Eq. (2.2) with respect to n_c and multiplying by the differential Δn_c, which results in

$$\Delta n_c = n_{TE} - n_{TM} = \frac{m\,\Delta\lambda}{\Delta L}, \tag{2.9}$$

Using a typical material birefringence of 1.5×10^{-3}, the polarization-dependent wavelength shift was calculated with a 2-D BPM as 0.55 nm and 0.6 nm for the 800-nm and 1300-nm AWG, respectively as shown in Fig. 2.15. From transmission measurements of the 800-nm AWG and 1300-nm AWG, a polarization-dependent central-wavelength shift of $\Delta\lambda$ = 0.5 nm was measured for both devices which corresponds to an effective refractive index difference between the two polarizations, i.e. the waveguide birefringence, of $\Delta n_c \cong 0.9 \times 10^{-3}$ and $\Delta n_c \cong 0.6 \times 10^{-3}$, according to Eq. (2.9), respectively.

The performance of an OCT system using a polarization-dependent AWG spectrometer could degrade dramatically if the incident light has a mixed polarization state since a polarization-dependent AWG images a spectral peak at a given wavelength onto different positions on the image plane for TE and TM polarizations. The measured amplitude interference spectrum $M(\lambda)$ for a specific polarization is the convolution of the broadband response (the transmission envelope) $B(\lambda)$ and the single-wavelength response $S_{\lambda 0}(\lambda)$ of the AWG [Smi96]. The depth information $D(z)$ which is the Fourier transformation (FT) of $M(\lambda)$, becomes

$$D(z) = \left| \mathcal{F}_{k \to z} \left\{ M(\lambda) \right\} \right| = \left| \mathcal{F}_{k \to z} \left\{ B(\lambda) \right\} \cdot \mathcal{F}_{k \to z} \left\{ S_{\lambda 0}(\lambda) \right\} \right|, \qquad (2.10)$$

For a pure TE or TM polarization, $S_{\lambda 0}(\lambda)$ has a single Gaussian peak, thus $\mathcal{F}\{S_{\lambda 0}(\lambda)\}$ is a Gaussian function which does not affect the uniform roll-off in $D(z)$. In contrast, for mixed TE and TM polarization, $S_{\lambda 0}(\lambda)$ exhibits two Gaussian peaks. For simplicity, the response to mixed TE and TM polarization will be derived in the k-domain and the final formula will be converted to wavelength at the end.

If the single-frequency response function (SFRF) of the AWG for TE-polarized light is $f(k)$, the SFRF for TM-polarized light then becomes, $f(k+\Delta k_{TE\text{-}TM})$, where $\Delta k_{TE\text{-}TM}$ is the separation between TE and TM peaks in wavenumber. The SFRF for the case of mixed polarization can be expressed as

$$S_{ko}(k) = a \cdot f(k) + f(k + \Delta k_{TE-TM}), \qquad (2.11)$$

where α is the ratio of TE and TM peak intensities. The FT of Eq. (2.11) yields

$$\begin{aligned}\mathcal{F}\{S_{ko}(k)\} &= \mathcal{F}\{a\cdot f(k)+f(k+\Delta k_{TE-TM})\}\\ &= \int_{-\infty}^{\infty} a\cdot f(k)e^{-2\pi ikz}dk + \int_{-\infty}^{\infty} f(k+\Delta k_{TE-TM})e^{-2\pi ikz}dk\\ &= a\cdot\mathcal{F}(z) + \int_{-\infty}^{\infty} f(k')e^{-2\pi i(k'-\Delta k_{TE-TM})z}d(k'-\Delta k_{TE-TM}),\\ &= a\cdot\mathcal{F}(z) + \int_{-\infty}^{\infty} f(k')e^{-2\pi i(k')z}e^{-2\pi i(\Delta k_{TE-TM})z}d(k')\\ &= a\cdot\mathcal{F}(z) + \mathcal{F}(z)e^{-2\pi i(\Delta k_{TE-TM})z}\end{aligned} \qquad (2.12)$$

where $\mathcal{F}(z)$ is the FT of $f(k)$, and $k'= k+\Delta k_{TE\text{-}TM}$. The final form of $\mathcal{F}\{S_{ko}(k)\}$ is

$$\mathcal{F}\{S_{ko}(k)\} = \mathcal{F}(z)(a+e^{-2\pi i(\Delta k_{TE-TM})z}), \qquad (2.13)$$

The depth information $D(z)$ is calculated as

$$\begin{aligned}D(z) &\propto \left|\mathcal{F}\{S_{ko}(k)\}\right| = \sqrt{\mathcal{F}\{S_{ko}(k)\}\mathcal{F}\{S_{ko}(k)\}^{*}}\\ &\propto \sqrt{(a+e^{-2\pi i(\Delta k_{TE-TM})z})(a+e^{2\pi i(\Delta k_{TE-TM})z})}\,|F(z)|,\\ &\propto \sqrt{1+2a\cos(2\pi\Delta k_{TE-TM}z)+a^2}\,|F(z)|\end{aligned} \qquad (2.14)$$

By applying wavenumber to wavelength conversion ($\Delta k=2\pi\Delta\lambda/\lambda^2$), Eq. (2.14) becomes

$$D(z)\propto\mathcal{F}\{S_{\lambda 0}(\lambda)\} = |\mathcal{F}(z)|\sqrt{1+2a\cos(2\pi z\Delta\lambda_{TE-TM}/\lambda^2)+a^2}, \qquad (2.15)$$

The cosine term modulates the roll-off curve with a frequency defined by $\Delta\lambda_{TE\text{-}TM}$ (wavelength separation between TE and TM peaks), which causes signal fading at specific depths as depicted in Fig. 2.16.

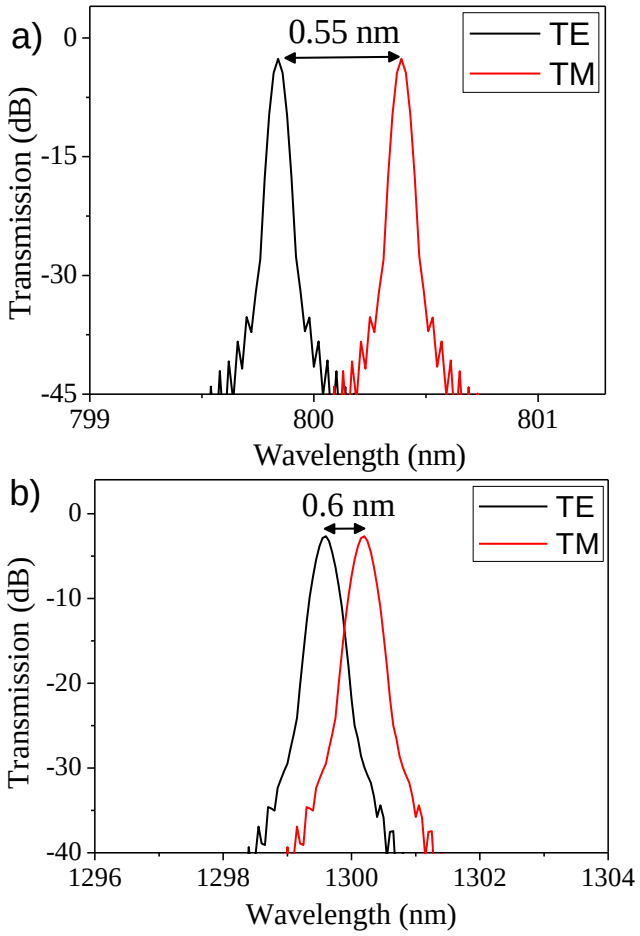

Fig. 2.15 Simulation results for the polarization-dependent wavelength shift for **(a)** the 800-nm AWG and **(b)** the 1300-nm AWG.

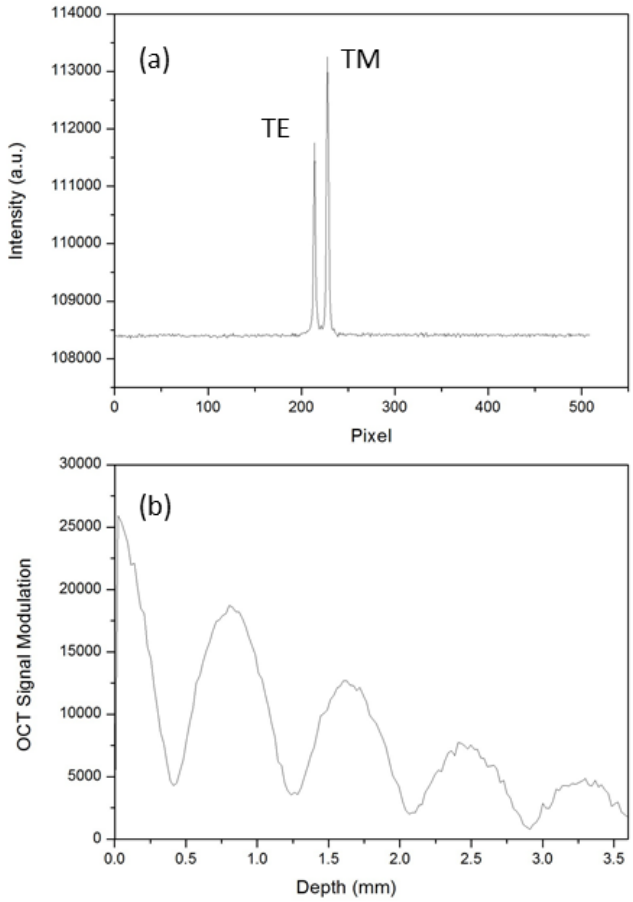

Fig. 2.16 (a) The single-wavelength response of an AWG for unpolarized light. **(b)** Corresponding Fourier transform of the spectrum given in (a).

2.6 Advanced AWG designs for OCT performance improvement

Combining high resolution and large FSR in a single AWG is highly desirable for numerous applications, e.g. high-resolution OCT systems, however it is rather difficult to implement. By applying different approaches, such as cascading several AWGs, the limitations on resolution and FSR of an AWG can be overcome. A cascading configuration enables us to design flexible WDM systems with high channel count and channel spacing [Tak01, Tak99, Tak00, Tak05]. In this section we will discuss two possible cascading methods; namely the 'conventional' way, and cascading by exploiting the cyclic frequency response of the AWGs. Additionally a new flat-top broadband AWG design will be discussed which can serve as a primary filter in the conventional cascading method.

2.6.1 Conventionally cascaded AWG design

This method is based on the use of two stages of the conventional AWG structure with different resolution and FSR values; the first stage, called the primary AWG and the second stage, called secondary AWG, as illustrated in Fig. 2.17. This method is commonly used for high-density WDM systems, therefore we called it the 'conventional' method.

The primary AWG, a 1 × *N* device, slices the whole spectrum of interest into wide *N* sub-passbands while the *N* secondary AWGs, 1 × *M* devices, reslice the wide passbands into narrow passbands. In this way the overall configuration will have a wide FSR with narrow channel spacing. The center wavelength of each of secondary AWG coincides with that of the corresponding primary filter passband. The main passband loss generated by the cascaded configuration consists of the loss at the primary and secondary filters. In addition to this loss, at the passband crossing points of the primary AWG, an extra loss will be introduced for the corresponding secondary AWG passbands due to Gaussian-like transmission response of the AWG. Therefore it is desirable to have a primary filter having a transfer function approximating a rectangular shape as much as possible.

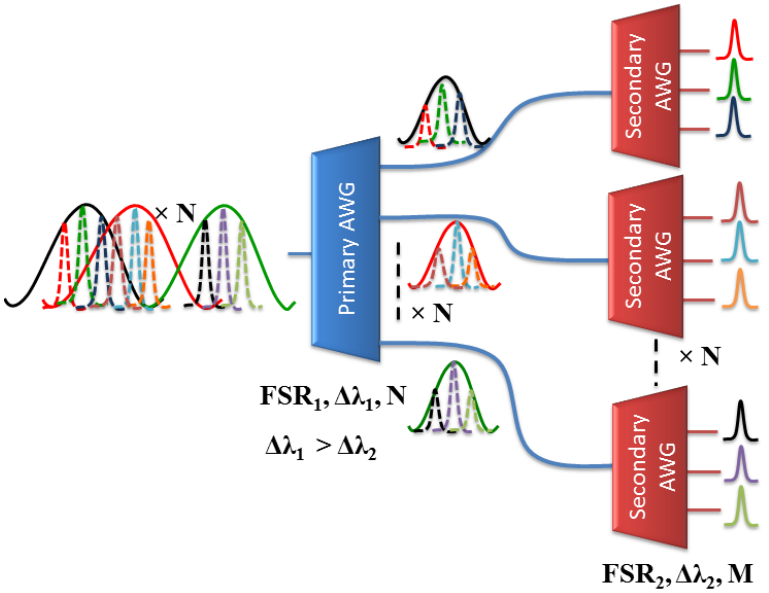

Fig. 2.17 Schematic diagram of the conventionally cascaded AWG configuration. *N* and *M*, respectively, indicate the number of primary and secondary filter output waveguides.

Using the conventional method, we designed a cascaded AWG system operating at the 800 nm wavelength range with the design parameters and the mask layout given in Table 2.12 and Fig. 2.18, respectively. The overall device size is 4.8 cm×2.6 cm, which is rather large.

Table 2.12: *Design parameters for the cascaded AWG at 800 nm.*

	Primary AWG	**Secondary AWG**
FSR (nm)	48	16.5
Channel spacing (δλ, nm)	16	0.1
# of output channels	3	165
Device size (cm^2)	0.08×0.5	2.7×3

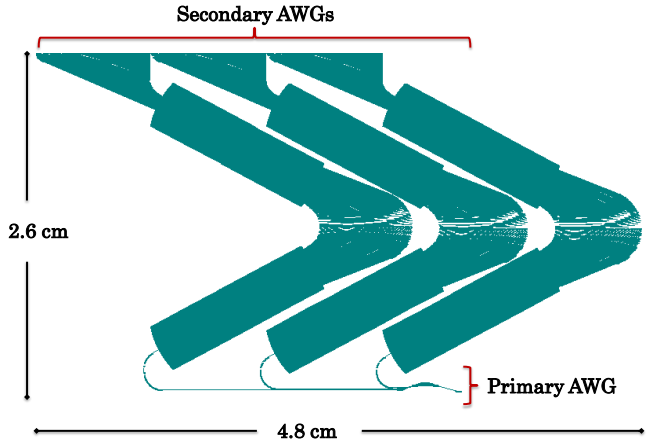

Fig. 2.18 Mask layout of the conventionally cascaded AWG at 800 nm. The overall device size is 4.8 cm×2.6 cm.

2.6.2 Cascaded AWG systems by using the cyclic FSR nature of AWG

An AWG has a cyclic transmission characteristic in that all wavelengths with a spacing equal to the FSR are transmitted simultaneously to a single output waveguide. Considering the size and loss problems of the conventional method, we proposed a new cascading technique with the use of the cyclic nature of the AWG response, which can provide a much smaller system size and better overall performance. Instead of the primary AWG having wide flat passbands, it could have narrow closely spaced passbands (that equal the final desired channel spacing) that repeat N times in the desired wavelength range, using the frequency-cyclic nature of the AWG as illustrated in Fig. 2.19. The channel spacing of the secondary AWGs should be equal to the FSR of the primary AWG. In this configuration the FSR of the secondary AWGs defines the FSR of the overall configuration whereas

the channel spacing (resolution) of the primary AWG defines the overall system resolution. In this method, the requirements on resolution and passband flatness of the secondary AWGs are relatively low, as the components in their prefiltered input spectra can be easily separated with very low adjacent-channel crosstalk. Moreover, the complete device size will be much smaller compared to one that is designed with the conventional cascading method, since high-resolution AWGs are generally bigger than low-resolution AWGs so a system with one high-resolution AWG and multiple low-resolution AWGs can be smaller in overall size than one with a low-resolution AWG and multiple high-resolution AWGs. Although this method promises a much better overall performance, for the high-wavelength resolution it is more sensitive to fabrication tolerances (i.e. thickness and refractive index nonuniformity of the core layer) than the conventional system since the fabrication-related wavelength shift in the primary and secondary AWGs should match exactly in order to obtain the desired wavelength resolution. Using this method in OCT systems is more beneficial since the FSR of an AWG (thereby the wavelength resolution) is constant in frequency which means that the spectrum is resolved in constant wavenumber Δk intervals which is appropriate for the OCT signal processing that transforms the spectrum from k to z domain.

Using this new cascading method, we designed two cascaded AWG systems operating at 800 nm and 1250 nm wavelength ranges with the design parameters given in Table 2.13 and Table 2.14, respectively. The mask layouts are given in Fig. 2.20. The overall device sizes are small compared to the conventionally cascaded AWG system at 800 nm. The characterization of the devices was performed with the same method as explained in Section 2.5. The central channel of each secondary AWG was measured in order to investigate the resolution of the final devices which are shown in Fig. 2.21 and Fig. 2.22. In Fig. 2.21 there is a shift in the center wavelength position of the AWG#3 which is due to the cyclic nature of the primary AWG. In Fig. 2.2. we observed a random behavior in terms of channel spacing and as well as the positioning of each peak which we attribute to the non-uniformity of the SiON layer thickness and refractive index. Additionally we observed randomly distributed scattering clusters in the top SiO_2 cladding layer which could induce effective refractive index fluctuations.

Table 2.13: *Design parameters for the cascaded AWG at 800 nm.*

	Primary AWG	**Secondary AWG**
FSR (nm)	0.3	30
Channel spacing (δλ, nm)	0.1	0.3
# of output channels	3	100
Device size (cm^2)	1.2×1.3	2.2×1.25

Table 2.14: *Design parameters for the cascaded AWG at 1250 nm.*

	Primary AWG	Secondary AWG
FSR (nm)	1.25	131.25
Channel spacing (Δλ, nm)	0.25	1.25
# of output channels	5	105
Device size	1.2 cm×1.2 cm	0.8 cm×2.1 cm

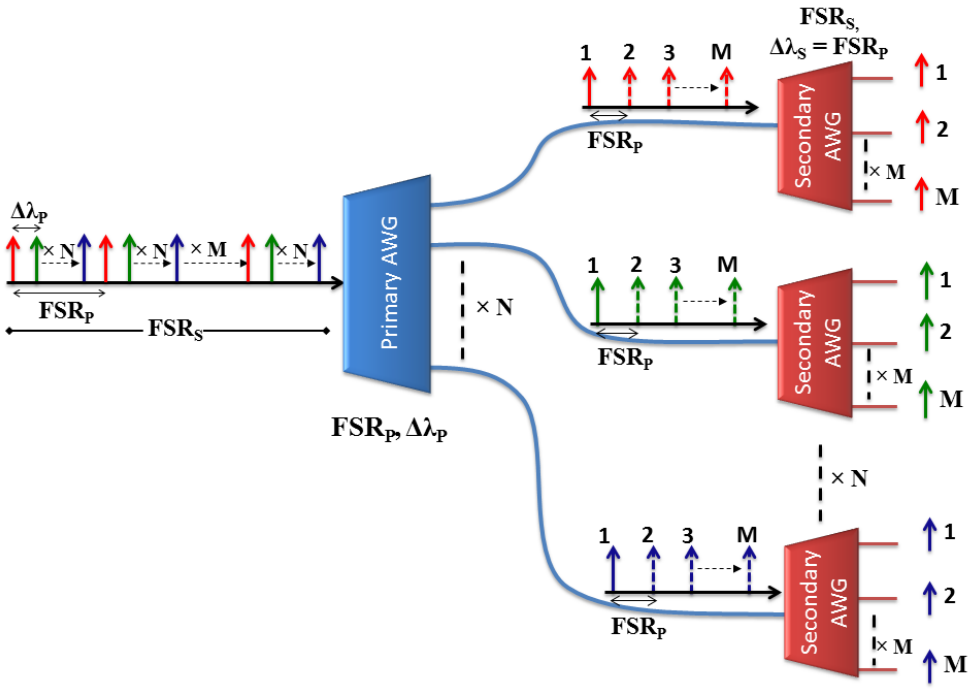

Fig. 2.19 Schematic diagram of the cascaded AWG configuration using the cyclic nature of the AWG. FSR_P, and FSR_S indicate the FSR of the primary and secondary AWGs, respectively, while $\Delta\lambda_P$ and $\Delta\lambda_S$ are the channel spacings of the primary and secondary AWGs, respectively. $\Delta\lambda_S$ equals FSR_P. The combined system has a free spectral range FSR_S and a resolution $\Delta\lambda_P$.

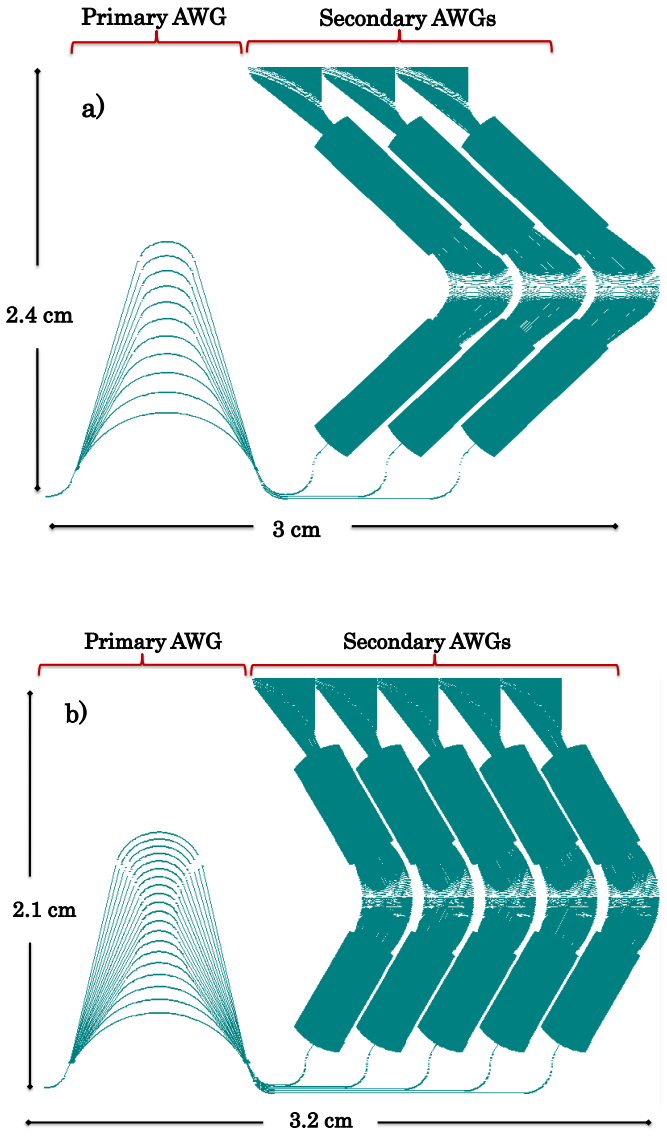

Fig. 2.20 Mask layout of the cascaded AWGs using the AWG cyclic nature at **(a)** 800 nm and **(b)** 1250 nm. The overall device size is 3 cm×2 cm and 3.2 cm×2.1 cm, respectively.

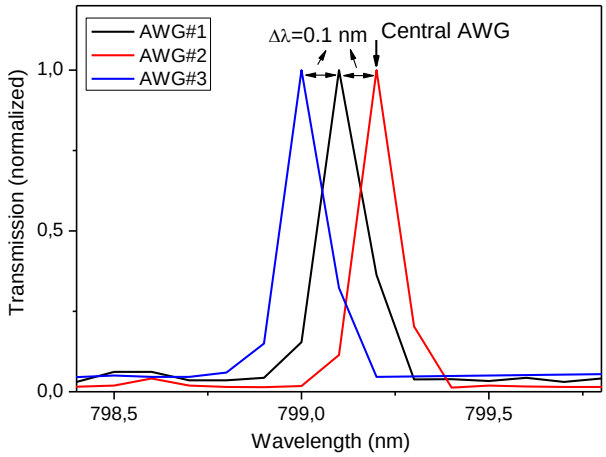

Fig. 2.21 Measurement results of the central channels of each secondary AWG of the cascaded system using the AWG cyclic nature at 800 nm. The separation between peaks is 0.1 nm, as given by the designed resolution of the primary AWG. However, the position of the AWG#3 peak does not correspond to the design. which is due to the cyclic behavior of the primary AWG.

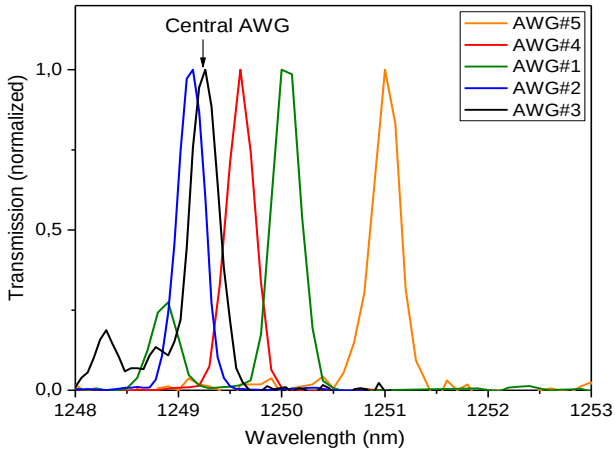

Fig. 2.22 Measurement results of the central channels of each secondary AWG of the cascaded system using the AWG cyclic nature at 1250 nm. The behavior of the overall system is random, i.e. there is no constant wavelength separation between them. Additionally, the center positions of the peaks do not correspond to the design: AWG#1 should have the lowest center wavelength whereas the center wavelength of AWG#5 was designed to be the largest. The discrepancy is attributed to thickness and refractive index nonuniformity of the core layer.

2.6.3 Broad-band flat-top AWG design

Although very-high-density WDM systems have been demonstrated, high loss and small passband due to the Gaussian transfer function of the primary filters are still substantial problems of the conventionally cascaded systems. In order to solve these problems flat-passband and low-loss primary AWGs are essential. Takada *et al.* have demonstrated a partially integrated low-loss multiplexer/demultiplexer configuration by cascading bulky thin-film interference filters as primary filters and five AWGs as secondary filters in order to reduce the overall system loss [Tak02[c]]. Although the loss decreased considerably, the thin-film interference filters were still not integrated on chip, which is a typical bottleneck for such filters.

There is a strong need for AWGs with low-loss and box-like passbands over a broad spectral range. Such AWGs are also known as band demultiplexers which are very useful in both dense and coarse wavelength-division-multiplexed systems. Several approaches have been proposed to implement AWGs having such a flat-top response [Ame96, Oka95, Oka96], however most have the drawbacks of increased insertion loss and large device size. Doerr *et al.* demonstrated a novel broad-band flat-top AWG design consisting of two waveguide grating routers, interconnected by a third one of non-standard design. [Doe03[a]]. Despite the impressive device performance, the device size was 88 × 5.4 mm^2 which is rather large for further component integration, e.g. cascaded AWG systems. Inoue *et al.* demonstrated a 20-nm-spacing 4-channel coarse wavelength-division-multiplexing filter which comprises a total of 16 Mach-Zehnder interferometer (MZI) stages [Ino02]. Although the filter had the advantages of low loss, low crosstalk, and a wide passband, the device size was 15 × 71 mm^2.

A very effective method for increasing the passband width without introducing intrinsic loss is the so-called MZI-synchronized AWG in which the closely spaced dual-output waveguides of an asymmetrical MZI together form the input waveguides of the AWG, thus generating an input light spot that shifts with wavelength [Dra95, Doe02, Doe03[b]] as illustrated in Fig. 2.23a. The term "synchronized" refers to the FSR of the MZI being equal to the wavelength-channel spacing of the AWG, so that the input light spot for the AWG makes a full 'sweep' in position along the x-direction for each AWG wavelength channel. This synchronous movement of its input spot compensates the dispersion of the AWG for the wavelength range contained in one wavelength channel, thus imaging all these wavelengths at the same output waveguide. Since the FSR of the MZI is equal to the wavelength-channel spacing of the AWG, the resulting device has a flattened passband for all wavelength channels. The MZI configuration given in Refs. [Dra95, Doe02, Doe03[b]] was constructed by using a Y-junction coupler for the first

coupler and a 2×2 directional coupler for the second coupler. The drawbacks of this configuration are excess loss and limited bandwidth due to the Y-junction coupler and the directional coupler, respectively.

An alternative for the aforementioned couplers is to take advantage of wavelength-insensitive 3-dB balanced couplers which can be realized by cascading two conventional couplers in a Mach-Zehnder configuration with a relative phase shift of 2θ introduced between them [Lit97], as shown in Fig. 2.23b. These couplers are very good candidates for broad-spectral-range MZI-synchronized AWGs with a maximally flat response with respect to deviations in wavelength, polarization, or uniform fabrication over a broad spectral range, with no excess loss. A detailed analysis of these couplers will be given in Chapter 3.

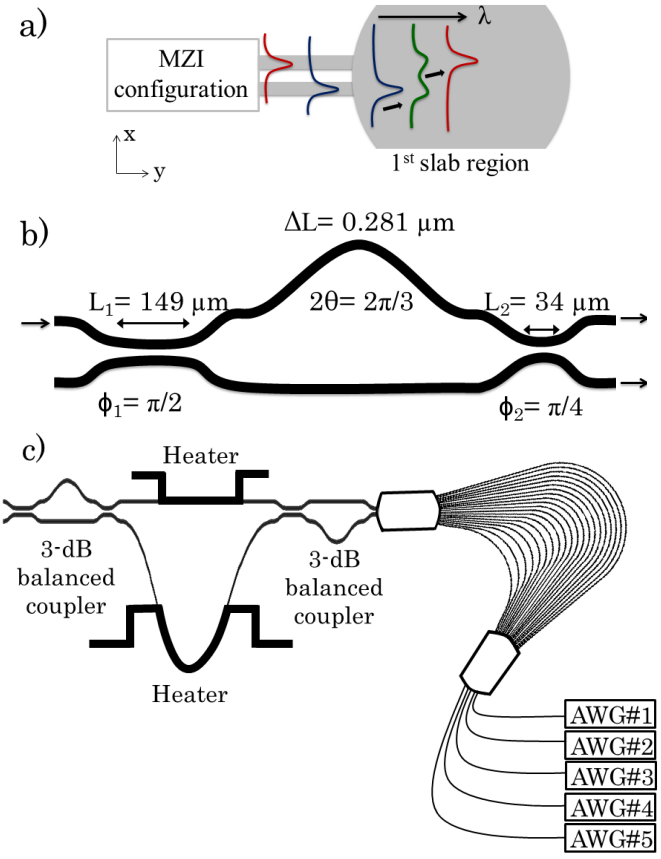

Fig. 2.23 (a) Change in optical field at the MZI and 1st slab region interface of the AWG, as the wavelength is changed. **(b)** Design parameters of the 3-dB balanced coupler. **(c)** Schematic of the cascaded AWG system with a MZI-synchronized AWG using 3-dB balanced couplers. Electrical heaters are placed on both arms of the MZI.

In this section we present a new synchronized design for flattening the passband of an AWG over a broad spectral range of 90 nm without any extra loss. A wavelength-insensitive 3-dB balanced coupler is designed to be used in duplicate in the MZI [Lit97]. The phase deviation created by one of the balanced couplers is canceled by flipping the other coupler around. Using these components, a 5-channel, 18-nm-spacing MZI-synchronized AWG is designed and a 0.5-dB bandwidth greater than 12 nm over 90 nm spectral range is demonstrated with an overall device size of 11 × 3 mm^2. The relative phase difference between the two MZI arms due to the processing fluctuations is compensated by employing the thermo-optic effect to tune the synchronized MZI. The applicability of this approach is demonstrated by the design and realization of a cascaded AWG system, which consists of this flat-top 1×5 AWG as a primary filter and five 1×51 AWGs with a 0.4-nm channel spacing as secondary filters. The FSR and the channel spacing of both, primary and secondary AWGs are chosen arbitrarily in order to prove the feasibility of the proposed design. Our configuration is advantageous due to its simple fabrication and full integration. Figure 2.23c shows the schematic configuration of the cascaded AWG system with synchronized MZI design using 3-dB balanced couplers. Such low-loss, broad-spectral-range AWGs are very desirable for high-density cascaded multiplexer/demultiplexer systems.

The splitting ratio at the output of a Mach-Zehnder-type interferometric coupler as shown in Fig. 2.23b is given by [Lit97]

$$S = \cos^2(\theta)\sin^2(\phi_1 + \phi_2) + \sin^2(\theta)\sin^2(\phi_1 - \phi_2) \qquad (2.16)$$

where ϕ_1 and ϕ_2 are the half phase differences between the fundamental and first-order system modes existing in the parallel-waveguide coupler sections of each directional coupler, and $2\theta = \beta(\lambda)\Delta L$ is the relative phase delay introduced in the uncoupled section by the path length difference ΔL and the propagation constant of the waveguide mode $\beta(\lambda)$. Reference [Lit97] specifies that in order to obtain a 3-dB coupler with a maximally flat wavelength response, the parameters can be chosen as $\phi_1 = \pi/2$ (full coupler), $\phi_2 = \pi/4$ (3-dB coupler), and $2\theta = 2\pi/3$.

The gap in the directional couplers was chosen as 1 μm. The FSR and wavelength resolution $\Delta\lambda$ of the primary flat-top AWG spectrometer were chosen as 90 nm and 18 nm, respectively, whereas for the secondary AWGs these values were 20.4 nm and 0.4nm, respectively. SiON channel waveguides with 1.8 μm width and 1 μm height were used for the AWG spectrometers and the MZI (Waveguide design#3 in Table 2.3) with an effective refractive index of 1.4822.The ΔL_{AWG} and grating order were 11.79 μm and 14, respectively. The primary and the secondary AWGs were on the same chip with an overall size of 4.5×1.5 cm^2.

Beam propagation simulations were performed for designing and optimizing the balanced couplers. The lengths of the straight coupler sections, were calculated as L_1 = 149 μm and L_2 = 34 μm, and the delay length was found to be ΔL = 0.281μm, as summarized in Fig. 2.23b. The simulated splitting ratio between the two arms stays constant over 90 nm bandwidth for both couplers, as shown in Fig. 2.24a. In order to have a flat passband for all output channels, the channel spacing of the AWG should be equal to the FSR of the MZI, which is given as

$$FSR_{MZI} = \frac{\lambda_c^{\,2}}{n_{e\,ff}\,\Delta L_{MZI}}, \tag{2.17}$$

where λ_c is the center wavelength, n_{eff} is the effective refractive index of the waveguide mode, and ΔL_{MZI} is the path length difference. Therefore, assuming that the MZI and arrayed waveguides have the same effective refractive index, the MZI should have a path length difference of

$$\Delta L_{MZI} = N \times \Delta L_{AWG}, \tag{2.18}$$

where N is the number of output channels of the AWG and ΔL_{AWG} is the constant length increment between adjacent arrayed waveguides. The excess loss decreases monotonically as the gap between waveguides in the second 3-dB balanced coupler of the MZI configuration becomes narrower, because the excess loss originates from the field mismatch between an even mode in the second 3-dB balanced coupler and a fundamental mode in the output waveguide at the center wavelength. Therefore, the gap between waveguides in the second 3-dB balanced coupler was arranged to be 0.8 μm by replacing its bent output waveguides by a small extension of the straight section L_2 from 34 μm to 40 μm. The performance of the reconfigured coupler is similar to the original one.

Due to the energy distribution among the diffraction orders in a cyclic AWG, i.e. FSR = $N \times \Delta\lambda$, the peripheral output waveguides suffer almost 3 dB more loss than the center waveguide (i.e. loss non-uniformity) [Smi96], thereby in a cascaded system the loss non-uniformity of the secondary AWGs will be at maximum equal to the 3 dB of a cyclic AWG. For the primary AWG design, the loss around the crossing points with the adjacent waveguides was reduced by designing the passband width in such a way that the adjacent channels overlap around the 3-dB down point in order to have a uniform intensity distribution for the complete cascaded system. In principle, using a non-cyclic AWG with a much larger FSR could result in a loss non-uniformity smaller than 3 dB, however, at the expense of a larger device size.

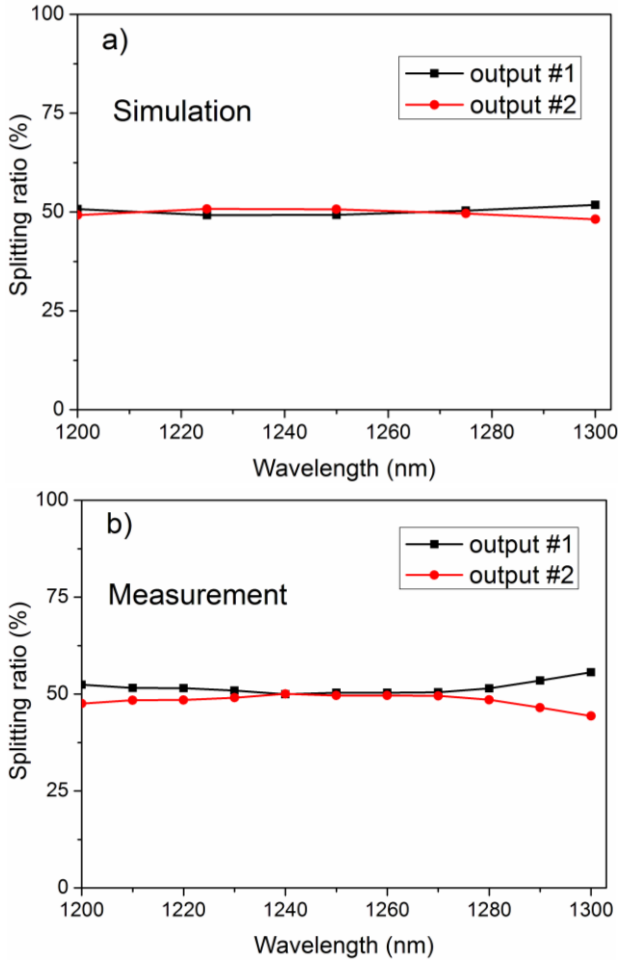

Fig. 2.24 (a) Simulation and **(b)** measurement result of the 3-dB balanced coupler. The wavelength dependence of the coupler increases at longer wavelengths due to processing fluctuations.

The measurements on both the individual 3-dB balanced couplers and the cascaded AWG system were performed with the same measurement set-up shown in Fig. 2.11, by coupling TE-polarized light from a broadband source alternatively into the 3-dB balanced coupler or the synchronized AWG with a single-mode polarization-maintaining fiber. The transmission spectra measured at the output waveguides of the different investigated structures were normalized with respect to the transmission of a straight channel waveguide. The measured spectra of the 3-dB balanced coupler are given in Fig. 2.24b. Due to fluctuations in the fabrication process, the core refractive index turned out to be slightly higher than intended, which led to a degradation of the performance of the 3-dB balanced coupler,

especially at longer wavelengths. The new core effective refractive index for TE was calculated as 1.548 from the measured central wavelength shift of the MZI-synchronized AWG. A simulation with a beam propagation method, using the increased core refractive index showed a similar performance decrease. In addition, at wavelengths where the splitting ratio is not exactly 3-dB, the coupler causes an additional phase shift between its outputs, which may cause reduced synchronized-AWG performance in terms of passband symmetry and excess loss at the outer channels.

The MZI-synchronized AWG was characterized using the aforementioned measurement procedure. The measured spectra are displayed in Fig. 2.25a. A 0.5-dB bandwidth of 12 nm and a central excess loss value of 1 dB were measured. A central wavelength shift of 7 nm with respect to the designed value was observed, corresponding to the same effective refractive index of the core of 1.548 that explains the measured performance of the 3-dB balanced coupler. At longer wavelengths the performance of the synchronized AWG decreased due to degraded performance of the 3-dB couplers, which was verified by the BPM simulations shown in Fig. 2.25a by dashed lines for the center and the 5^{th} output channels.

In order to overcome fabrication-related performance degradation of the MZI-synchronized AWG, chromium electrical heaters were placed on both arms of the MZI. These heaters control the phase delay between the modes in the two waveguides and, thus, the field distribution at their junction with the AWG input free-propagation region, and thereby also the AWG passband shape. Figure 2.25b shows the transmission response of one of the output waveguides of the flat-top AWG with and without thermal tuning. The asymmetrical passband shape due to the fabrication imperfections was significantly improved by applying 0.5 W to the bottom arm of the MZI.

The cascaded AWG configuration is shown in Fig. 2.23c. This device was characterized by using the same procedure as described before. Several of the outer and central output waveguides of each secondary AWG were measured, as shown in Fig. 2.26. The overall response has an envelope function which overlaps very well with the transmission spectra of the MZI-synchronized primary AWG, as indicated by the dashed line in Fig. 2.26a. A central excess-loss value of 4.5 dB (1 dB from the primary AWG and 3.5 dB from the secondary AWG) and a non-adjacent crosstalk value of 30 dB were obtained. The close-up of the transmission measurement results of the 4^{th} secondary AWG is given in Fig. 2.26b. For the primary AWG design, the loss around the crossing points with the adjacent waveguides was reduced by designing the passband width in such a way that the adjacent channels overlap around the 3-dB down point which is the typical loss non-uniformity value of a cyclic AWG [Smi96]. However, the loss values at the

spectral crossing points of the adjacent passbands of the primary AWG increased from 3 dB to 6 dB towards longer wavelengths as seen in Fig. 2.25a. This can be compensated for in future designs by arranging the passband width of the primary AWG.The design parameters, i.e., FSR and wavelength resolution, for both primary and secondary AWGs are flexible. The idea of a broad-band, MZI-synchronized AWG is applicable for high-resolution systems as well. The secondary AWGs can be designed with higher wavelength resolution, e.g. 0.1 nm, however a compromise between device size and the resolution needs to be made.

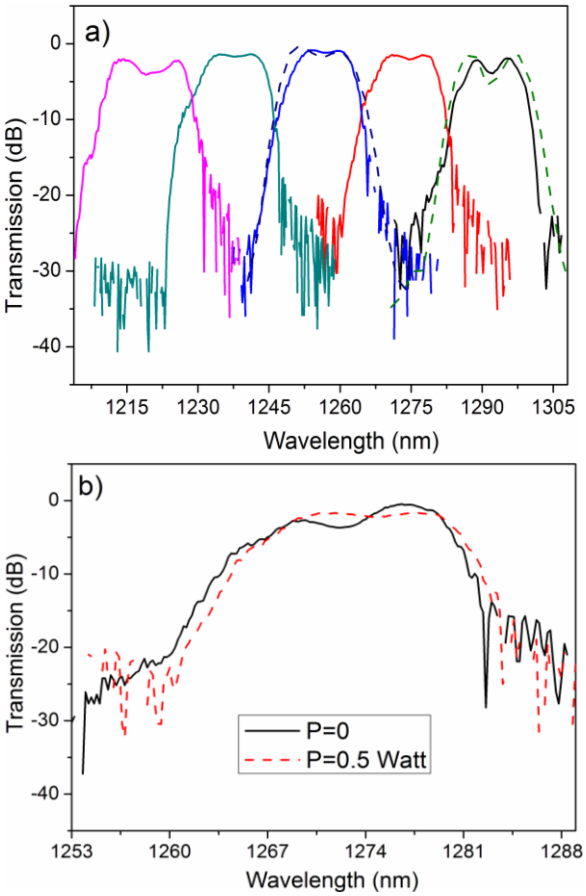

Fig. 2.25 (a) MZI-synchronized AWG spectrum, exhibiting a 0.5-dB-bandwidth of 12 nm and 1 dB excess loss at the central channel. The dashed lines are the simulated transmission spectra of the center and the 5^{th} output channels in case of the non-ideal balanced coupler given in Fig. 2.22b. **(b)** Thermal tuning effect on the transmission spectrum of one of the output channels of the MZI-synchronized AWG; black solid line: heater turned off, red dashed line: heater turned on.

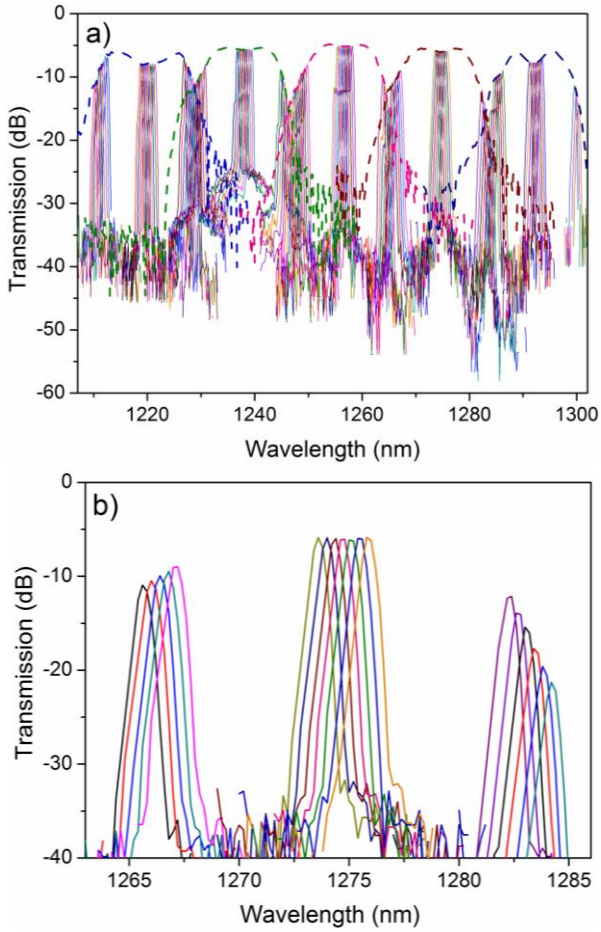

Fig. 2.26 (a) Measurement result of the cascaded AWG system with MZI-synchronized, flat-top primary AWG and five 1 × 51 secondary AWGs. The dashed line is the transmission response of the MZI-synchronized primary AWG, which acts as an envelope for the secondary AWGs. **(b)** Close-up of the 4th secondary AWG transmission results.

2.7 Discussions and conclusions

Design, simulation, and optical characterization of AWG spectrometers as well as several different approaches for realizing AWG spectrometers for on-chip OCT applications have been investigated in this chapter. Since a single AWG cannot provide high resolution and large FSR at the same time, two different cascaded AWG systems were proposed; namely conventional and cyclic FSR AWG. Although conventional method is more tolerant to fabrication imperfections compare to cyclic method, the overall device size is rather big. Cyclic method

occupies almost half of the space of that a conventionally cascaded AWG system, however it is dependent on the quality of the available fabrication technology especially for high wavelength resolutions. In conclusion for a compact size cyclic AWG is preferable whereas for a fabrication-resistant system the conventional method is preferable.

3 Integrated Michelson interferometers

3.1 Introduction

The heart of any OCT system is an interferometer which is generally in Michelson configuration. As it was discussed in Chapter 1, the beam splitter and reference arm of a Michelson interferometer (MI) can be implemented using integrated optics. For a high resolution SD-OCT system, the bandwidth of the spectrometer should be large, which necessitates a beam splitter with a constant 3-dB splitting ratio over a broad wavelength range. In integrated optics such a beam splitter can be realized using wavelength-insensitive couplers; namely balanced couplers and non-uniform adiabatic couplers. This chapter firstly introduces directional coupler theory, as the basis for the theory of balanced and non-uniform adiabatic couplers. Then design, realization, and characterization of these couplers will be discussed. Finally the dispersion of an on-chip reference arm will be investigated.

3.2 Optical 3-dB couplers

3.2.1 Directional coupler design

A directional coupler is the waveguide equivalent of the fused fiber coupler which is a lossless component as illustrated in Fig. 3.1. The directional coupler functions by evanescent wave coupling between two closely spaced waveguides which can be described by the coupled mode theory. In a symmetrical directional coupler with two identical waveguides, both even and odd modes of the system are excited in the interaction region. Due to the different propagation constants of these two modes, the power crosses from one waveguide to the other as it propagates along the device.

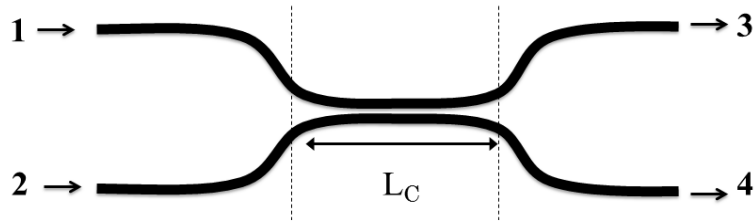

Fig. 3.1 Schematic of a 2×2 directional coupler where L_C is the coupling length.

The transmission characteristics of a 2×2 directional coupler can be expressed by the transfer matrix, in which the modal amplitudes in input waveguides transmitted to those in output waveguides. If we ignore the waveguide and bending losses the general form of the transmission matrix of a directional coupler (formed with either symmetric or asymmetric waveguides) can be written as [Hua94]

$$M = \begin{bmatrix} \cos(\phi) - j\cos(\eta)\sin(\phi) & -j\sin(\eta)\sin(\phi) \\ -j\sin(\eta)\sin(\phi) & \cos(\phi) + j\cos(\eta)\sin(\phi) \end{bmatrix}, \qquad (3.1)$$

$$\cos\eta = \frac{\delta}{\Gamma}, \quad \delta = \frac{\beta_2 - \beta_1}{2}, \quad \Gamma = \sqrt{\delta^2 + \kappa^2},$$

where $\phi = \delta \times L$ is the phase term, κ is the mutual coupling coefficient between waveguides, and δ is the half of the difference between propagation constants of the sysmten modes (β_1 and β_2), expressing the degree of synchronism between the modes. For a symmetric directional coupler formed with two identical waveguides, $\delta = 0$, Eq. (3.1) can be reduced to

$$M_S = \begin{bmatrix} t_{13} & t_{14} \\ t_{23} & t_{24} \end{bmatrix} = \begin{bmatrix} \cos(\phi) & -j\sin(\phi) \\ -j\sin(\phi) & \cos(\phi) \end{bmatrix}, \qquad (3.2)$$

For a lossless coupler the transfer matrix is unitary, i.e. $|t_{13}|^2 + |t_{14}|^2 = 1$ and $|t_{23}|^2 + |t_{24}|^2 = 1$, where $|t_{13}|$ and $|t_{24}|$ are called bar-coupling ratio (Y) whereas $|t_{14}|$ and $|t_{23}|$ are called cross-coupling ratio (X). A directional coupler is a symmetric and reciprocal device which necessitates that X is the same for 1→4, 4→1, 2→3, and 3→2 and similarly Y is the same for 1→3, 3→1, 2→4, and 4→2. For power conservation $X + Y = 1$. In an on-chip OCT system, the light reaching the detector will traverse the coupler twice for each path, once in cross and once in bar, so overall the transfer ratio of the coupler will be

$$T = XY = X(1 - X), \qquad 3.3)$$

which has a maximum 1/4 for $X = 1/2$. Even if the reflectivity of the specimen is much lower than that of the reference mirror, the optimum splitting ratio will always be 1/2 (3 dB) for the coupler used in an on-chip OCT system.

When we neglect the higher-order modes (i.e. each waveguide in isolation supports only one guided mode), and assume a weak coupling between the waveguides, the total field can be decomposed into either the mode amplitudes E_1 and E_2 of each channel waveguide in isolation (uncoupled), or the mode amplitudes E_p and E_q of the composite structure (coupled) [Gha91]. If the two coupled single-mode waveguides have identical optical properties (synchronous coupling), they

support two system modes, a symmetric (even) one, E_p, and an antisymmetric (odd) one, E_q. If the cross-section of the system is z-dependent (waveguides not parallel to each other, or tapered), the modal fields become z-dependent, and one speaks about local channel modes $E_1(z)$, $E_2(z)$ and local modes $E_p(z)$ and $E_q(z)$, see Fig. 3.2.

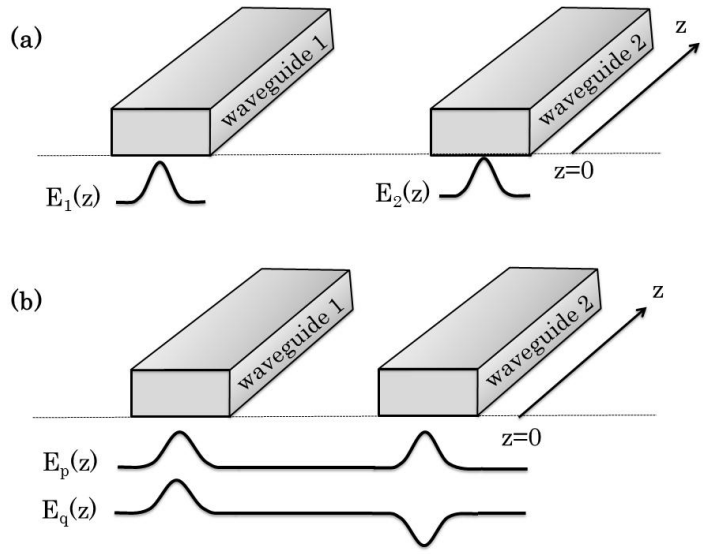

Fig. 3.2 Schematic of **(a)** uncoupled and **(b)** coupled identical waveguides with the electric fields distributions of the channel modes, E_1 & E_2 and the system modes E_p & E_q, respectively.

Applying this decomposition of the total electromagnetic field in a directional coupler into both the channel modes and the system modes, the amplitudes of the system modes at location z can be expressed in those of the channel modes at that location [Mil54, Hua94]:

$$E_p(z) = e^{-j(\beta+\kappa)z}\left[\cos(\frac{\eta}{2})E_1(z) + \sin(\frac{\eta}{2})E_2(z)\right], \tag{3.4}$$

$$E_q(z) = e^{-j(\beta+\kappa)z}\left[\cos(\frac{\eta}{2})E_2(z) - \sin(\frac{\eta}{2})E_1(z)\right], \tag{3.5}$$

where

$$\beta = \frac{\beta_2+\beta_1}{2}, \qquad E_1(z) = E_1(0)e^{j\Gamma z}, \qquad E_2(z) = E_2(0)e^{-j\Gamma z},$$

in which $E_1(0)$ and $E_2(0)$ are the normalized mode amplitudes satisfying $|E_1(0)|^2 + |E_2(0)|^2 = 1$, and $E_p(z)$ and $E_q(z)$ denote the symmetric (even) and

antisymmetric (odd) system modes, respectively. The power in the first waveguide is given as

$$\begin{aligned} P_1(z) &= \left|E_p(z)^2\right| \\ &= \left|E_1(0)\right|^2 \cos^2(\frac{\eta}{2}) + \left|E_2(0)\right|^2 \sin^2(\frac{\eta}{2}) - \sin(\eta)\,\mathrm{Re}(E_1(0)E_2{}^*(0)e^{2j\Gamma z}) \end{aligned} \quad ,(3.6)$$

whereas for the second waveguide it is calculated as

$$\begin{aligned} P_2(z) &= \left|E_a(z)^2\right| \\ &= \left|E_1(0)\right|^2 \sin^2(\frac{\eta}{2}) + \left|E_2(0)\right|^2 \cos^2(\frac{\eta}{2}) + \sin(\eta)\,\mathrm{Re}(E_1(0)E_2{}^*(0)e^{2j\Gamma z}) \end{aligned} \quad ,(3.7)$$

Since directional couplers utilize the interference of two channel modes, both these modes must be excited with an equal amplitude $E_1(0) = -E_2(0)=1/\sqrt{2}$ (assuming that the input power is 1). In addition, for a symmetric directional coupler ($\delta = 0$, hence $\eta = \pi/2$, $\Gamma = \kappa$) Eqs. (3.6) and (3.7) become

$$\begin{aligned} P_1(z) &= \left|E_1(0)\right|^2 \cos^2(\frac{\eta}{2}) + \left|E_2(0)\right|^2 \sin^2(\frac{\eta}{2}) + \frac{\sin(\eta)}{2}\cos(2\kappa z)) \\ &= \frac{1}{4} + \frac{1}{4} + (\frac{2\cos^2(\kappa z) - 1}{2}) = \cos^2(\kappa z) \end{aligned} \quad , \qquad (3.8)$$

and

$$\begin{aligned} P_2(z) &= \left|E_1(0)\right|^2 \cos^2(\frac{\eta}{2}) + \left|E_2(0)\right|^2 \sin^2(\frac{\eta}{2}) - \frac{\sin(\eta)}{2}\cos(2\kappa z)) \\ &= \frac{1}{4} + \frac{1}{4} - (\frac{1 - 2\sin^2(\kappa z)}{2}) = \sin^2(\kappa z) \end{aligned} \quad , \qquad (3.9)$$

3.2.2 Balanced coupler design and characterization

3-dB balanced couplers can be realized by cascading two conventional directional couplers in a Mach-Zehnder configuration with a relative phase shift of 2θ introduced between them [Lit97], as shown in Fig. 3.3. In this configuration, the purpose of the second coupler is to compensate for deviations introduced by the first one and the phase shift of 2θ in the Mach-Zehnder can be chosen such that the response of the device becomes flatter than a normal 3 dB directional coupler. This value is calculated to be $\theta = \pi/3$. Cherchi et al. showed geometrically, by means of Poincaré spheres, how the phase shift 2θ can effectively compensate small errors in the coupler sections [Che03]. Such couplers can be designed to yield a maximally

flat response with respect to deviations in wavelength, polarization, or uniform fabrication over a broad spectral range, with no excess loss.

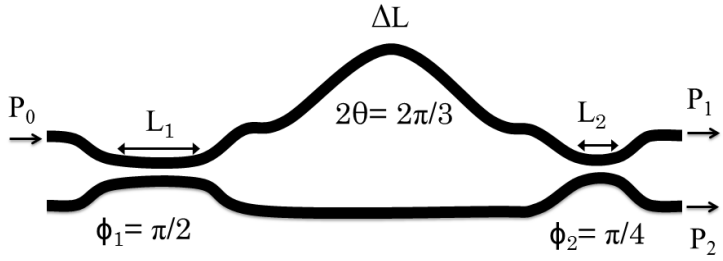

Fig. 3.3 Schematic of the 3-dB balanced coupler.

A 3-dB balanced coupler can be considered as a combination of two symmetric couplers (with different phase accumulations, ϕ_1 and ϕ_2) and a delay section in series. The matrix which is representing the wavelength response of the 3-dB balanced coupler is given as

$$M_B = M_{S1} \cdot M_D \cdot M_{S2}, \tag{3.10}$$

where M_{S1} and M_{S2} are defined using Eq. (3.2) as

$$M_{S1,2} = \begin{bmatrix} \cos(\phi_{1,2}) & -j\sin(\phi_{1,2}) \\ -j\sin(\phi_{1,2}) & \cos(\phi_{1,2}) \end{bmatrix}, \tag{3.11}$$

in which $\phi_{1,2}$ is the half phase term of the first and second symmetric directional couplers, respectively. The transfer matrix of a delay section with a phase difference of 2θ can be written as

$$M_D = \begin{bmatrix} e^{-2j\theta} & 0 \\ 0 & 1 \end{bmatrix} \text{ or (omitting a common phase) } M_D = \begin{bmatrix} e^{-j\theta} & 0 \\ 0 & e^{+j\theta} \end{bmatrix}, \tag{3.12}$$

where θ is the half propagation phase term. By inserting Eqs. (3.11) and (3.12) into Eq. (3.10) and performing the matrix multiplication, the final result becomes

$$M_B = \begin{bmatrix} \cos(\theta)\cos(A) - j\cdot\sin(\theta)\cos(B) & -j\cdot\cos(\theta)\sin(A) - \sin(\theta)\sin(B) \\ -j\cdot\cos(\theta)\sin(A) + \sin(\theta)\sin(B) & \cos(\theta)\cos(A) + j\cdot\sin(\theta)\cos(B) \end{bmatrix}, \tag{3.13}$$

where $A = \phi 1 + \phi 2$ and $B = \phi 1 - \phi 2$. From Eq. (3.13) the power cross coupling is extracted as

$$S = \cos^2(\theta)\sin^2(\phi_1 + \phi_2) + \sin^2(\theta)\sin^2(\phi_1 - \phi_2), \tag{3.14}$$

A wavelength-flattened design can be obtained by a numerical optimization of ϕ_1, ϕ_2, and θ. Since $\cos^2(\theta)+\sin^2(\theta)=1$, the cross coupling of a balanced coupler is bounded by two envelope functions, i.e. $\sin^2(\phi_1+\phi_2)$ and $\sin^2(\phi_1-\phi_2)$ where the weight of these terms depends on the value of θ. Reference [Lit97] specifies that in order to obtain a 3-dB coupler with a maximally flat wavelength response, the parameters are chosen as $\phi_1= \pi/2$ (full coupler), $\phi_2= \pi/4$ (3-dB directional coupler), and $2\theta = 2\pi/3$.

In this project two different balanced couplers, depending upon the operation wavelength range of the MI, i.e. 800 nm and 1250 nm, were designed. The design parameters are provided in Table 3.1. The balanced couplers were simulated using BPM and the results are depicted in Fig. 3.4.

The balanced couplers operating at 800 nm and 1250 nm were fabricated with the waveguide geometries given in Table 2.4 and Table 2.3 (Design#1), respectively. The fabrication steps discussed in Chapter 2, Section 1, were used for both couplers. The optical measurements were performed with the set-up shown in Fig. 2.13. The transmission response of each coupler arm was normalized to that of a straight waveguide in order to exclude fiber-to-chip coupling losses. The optical characterization results of both couplers are given in Fig. 3.5.

Table 3.1: *Design parameters of the balanced couplers at 800 nm and 1250 nm wavelength ranges.*

Parameters	800 nm	1250 nm
Center wavelength (λ_c)	800	1250
Bandwidth (nm)	100	100
L_1 (μm)	171	149
L_2 (μm)	43	34
ΔL (μm)	0.181	0.281
Overall device length (mm)	1.9	1.85

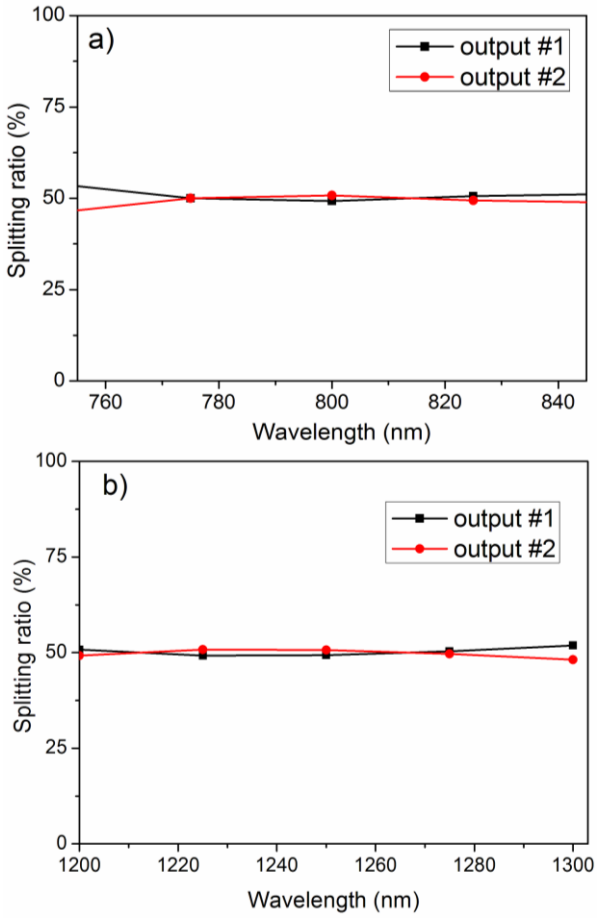

Fig. 3.4 Simulation results of the balanced couplers at **(a)** 800 nm and **(b)** 1250 nm wavelength range.

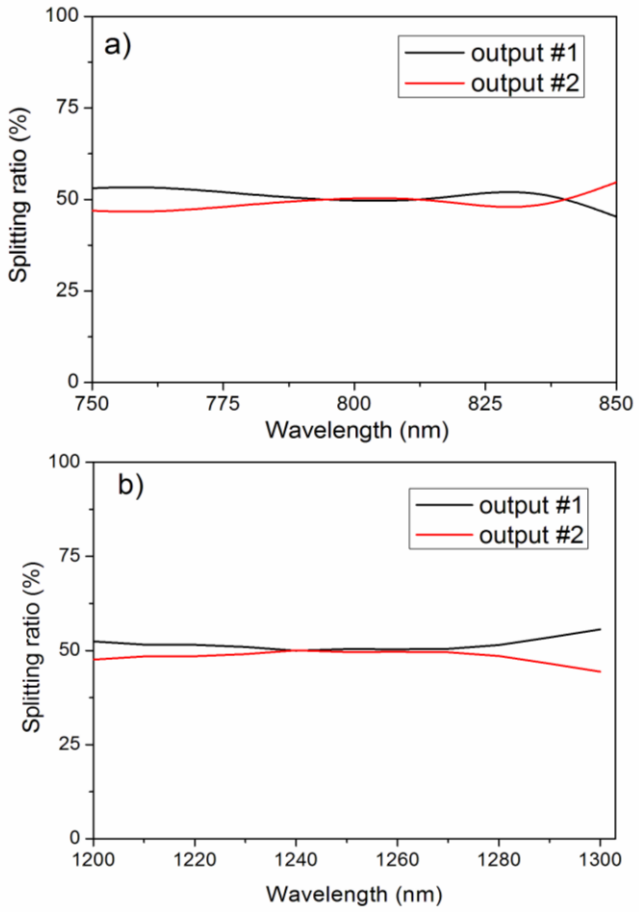

Fig. 3.5 Measurement results of the balanced couplers at **(a)** 800 nm and **(b)** 1250 nm wavelength range.

There is a slight discrepancy between simulation and measurement results of both couplers; however the splitting ratio is quite close to 50% with a very slight deviation of ±3% and ±5% for the 800 nm and 1250 nm couplers, respectively. The discrepancy could be due to process fluctuations (i.e. different core refractive index, thickness, etc.) as well as the mask discretization.

3.2.3 Non-uniform adiabatic coupler design and characterization

A non-uniform adiabatic coupler consists of two tapered waveguides (i.e. δ, η, and κ are z-dependent) as depicted in Fig. 3.6. Although both the fundamental and the first order mode of the composite structure (for simplicity modelled in 2D as a five layer slab) will be excited at the input of either of the two isolated waveguides, the

power in each of the (single-mode) input waveguides will predominantly go into only one of the system modes if the coupler is sufficiently asynchronous at its input. If the widths of the coupled waveguides change adiabatically, i.e. the cross-section of the system changes slowly with the z-position, a system mode will propagate through the structure with negligible power conversion to the other system mode.

Although, strictly speaking, pure modes do not exist in non-uniform waveguides, for adiabatically changing structures, the field distribution at each z-location is very well approximated by the modal solutions of a uniform waveguide that has the same cross-section as the adiabatic structure at that z-position. These z-dependent modal solutions are called local modes (by some authors denoted as "quasi-normal modes"). In the coupler discussed here, the synchronicity of the waveguides is arranged in such a way that only the zero-order local system mode of the coupler will be excited.

If the widths of the waveguides are interchanged at the end of the tapered coupling region this gives a full coupler, whereas equal output widths will result in a 3-dB coupler [Ada92]. The non-uniform adiabatic coupler has wavelength-flattened-performance and good process tolerances compared to other couplers, but it is rather long. Thus, adiabatic couplers have not been widely used in integrated optics.

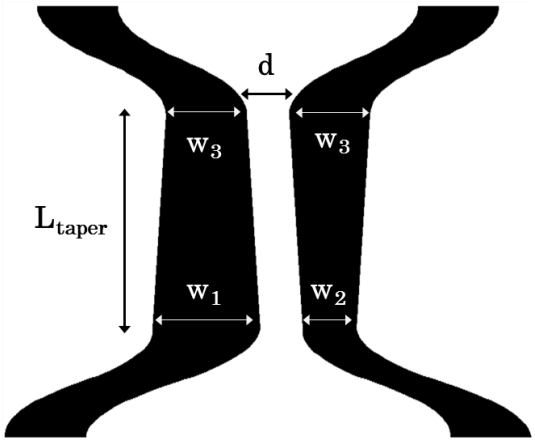

Fig. 3.6 Schematic of the 3-dB non0uniform adiabatic coupler. L_{taper} is the length of the tapered section, d is the separation between waveguides, w_1, w_2, and w_3 are waveguide widths at the beginning and the end of the straight coupling region.

In case of a non-uniform adiabatic coupler, some of the aforementioned coupler parameters will be function of z [Lou55]

$$\delta(z)=\frac{\beta_2(z)-\beta_1(z)}{2},\ \beta=\frac{\beta_1(z)+\beta_{21}(z)}{2},\ \ \eta=\eta(z),\ \ \kappa=\kappa(z),\ \ \Gamma=\Gamma(z)$$

If we assume that the waveguide cores are sufficiently well separated (i.e., weakly coupled), the system modes $E_s(z)$ and $E_a(z)$ can be written as [Lou55]

$$E_s(z)=e^{-j(\beta z+\int_0^z \kappa(\alpha)d\alpha)}(\cos(\frac{\eta(z)}{2})E_1(z)-\sin(\frac{\eta(z)}{2})E_2(z))\ , \quad (3.15)$$

$$E_a(z)=e^{-j(\beta z+\int_0^z \kappa(\alpha)d\alpha)}(\sin(\frac{\eta(z)}{2})E_1(z)+\cos(\frac{\eta(z)}{2})E_2(z)), \quad (3.16)$$

The local channel modes can be defined for both waveguides as [Lou55]

$$E_1(z)\cong e^{-j\rho(z)}\times \quad (3.17)$$

$$\left[E_1(0)+\frac{1}{2}E_2(0)\int_0^z\frac{d\eta}{dz'}e^{-2j\rho(z')}dz'-\frac{1}{4}E_1(0)\int_0^z\frac{d\eta}{dz'}e^{-2j\rho(z')}\int_0^{z'}\frac{d\eta}{dz''}e^{2j\rho(z'')}dz'dz''\right],$$

$$E_2(z)\cong e^{-j\rho(z)}\times \quad (3.18)$$

$$\left[E_2(0)-\frac{1}{2}E_1(0)\int_0^z\frac{d\eta}{dz'}e^{2j\rho(z')}dz'-\frac{1}{4}E_2(0)\int_0^z\frac{d\eta}{dz'}e^{2j\rho(z')}\int_0^{z'}\frac{d\eta}{dz''}e^{-2j\rho(z'')}dz'dz''\right],$$

where

$$\rho(z)=\int_0^z\Gamma(\varepsilon)d\varepsilon \quad (3.19)$$

The power in the first and second waveguides can be written in the same form given in Eqs. 3.6 and 3.7 by using z dependent functions as [Lou55]

$$\begin{aligned}P_1(z)&=\left|E_s(z)^2\right|\\&=\left|E_1(z)\right|^2\cos^2(\frac{\eta(z)}{2})+\left|E_2(z)\right|^2\sin^2(\frac{\eta(z)}{2})-\sin(\eta(z))\,\mathrm{Re}(E_1(z)E_2^{\ *}(z))\end{aligned}\ , \quad (3.20)$$

$$P_2(z) = \left|E_a(z)^2\right| = \left|E_1(z)\right|^2 \sin^2(\frac{\eta(z)}{2}) + \left|E_2(z)\right|^2 \cos^2(\frac{\eta(z)}{2}) + \sin(\eta(z))\,\mathrm{Re}(E_1(z)E_2^{*}(z)) \quad (3.21)$$

If only one quasi-normal mode is excited by putting power in only one waveguide (i.e. $E_1(0)=1$, and $E_2(0)=0$ and $\eta(0)=0$), $P_1(z)$ and $P_2(z)$ can be approximated as [Lou55]

$$P_1(z) \cong \cos^2(\frac{\eta(z)}{2})\left[1+v(z)\right] + \sin^2(\frac{\eta(z)}{2})\mu(z) + \sin(\eta(z))\sigma(z), \quad (3.22)$$

$$P_2(z) \cong \sin^2(\frac{\eta(z)}{2})\left[1+v(z)\right] + \cos^2(\frac{\eta(z)}{2})\mu(z) - \sin(\eta(z))\sigma(z), \quad (3.23)$$

where

$$\mu(z) \cong \left| -\frac{1}{4}\int_0^z \frac{d\eta}{dz'} e^{2j\rho(z')} dz' \right|^2, \quad (3.24)$$

$$v(z) \cong -\frac{1}{2}\mathrm{Re}\left[\int_0^z \frac{d\eta}{dz'} e^{-2j\rho(z')} \int_0^{z'} \frac{d\eta}{dz''} e^{2j\rho(z'')} dz'' dz' \right], \quad (3.25)$$

$$\sigma(z) \cong \frac{1}{2}\mathrm{Re}\left[e^{2j\rho(z)} \int_0^z \frac{d\eta}{dz'} e^{-2j\rho(z')} dz' \right] \quad (3.26)$$

For power conservation $\mu(z)+v(z) = 0$. In case of a full coupler, $\eta(L) = \pi$, the power in both arms are given as

$$P_1(z) = \left|E_2(L)\right|^2 = \mu(L), \quad (3.24)$$

$$P_2(z) = \left|E_1(L)\right|^2 = 1 + v(L), \quad (3.25)$$

Here $\mu(L)$ represents a residual power at the output end of the first waveguide; in other words mode crosstalk. For a 3-dB coupler, $\eta(L) = \pi/2$, the power in the coupler arms becomes

$$P_1(z) \cong \frac{1}{2} + \frac{\sigma(L)}{\sqrt{2}}, \quad (3.26)$$

$$P_2(z) \cong \frac{1}{2} - \frac{\sigma(L)}{\sqrt{2}}, \tag{3.27}$$

where $\sigma(L)$ is defined as the interference error power [Lou55].

In this project two different non-uniform adiabatic couplers, depending upon the operation wavelength range of the MI, i.e. 800 nm and 1250 nm, were designed with the design parameters provided in Table 3.2. The balanced couplers were simulated using BPM and the results are depicted in Fig. 3.4.

The waveguide geometries given in Table 2.4 and Table 2.3 (Design#1), were used for adiabatic couplers operating at 800 nm and 1250 nm, respectively. The fabrication steps discussed in Chapter 2, were applied for both couplers. The optical measurements were performed with the set-up shown in Fig. 2.13. The transmission response of each coupler was normalized to a straight waveguide in order to exclude fiber-to-chip coupling losses. The BPM simulations and the optical characterization results of the couplers are given in Figs. 3.5 and 3.6.

Table 3.2: *Design parameters of the adiabatic couplers at 800 nm and 1250 nm wavelength ranges.*

Parameters	800 nm	1250 nm
Center wavelength (λ_c)	800	1250
Bandwidth (nm)	100	200
$L_{straight}$ (mm)	4	3.5
w_1 (μm)	1.7	2
w_2 (μm)	1.3	1.6
w_3 (μm)	1.5	1.8
d (μm)	0.8	0.8
Overall device length (mm)	8	6.5

We obtained a coupler loss value of around 3.5 dB for both adiabatic coupler designs. Additionally an oscillatory transmission response was observed in both wavelength ranges. The discrepancy between simulation and measurement was attributed to the incomplete etching of SiON layer in the 0.8-μm-wide gap region which could perturb the evanescent tails of the waveguide mode and increases the propagation losses as well. The effect of the incomplete etching of SiON layer was included in the 1250 nm simulations and a similar oscillatory response was obtained as shown in Fig. 3.8c. Although measurement results are not fitting well with the simulations the splitting ratio is still reasonable (25% ± 5%) when we consider the operation bandwidth of the couplers.

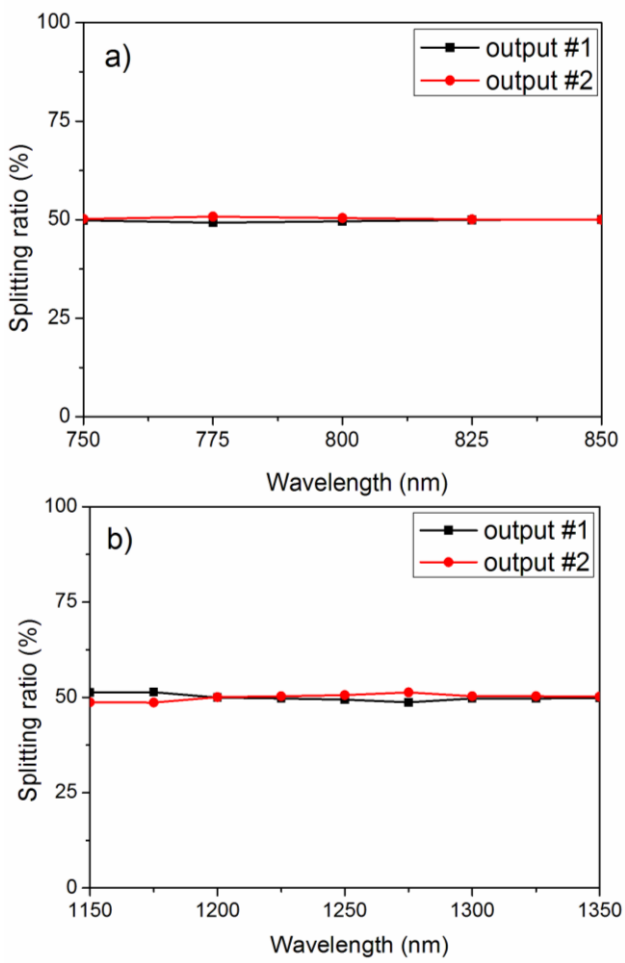

Fig. 3.7 Simulation results of the adiabatic couplers at **(a)** 800 nm and **(b)** 1250 nm wavelength range.

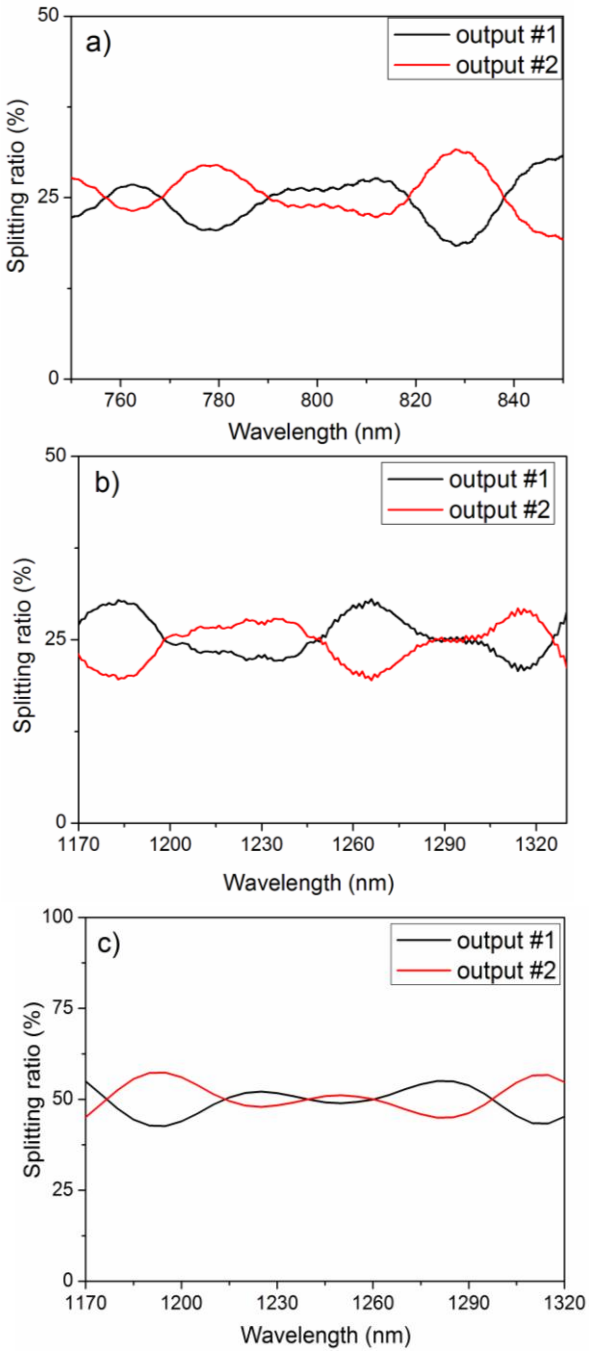

Fig. 3.8 Measurement results of adiabatic couplers at **(a)** 800 nm and **(b)** 1250 nm. **(c)** Simulation result of the adiabatic coupler at 1250 nm including the incomplete etching of SiON layer in the 0.8-μm-wide gap region.

3.3 On-chip reference arm

The group velocity of light in an optical waveguide is wavelength dependent, hence different spectral components travel at different speeds through the waveguide, resulting in broadening of a transmitted pulse at the receiver as shown in Fig. 3.9a. This is called group velocity dispersion (GVD) or chromatic dispersion. A common measure for GVD is the dispersion parameter *D* expressed in units of ps/nm/km (the amount of broadening in ps that a pulse of bandwidth 1 nm would experience over 1 km of length).

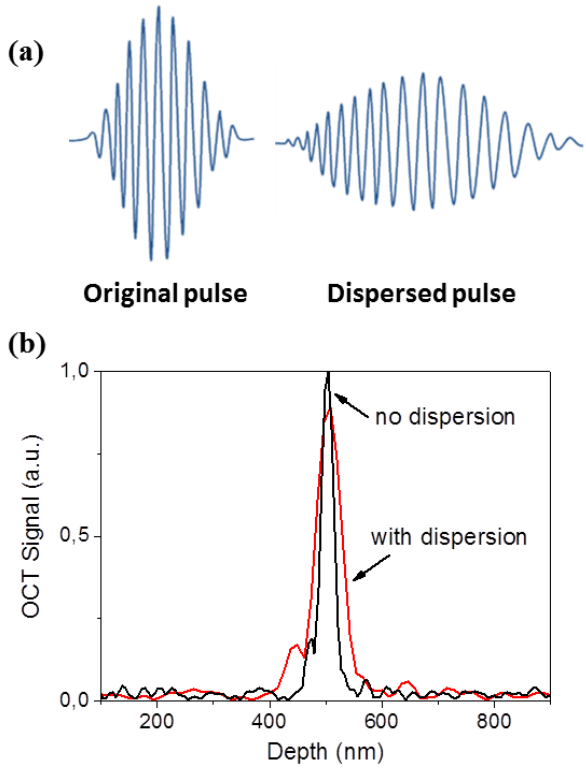

Fig. 3.9 (a) Pulse broadening due to group velocity dispersion. **(b)** Effect of dispersion on OCT signal FWHM and intensity.

In an on-chip OCT system the GVD mismatch between reference and sample arm should be compensated for an optimal axial resolution and sensitivity as illustrated in Fig. 3.9b. The intensity of the interference signal in case of an incoherent light source was derived in Eq. (1.12) with a frequency-dependent phase term ($\Delta\phi(\omega)$) resulting from dispersion between the reference and sample arms. The Fourier transformation of the interferogram in Eq. (1.12) gives rise to a broad

distribution of path lengths instead of a single sharp peak at depth *z* unless dispersion compensation between the interferometer arms is applied.

There are some post-processing methods that can be applied after OCT data is acquired [Cen04, Dre01]. For on-chip SD-OCT systems using an external mirror for the reference arm, such post-processing methods can be easily applied. For an on-chip reference arm where the dispersion mismatch is high, post-processing is still applicable, but the loss cannot be compensated. For a high signal-to-noise (SNR) system the overall loss should be minimized, therefore the GVD of the optical waveguides should be engineered at the design stage by using different cladding materials or by changing the width of the waveguides which has a much stronger effect on the GVD.

For this reason the waveguide geometry for 800 nm OCT with on-chip reference arm design was optimized to reduce the GVD. For a standard waveguide geometry with width of 1.2 µm and height of 1 µm, the dispersion was calculated as D = 200 ps/nm/km whereas for an optimized waveguide geometry with a waveguide width of 1.5 µm and height of 0.8 µm it was obtained as D = 140 ps/nm/km from the simulations. If we assume a total source bandwidth (BW) of 25 nm and an on-chip difference between reference and sample arms (ΔL) of 10 cm (20 cm for double pass), the dispersion induced offset in time (T_D) is obtained as

$$\begin{aligned} T_D &= D \times BW \times 2\Delta L \\ &= 140\,ps/nm/km \times 25nm \times 20cm\,, \\ &= 0.7\,ps \end{aligned} \tag{3.27}$$

which means that light returning from sample arm and reference arm will have 0.7 ps difference in time. If we multiply this with the speed of light (c), the dispersion induced offset in distance is obtained as

$$\begin{aligned} X_D &= T_D \times c \\ &= (7\times10^{-13}\,s) \times (3\times10^{8}\,m/s)\,, \\ &= 0.21mm \end{aligned} \tag{3.28}$$

If the coherence length defined by the spectrometer resolution is greater than 0.21 mm a good fringe visibility can be obtained. The wavelength resolution of the AWG spectrometer in this configuration is 0.1 nm which results in a coherence length of 2.8 mm according to Eq. (1.13). Since the coherence length is large enough, we do not expect any fringe loss or broadening in the axial resolution for the 800-nm waveguide design.

4 Optical coherence tomography (OCT) measurements

4.1 Optical low coherence reflectometry (OLCR) measurements

In this section we will discuss the optical low coherence reflectometry (OLCR) measurements of the AWG spectrometers as well as their combination with on-chip beam splitters at 800 nm and 1300 nm wavelength ranges. The OLCR measurements were done in order to characterize the components before applying them to OCT imaging. The measurements were performed in collaboration with the Academic Medical Center in Amsterdam[4] and Medical University of Vienna[5].

4.1.1 800-nm AWG measurements

4.1.1.1 Measurement set-up

The OLCR measurements with the 800-nm AWG spectrometer were performed by using the free-space Michelson interferometer (MI) setup. The schematic of the free-space SD-OCT system with integrated AWG spectrometer is shown in Fig. 4.1. The design and geometrical specifications of the 800-nm spectrometer are given in Table 2.6 (AWG#1) and Table 2.8.

The free-space MI is illuminated with a superluminescent diode emitting a partially polarized Gaussian-like spectrum with the specifications provided in Table 4.1. Light from the source is directed to the reference and sample arms by a 50:50 beam splitter. For testing purposed the sample has been replaced by a movable mirror. The reference mirror is kept stationary, while the sample mirror is moved during the experiments. Light returning from the two arms is focused by an objective lens into a single-mode fiber and directed to the AWG spectrometer. The output power of the MI is measured to be 0.1 mW. In the AWG spectrometer, the optical spectrum is dispersed by the arrayed waveguides and imaged by a camera

[4] The OCT measurements were performed with V. Duc Nguyen and Jeroen Kalkman under the supervision of Ton van Leeuwen.

[5] The OCT measurements were performed with the help of Aneesh Alex and Boris Považay under the supervision of Wolfgang Drexler.

lens (JML Optical, focal length: 50 mm) with high numerical aperture (NA = 0.5) onto the camera with the specifications provided in Table 4.1.

The linescan camera is operated at a readout rate (pixels/second) for which the maximum optical power is close to the saturation limit of the camera, see Table 4.1. The raw unprocessed interference data is stored in memory at 25 frames per second. The frame rate of a camera is the fastest rate at which an image or spectra can continuously recorded and saved. Frame rates are governed principally by the number of pixels and the pixel readout rate. The signal processing steps as described in Chapter 1 (Fig. 1.4) were applied. The measured spectra have an absolute wavelength scale defined by the center wavelength and FSR value of the AWG. The corresponding depth axis is calculated using Eq. (1.14).

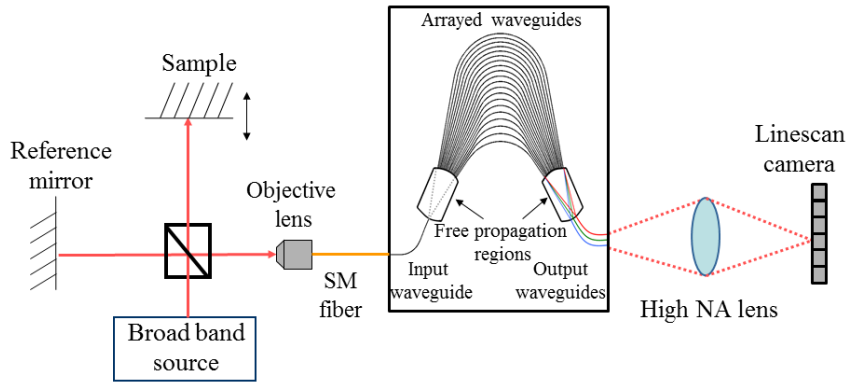

Fig. 4.1 Optical measurement set-up of the SD-OLCR system with free-space Michelson interferometer and integrated AWG spectrometer.

Table 4.1: *Specifications of the light source and the linescan camera for 800 nm and 1300 nm measurements.*

Parameters		**800 nm**	**1300 nm**
Light source	Center wavelength (λ_c)	830 nm	1300 nm
	Bandwidth (FWHM)	13 nm	40 nm
	Output power	5 mW	7 mW
	Polarization	Unpolarized	TE
	Spectral shape	Gaussian	Gaussian
Linescan camera	Number of pixels	2048	1024
	Pitch of pixels	14 µm	25 µm
	Readout rate	36 kHz	46 kHz

4.1.1.2 Measurement results

The spectrum shown in Fig. 4.2 is the spectrum from the reference arm at 800 nm. The optical bandwidth $\Delta\lambda_{FWHM}$ of the spectrum is measured as 12 nm which corresponds to an axial resolution of Δz = 24 µm, in agreement with the targeted axial resolution for 800 nm for the given light source bandwidth. The inset shows the measured interference spectrum after background subtraction, measured at a depth of 200 µm, i.e. with a 200-µm length difference between the sample arm and the reference arm. The modulation on the spectra due to interference can be clearly observed.

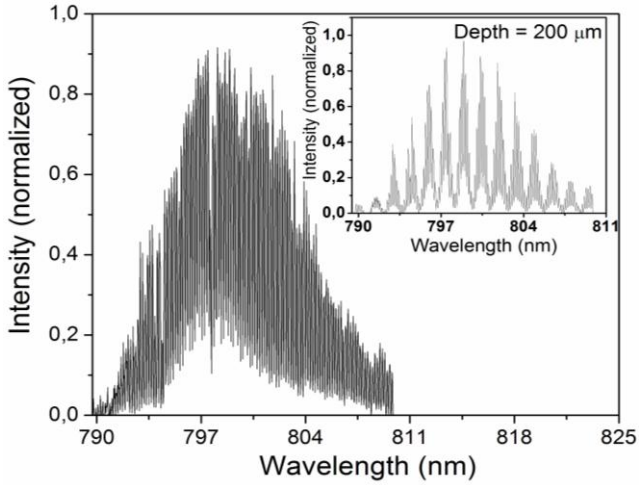

Fig. 4.2 Measured reference spectrum of the 800-nm AWG spectrometer on the linescan camera. The inset shows interference spectrum measured at 200 µm depth after background subtraction.

The OLCR signals measured for different depths, i.e. for different path length differences between sample and reference arm of the MI, are shown in Fig. 4.3. The depth scale corresponded one-to-one with the physical distance of the sample arm position change. We achieved a maximum depth range of 1 mm. The FWHM values of the point spread functions at various depths are plotted in Fig. 4.4. An experimental axial resolution of 25 µm at 100 µm depth was obtained. A decrease in resolution was found at larger depths, which was attributed to limited spectral sampling resolution of the SD-OLCR system to resolve high-frequency spectral interference modulations from deeper areas. Imaging aberrations due to the high-NA lens, noise, and reduced interpolation accuracy of the resampling process at higher fringe modulations are possible causes of the measured loss of spectral resolution.

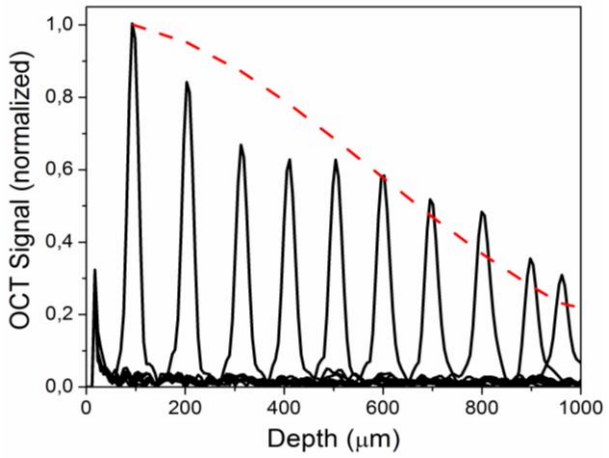

Fig. 4.3 Measured OLCR signal as a function of depth for a mirror reflector and fit of the roll-off (dashed line). The maximum depth range is 1 mm.

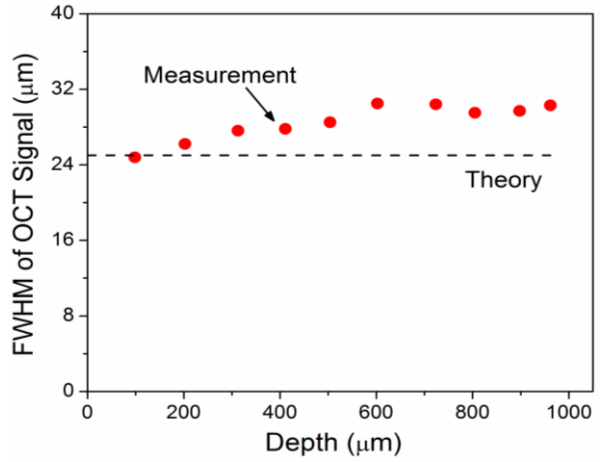

Fig. 4.4 Measured OCT axial resolution (solid circles) in comparison with the theoretical axial resolution (dashed line). A decrease in resolution occurs for larger depths.

Equation (2.7) was fitted to the signal decay data presented in Fig. 4.3, with ω as a free parameter and $K = 0.5$. The value for ω obtained from the fit is 0.9, which is higher than the expected lower limit of $\omega = 0.32$ which is calculated with the simulated FWHM spectral resolution of the spectrometer. The discrepancy between theory and experiment could arise due to misalignment in the experimental set-up as well as lens aberrations which cause spectral broadening of the spot size on the linescan camera pixel (in addition to imaging errors in the focal plane of the second

FPR). In addition, the AWG spectrometer was not designed to be polarization insensitive; hence, partial polarization of the light source could cause degradation in roll-off in depth.

4.1.2 1300-nm AWG measurements

4.1.2.1 Measurement set-up

The OLCR measurements with the 1300-nm AWG spectrometer were performed by using the fiber-based MI setup. The design and geometrical specifications of the 1300-nm spectrometer are given in Table 2.7 (AWG#1) and 2.8.

A schematic of the fiber-based SD-OLCR system is shown in Fig. 4.5. Light from a broadband source (B&W Tek superluminescent diode) is coupled, via an optical circulator (Gould Fiber Optics), to prevent unwanted feedback into the laser, into a 90/10 beam splitter with polarization controllers positioned in both sample and reference arm. The back reflected light is redirected through the optical circulator and coupled into the input waveguide of the AWG spectrometer. The beams from the output waveguides of the AWG spectrometer are focused, by a high-numerical-aperture camera lens (JML Optical, focal length: 50 mm, NA = 0.5), onto a 46 kHz linescan camera. A moveable mirror is placed in the sample arm to measure the OCT signals in depth. This set-up was used only for the OLCR measurements with the 1300-nm AWG because no suitable beam splitter was available for this wavelength range. The camera and light source specifications are listed in Table 4.1.

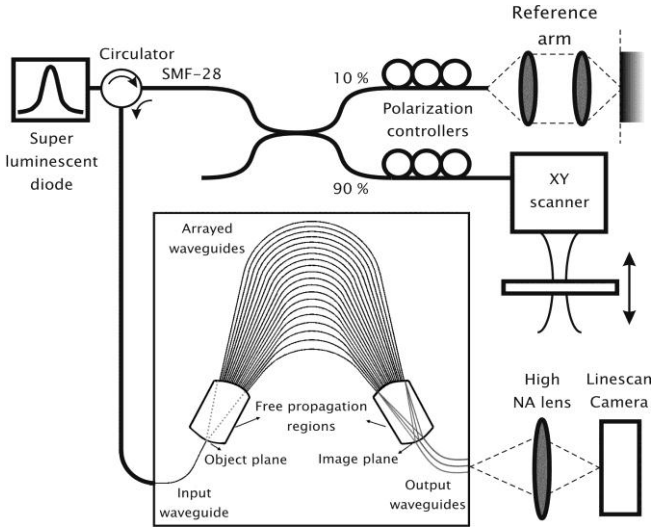

Fig. 4.5 Schematic of the experimental setup used for 1300-nm fiber-based SD-OCT with an AWG.

4.1.2.2 Measurement results

Figure 4.6 shows the spectrum from the reference arm at 1300 nm. The optical bandwidth $\Delta\lambda_{FWHM}$ of the spectrum is measured as 39 nm which corresponds to an axial resolution of Δz = 19 µm. The inset shows the interference spectrum measured at 200 µm depth after reference subtraction. The wavelength scale is based on the AWG design parameters (λ_c and $\delta\lambda$), which determines the maximum imaging depth according to Eq. 1.14.

Figure 4.7 demonstrates OCT imaging up to the designed maximum depth range of 1 mm. The physical movement of the sample-arm mirror corresponds one-to-one with the calculated depth scale. A fit of the OCT roll-off in depth (dashed line), including the effect of the waveguide width, provides the ratio of the spectral resolution to the wavelength spacing ($\delta\lambda$), ω = 1.4, which is higher to the expected limit of the AWG performance, ω = 0.55, calculated from the ratio of measured spectral resolution to the wavelength spacing.

The theoretical axial resolution in air, calculated based on the reference spectrum, is 18.5 µm. Figure 4.8 shows that the measured axial resolution is in reasonable agreement with the theoretical axial resolution of 18.5 µm. A slight decrease in depth resolution at larger depths and higher fitted ω value is attributed to lens aberration in the imaging system.

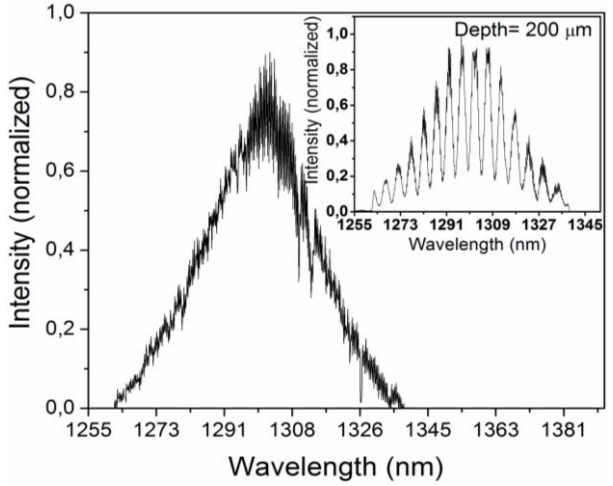

Fig. 4.6 Measured reference spectrum of the 1300-nm AWG spectrometer on the linescan camera. The inset shows interference spectrum measured at 200 µm depth after background subtraction.

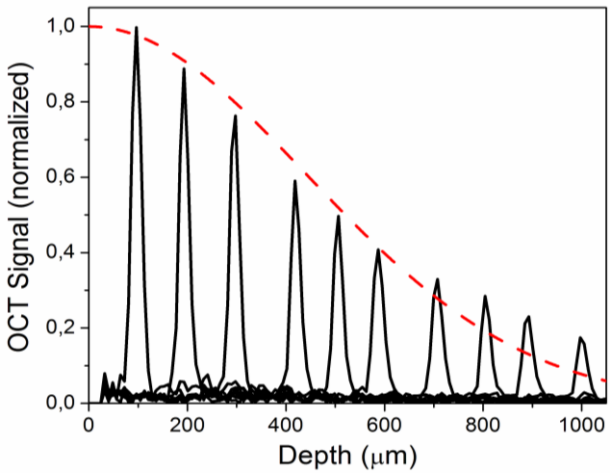

Fig. 4.7 Measured OCT signal as a function of depth for a mirror reflector and fit of the roll-off (dashed line). The maximum depth range is 1 mm.

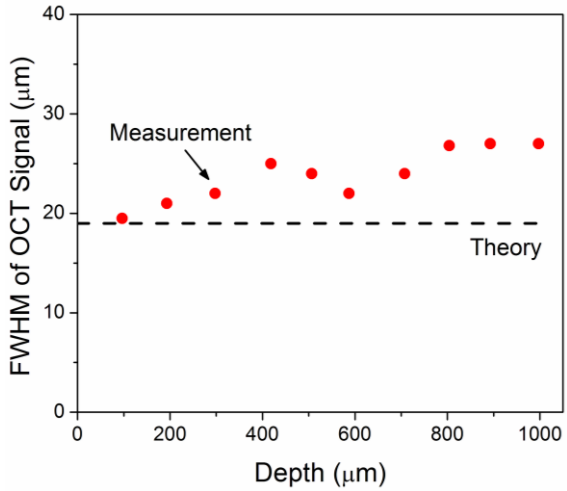

Fig. 4.8 Measured axial resolution (FWHM) versus depth in comparison with the theoretical axial resolution (dashed line).

Imaging of the spectrometer output plane onto the linescan-camera pixel array was not straightforward, since the output waveguides have a very high exit NA and the AWG output channels are separated by 60 μm, resulting in a large collection area of a centimeter wide. Therefore, a wide-field, high-NA camera lens is required to image the output-waveguide array at the edge of the chip onto the flat linescan-camera imaging plane. Given the large field of view of the output-waveguide array

and the high exit NA, we expect non-ideal imaging performance over parts of the spectrum.

4.1.3 Integrated 1250-nm AWG with beam splitter measurements

In this section the OLCR measurements of the partially-integrated SD-OCT system using an AWG spectrometer and an integrated beam splitter (BS) which forms the on-chip MI at 1250 nm wavelength range will be investigated. The design specifications of the AWG (AWG #6 in Table 2.7 and Table 2.9) and the non-uniform adiabatic coupler are discussed in Chapters 2 and 3, respectively.

4.1.3.1 Measurement set-up

The schematic of the SD-OCT system with integrated AWG spectrometer and BS is shown in Fig. 4.9. Partially polarized light emitting from a broadband superluminescent diode (Previum/Thorlabs Inc., Newton, USA) was coupled into the BS by using a butt-coupled fiber and directed to the reference and sample arms by the 3 dB non-uniform adiabatic coupler. The light source operated at a center wavelength of 1320 nm and had a full-width at half-maximum bandwidth of 100 nm and a fiber-coupled optical power of 5.5 mW. TE polarized light was coupled into the chip and the polarization of light was optimized, by a polarization controller, to maximize the interference signal at the detector. Light exiting the reference and sample arms was collimated by ×40 objective lenses with numerical apertures (NA) of 0.65 and directed towards reference mirror and sample. The SNR, axial resolution, and imaging range were measured using a mirror in the sample arm. For depth ranging measurements the reference mirror was kept stationary, while the sample mirror was moved during the experiments. Light returning from the two arms was focused by the respective objective lenses into the waveguides and passed through the BS to the AWG spectrometer. The output power of the MI for both reference and sample arms were measured to be 0.5 mW. In the AWG spectrometer, the optical spectrum was dispersed by the arrayed waveguides and imaged by a ×20 objective lens (NA=0.40) onto the entire, 2.5 mm wide array of the infrared linescan camera (SUI1024-LDH-1.7RT-0500/LC, 1024 pixels, 25×500 µm pixel size, Goodrich) with a magnification factor of ~10:1. The axial scan (depth or A-scan) rate of the OCT system was 47 kHz, corresponding to a frame rate of 46 Hz with 1024 A-scans (each 1024 pixels) per frame.

A Labview programming interface (National Instruments) was employed for detection, control and real time display. The non-linear relation between the spectral positions of the detection channels and optical frequency was corrected by a *k*-mapping procedure based on optimizing the signals from a reference reflection

[Hof09]. After resampling to *k*-space, the dispersion between the two arms of the interferometer was eliminated by applying the compensating phase term to the interference spectrum in order to maximize the axial resolution. Finally the reflectivity depth profile was obtained by transforming the corrected interference spectrum to the spatial domain via an inverse Fourier transform.

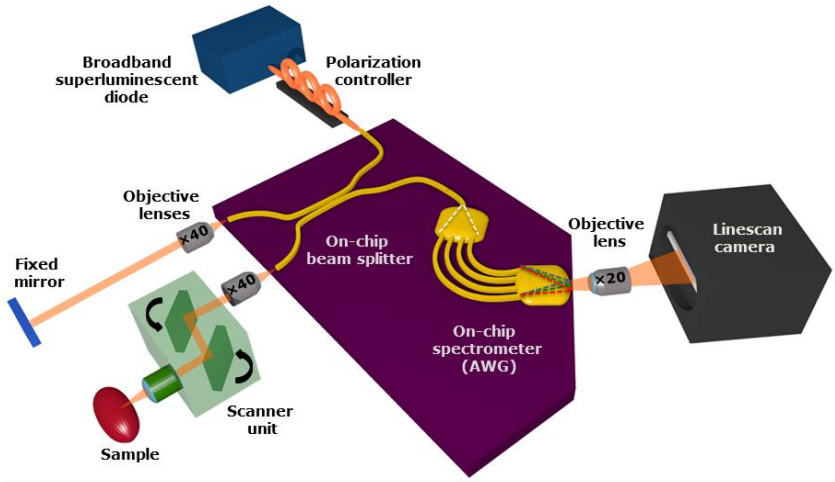

Fig. 4.9 Schematic of the on-chip SD-OCT system with an external mirror in the reference arm. The output channels of the AWG have been removed in order to have a continuous spectrum. A 3-dB non-uniform adiabatic coupler is used to split the incoming light equally towards sample and reference arms. The light reflected off the sample and the reference arms merge in the coupler and enter the input waveguide of the arrayed waveguide grating (AWG). The dispersed light is imaged onto the entire linescan camera using a ×20 objective lens. Note that the purple region is artificially magnified for viewing purposes.

4.1.3.2 Measurement results

For enhancing the maximum depth range, the output channels of the AWG were omitted in the design stage. The linescan camera detected a 75 nm bandwidth centered at ~1300 nm, where each pixel was wavelength-separated by 0.13 nm. The AW-limited resolution $\Delta\lambda = \lambda_c/Mm$ [Tka90] was calculated as 0.28 nm. The overall spectral resolution, which is given by the combination of these two resolutions, was calculated as 0.21 nm [Hu07]. Theoretically, this resolution results in an improved depth range of 2 mm. A detailed analysis will be given in Chapter 5.

Figure 4.10 demonstrates OCT imaging up to the designed maximum depth range of 2 mm.The theoretical axial resolution in air, calculated based on the reference spectrum (BW=100nm), is 7.5 µm. However, the waveguides at the

air/SiON interface of the BS were tapered from 1.8 µm to 3 µm in order to increase the back-coupled light efficiency, which resulted in an unexpected destructive wavelength dependent interference in the spectrum. The usable spectrum reduced from 100 nm to 75 nm which corresponds to a theoretical axial resolution of 10.5 µm. Signal-to-noise ratio (SNR) measured close by the zero delay where both interferometer arms are equal in length was 74 dB at 0.5 mW optical power on the sample, which includes 5 dB fiber-to-chip coupling loss, 7 dB on-chip coupler double-pass excess loss due to imperfect fabrication, and 7.5 dB double-pass transmission loss of the standard microscope objectives. In the current arrangement the signal attenuation at 1.4 mm depth range was 15 dB, which was caused by the aberrations of the spectrometer objective on top of the physical resolution limit given by the finite sampling resolution of the camera and the AWG.

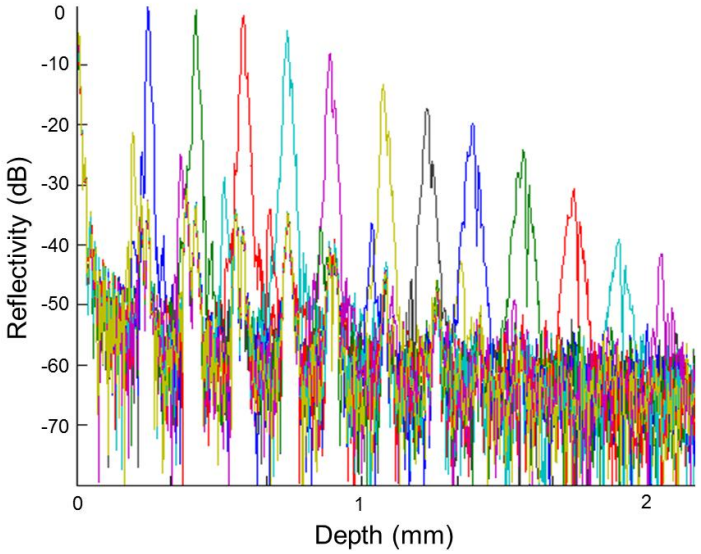

Fig. 4.10 Measured reflectivity signal as a function of depth for a mirror reflector. The maximum depth range is 2 mm.

4.2 OCT imaging

In this section the OCT imaging performance of the 1300-nm AWG with an external MI and the 1250-nm AWG connected to the on-chip BS will be presented. A phantom image was obtained by using the 1300-nm AWG whereas with the 1250-nm partially-integrated SD-OCT system human skin was imaged.

4.2.1 1300-nm AWG with an external MI

As a demonstration of OCT cross-sectional imaging using the 1300-nm AWG spectrometer, the same fiber-based SD-OCT system shown in Fig. 4.5 was used. An image of a layered phantom is obtained by scanning the OCT beam over the sample, see Fig. 4.11. The phantom consists of three layers of scattering medium (scattering coefficient μ_s=4 mm^{-1}, n=1.41) interleaved with non-scattering tape. As expected, all three scattering layers are observed up to the maximum single pass length of 1 mm (725 μm depth for the average refractive index of 1.38 of the phantom). The current imaging resolution and depth are sufficient for biological imaging but can be improved by increasing the FSR and the number of output channels.

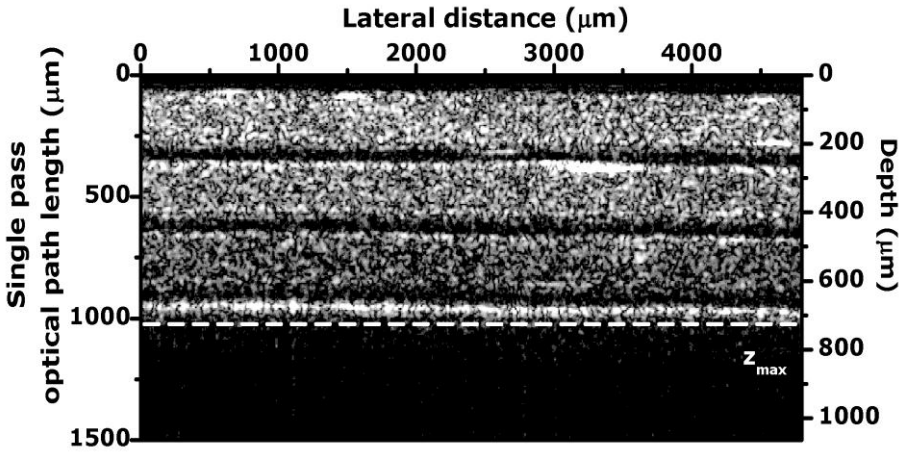

Fig. 4.11 An OCT image of the three-layered scattering phantom measured with the 1300-nm AWG as spectrometer in fiber-based SD-OCT. The dashed-line indicates maximum imaging depth.

4.2.2 1250-nm AWG connected to the on-chip beam splitter

4.2.2.1 Measurement set-up

The schematic of the SD-OCT setup with AWG spectrometer and integrated BS shown in Fig. 4.9 was also used in these measurements.

For *in vivo* imaging the reference arm consisted of a free-space pathway, while the sample arm consisted of a handheld probe with a close pair of galvanometric mirrors for scanning in two dimensions and a telecentric scan lens (LSM03-BB, Thorlabs) that was covered by a closed patient interface for direct contact via a 10° tilted 4 mm thick sapphire window to avoid specular reflections from the air/tissue interface. The lateral resolution of the system was limited by the numerical aperture

of the scan lens and the incident beam size to 20 µm. The mirrors were controlled by a field programmable gate array that was triggered by the camera output. Digital data were transferred from the linescan camera to a frame grabber (NI-1429, National Instruments) by a high-speed CameraLink connection.

4.2.2.2 Measurement results

In vivo imaging of was performed using human skin above the proximal interphalangeal joint of the middle finger by applying contact gel to the imaging sites as an index matching medium to decrease the surface reflectivity. Conventional OCT requires transverse scanning of the illumination spot in one (X) or two directions (X, Y) to produce cross-sectional (XZ) or *en face* (XY) images, respectively.

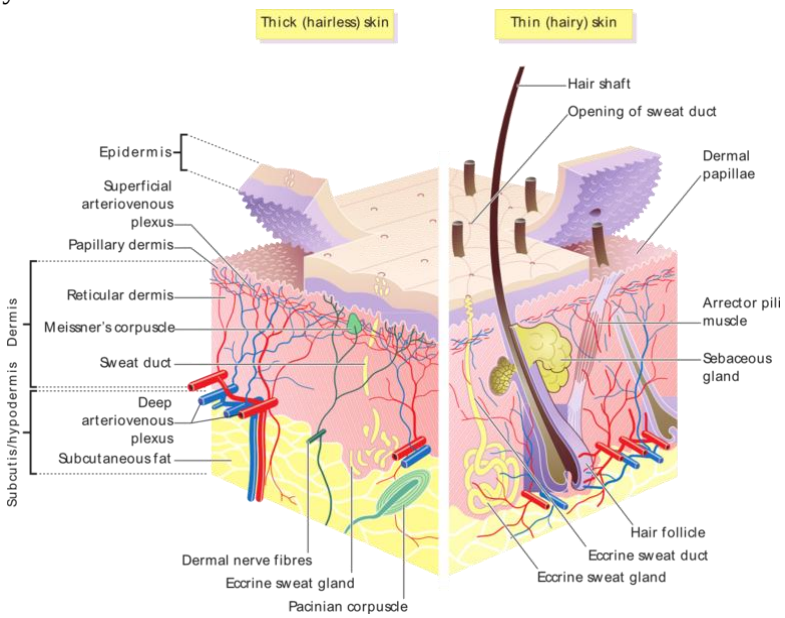

Fig. 4.12 Human skin anatomy. (www.healthhype.com)

The *en face* and the corresponding averaged cross-sectional tomogram of the proximal interphalangeal joint of the middle finger are given in Fig. 4.13. The morphology of several layers (see Fig. 4.12) including the stratum corneum and vivid layers of the epidermis, the stratum papillare and reticulare of the dermis, featuring vessels and several skin appendages like hair shafts, and sweat ducts within a depth range of 1.4 mm has been visualized with an axial resolution of 7.5 µm. In pigmented thin skin (Fig. 4.14) additionally to the bright appearance above the skin, hairs are identified as dark almost vertical channels, bulging with an onion-like appearance towards their root in the deeper regions of the dermis. The

layered structure of the pigmented thin skin is well visualized throughout the cross-sectional series and a 3D volume rendered representation is depicted in Fig. 4.14e.

Besides normal skin imaging, abnormal sites like scar tissue was examined with the on-chip SD-OCT system. Fig. 4.15 shows the *en face* and the corresponding cross-sectional tomogram taken from the scar tissue at the index finger of the volunteer . Cross-section displaying the irregularities caused due to an incision after complete healing is given in Fig. 4.15(a). In the *en face* view of the region at the layer of the stratum corneum the typical matrix-like distribution of sweat ducts (bright spots) appears on the left and right portion of Fig. 4.15(b). The tissue distortions become obvious at the layer of the living epidermis and the dermal papillae as shown in Fig. 4.15(c). The fine dark lines on the right parallel to the scar correspond to deep folds in the epidermis that also cast shadows onto the deeper dermis (Fig. 4.15(d)).

The imaging performance of the partially-integrated SD-OCT system was compared to the 1300-nm fiber-based custom-designed SD-OCT system [Ale10] by acquiring OCT images of scar tissue from approximately the same locations with both systems as depicted in Fig. 4.16. The axial resolution of the custom-designed SD-OCT system was obtained as ~5.7 µm in tissue which is slightly better than the partially-integrated SD-OCT system. However, SNR of the partially-integrated SD-OCT system (74 dB) lags behind the custom-made SD-OCT system (94 dB) due to the background caused by internal reflections and the aforementioned high losses. The theoretical SNR of both devices is given by 107 dB using the shared camera with >70% quantum efficiency and 13.9 µs exposure time at 0.5 mW optical power incident on the sample. The zero delay of the partially-integrated SD-OCT system was offset by ~800 µm towards the region of interest (see Fig. 4.16c) to compensate for ~10 dB loss caused by signal roll-off, due to the averaging the remaining SNR difference mainly affects the weaker signals. The ~ 10 dB difference can also be compensated by using a lower number of averages (8 versus 32, Fig. 4.16b) which results in a signal of similar dynamics. Although it suffers less from the blur introduced by averaging and operates at slightly higher axial resolution, it misses the faint features below the dermis (dark region at bottom of Fig. 4.16a and 4.16b). Fortunately, the current implementation has the potential to be improved by optimization of individual components and can be exploited further to increase the SNR of the on-chip OCT system to the level of commercial bulk-optics systems.

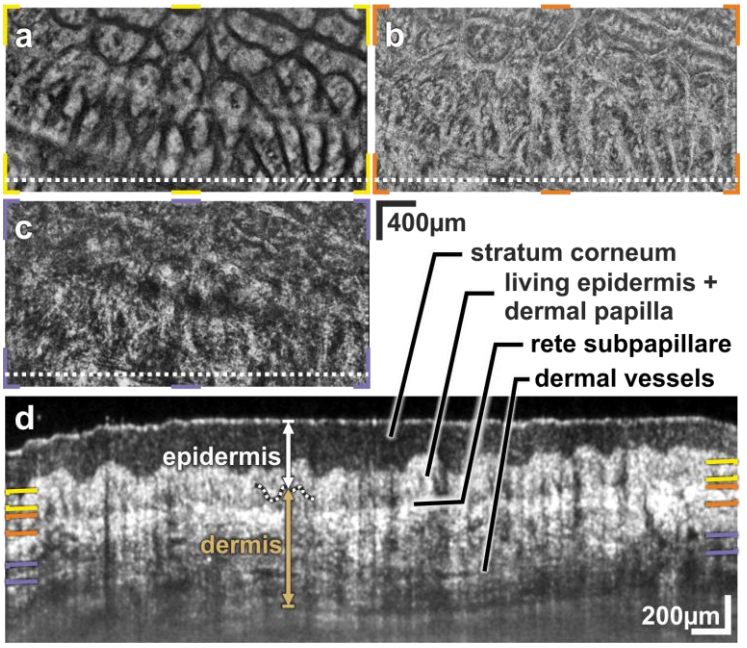

Fig. 4.13 Images of glabrous skin at interdigital joint taken using the 1300-nm partially-integrated SD-OCT system: (a, yellow) *En face* section at the deeper epidermal layers featuring the living epidermis on top of the dermal papillae. Central sweat ducts are visible as dark dots (b, orange) section at the rete subpapillare where fibrous components dominate the basis of the dermal papillae. (c, violet) shows the deeper dermis with vessels. (d) Cross-section as indicated by the dotted white line in the *en face* sections. Colored indicators depict the location of the *en face* views. The scale bars denote 200 µm in cross sections and 400 µm in *en face* sections.

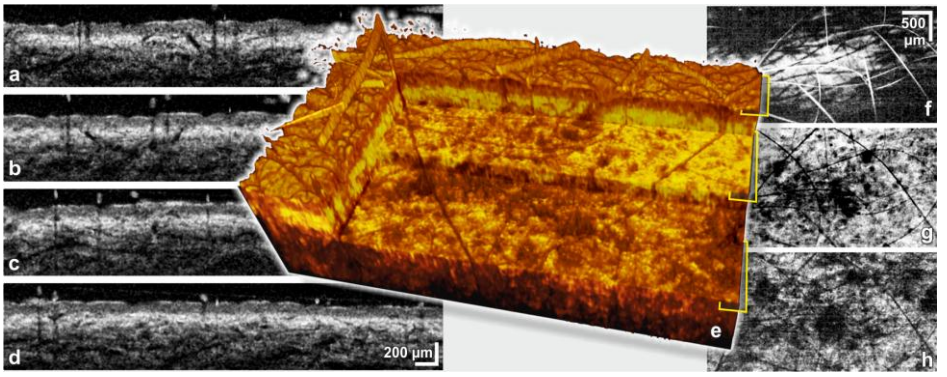

Fig. 4.14 Images of pigmented thin skin taken using the 1300-nm partially-integrated SD-OCT system. Left (a-d): Cross-sectional views of three-dimensional volume obtained at a location with increased melanin

concentration. Right (f-h): *En face* views at different depths. e) 3D volume rendered representation of OCT image data. The yellow markers delineate the corresponding positions of the orthogonal views. The scale bars denote 200 µm in cross sections and 500 µm in *en face* sections.

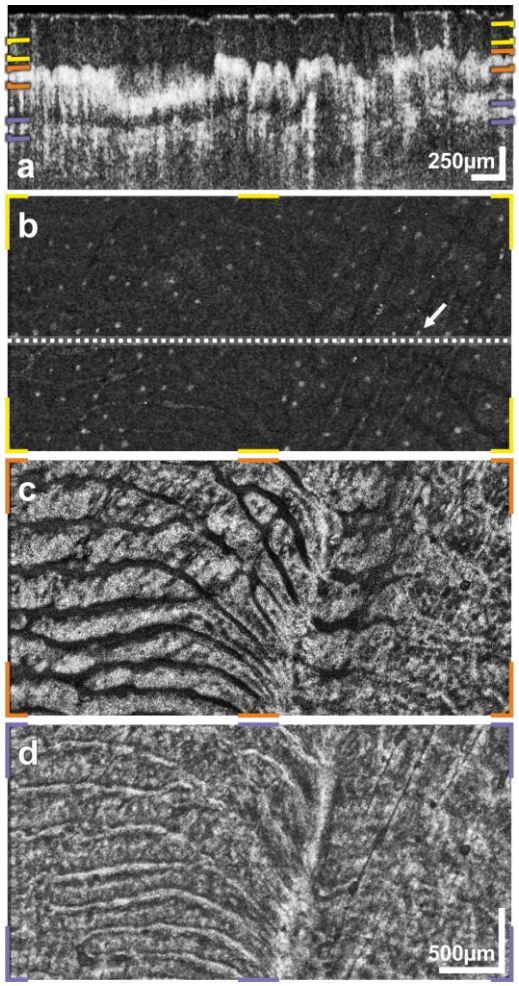

Fig. 4.15 Images of scar tissue at index finger taken with the 1300-nm partially-integrated SD-OCT system: (a) Cross section displaying the irregularities caused due to an incision after complete healing. (b, yellow) In the *en face* view of the region at the layer of the stratum corneum the typical matrix-like distribution of sweat ducts (bright spots) appears on the left and right portion of the image. (c, orange) The tissue distortions become obvious at the layer of the living epidermis and the dermal papillae. (d, violet) Inside the dermis the denser fibrous material of the scar has replaced the normal tissue including the vascular support. The scale bars denote 250 µm in cross sections and 500 µm in *en face* sections.

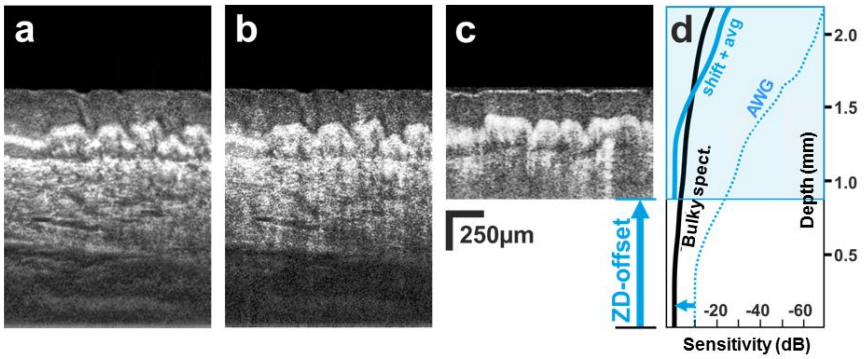

Fig. 4.16 Cross-sectional tomograms of the scar tissue at the index finger taken by (a),(b) the 1300-nm custom-designed SD-OCT system and (c) the partially-integrated SD-OCT system. (a) and (c) are taken with 32× average, and (b) is taken with 8× average. The zero delay is offset by ~800 μm towards the region of interest to compensate for ~10 dB loss caused by signal roll-off; (c) is the resulting OCT image. (d) The signal roll-off curves of the partially-integrated OCT system using an AWG spectrometer and the custom-designed OCT system using a bulky spectrometer with the blue dashed line and black solid line, respectively. The resulting signal roll-off of the partially-integrated OCT system after compensation is given by the blue solid line in (d).

4.2.2.3 Discussion

The results described above demonstrate that a partially-integrated SD-OCT system comprising an AWG spectrometer and an integrated BS is capable of acquiring *in vivo* OCT images of human skin with a reasonable axial resolution and depth range. The current SNR of 74 dB, which is sufficient for biomedical imaging, is limited by the overall system losses (i.e. non-adiabatic coupler loss, fiber-to-chip coupling loss, objective lens losses, and AWG excess loss) as well as the increased background due to internal scatterings. However it can be further increased up to 95 dB by reducing the (1) non-adiabatic coupler loss down to its theoretical value of 0 dB with an optimized lithography and etching procedure, (2) fiber-to-chip coupling losses down to <0.5 dB either with a spot-size converter [Spu98] or a tapered input waveguide [Mit94], (3) losses arises from using microscope objectives down to <1 dB with proper objective lenses designed specifically for the near infrared range, and (4) AWG excess loss down to <0.5 dB by applying vertical tapers at the interfaces of arrayed waveguides with the FPRs [Sug00]. The significant significant background in the measurements was attributed to the internal scatterings due to waveguide surface roughness as well as the back

reflections at the waveguide facets at air/SiON interfaces. In order to reduce the back reflections arise from the air/SiON interfaces and also increase the facet quality of the chip, the waveguide facets were polished at an angle of 8^{o}. Although back reflections reduced significantly by angle polishing the facets, it couldn't be eliminated completely. The exact location of the unwanted reflections can be determined using the low coherence reflectometry method, and the reflections arise from waveguide surface roughness can be eliminated by optimizing the etching procedure and using a higher quality e-beam mask for smoother waveguide surfaces.

The operation window of the AWG and the non-uniform adiabatic coupler were centered at 1250 nm which did not match with the center wavelength of the available light source, i.e. 1320 nm which deviated the splitting ratio of the coupler by 5% and slightly improved the depth range by ~50 μm due to the longer wavelength of the light despite the reduced AW-limited resolution of 0.29 nm. The 100-nm-wide bandwidth of the light source resulted in a theoretical axial resolution of 5 μm in tissue; however the aforementioned destructive interference due to the tapers at the waveguide ends of the non-uniform adiabatic coupler reduced the useful spectral bandwidth from 100 nm to 75 nm that is the main cause of the decrease in axial resolution to 7.5 μm in tissue. The tapers will be removed in the future designs. Additionally, the theoretical axial resolution will be improved by cascading several AWGs for increasing the bandwidth.

Since most skin malignancies are of epidermal origin, 1.4 mm of depth range is sufficient for visualizing the superficial skin layers and for performing early diagnostic procedures [http://www.cancer.umn.edu/cancerinfo]. Frequency domain OCT signals suffer from a depth-dependent signal roll-off that is attributed to the effective spectral resolution of the device. In the current arrangement the signal attenuation at 1.4 mm depth range was 15 dB, which was caused by the aberrations of the spectrometer objective on top of the physical resolution limit given by the finite sampling resolution of the camera and the AWG.

4.3 Conclusions

The applicability of AWG spectrometers for SD-OCT systems were demonstrated with an imaging depth of 1 mm and axial resolutions of 25 μm and 20 μm (at 100 μm depth) at 800 nm and 1300 nm, respectively. The measurement results were in good agreement with the theoretical calculations. Furthermore, a phantom image was taken by using a fiber-based SD-OCT set-up with the 1300-nm AWG spectrometer.

Additionally *in vivo* imaging by the partially-integrated SD-OCT system comprising of 1250-nm AWG and the integrated beam splitter has been successfully demonstrated in human skin. In-tissue axial resolution of 7.5 µm and in-tissue depth range of 1.4 mm was achieved. The performance of the current partially-integrated OCT system can be improved to the level of bulky commercial OCT systems with an optimized design and high-quality fabrication facilities. Considering the ability of lithography to easily multiply and mass-produce a perfectly optimized optical system as well as the current performance and stability of the preliminary partially-integrated SD-OCT system, these devices have a high potential to make up the central components of state-of-the-art OCT systems featuring much lower cost, size, and higher stability to make them accessible to a significantly larger group of applications and users.

5 Performance improvement of the OCT systems

5.1 Introduction

As it was demonstrated in the previous chapter, AWG spectrometers with their high spectral resolution and compactness are excellent candidates for on-chip SD-OLCR and SD-OCT systems. However, specific design-related issues limit the performance of these integrated systems. For obtaining a large depth range, the AWG spectrometer must have a high wavelength resolution, while a high axial resolution requires a wide FSR. As usually the output spectrum of an AWG is discretized in a number of output channels, the combination of large depth range and high axial resolution requires a large number of output channels, up to a point where space limitations inhibit further improvement. One possible solution is omitting the output channels (or removing them from a conventional AWG by dicing [Cve09]). In this way, the wavelength discretization will be determined by the number of pixels on the camera, which can be much larger than the number of output channels, thus enhancing the depth range significantly. Current commercial SD-OCT systems typically achieve an imaging range of ~2.0-2.6 mm [www.thorlabs.com, www.meditec.zeiss.com]. Comparable performance of an integrated instrument necessitates an improvement in the imaging range of SD-OCT using an AWG.

Another important issue is the polarization dependency of AWG spectrometers, which affects the sensitivity roll-off. Using a less polarization-dependent dispersive element, e.g. a holographic transmission grating [www.thorlabs.com], in an OLCR system is more favorable. An AWG spectrometer is polarization independent if its array waveguides are polarization independent, which can be achieved by balancing the material and waveguide birefringence [Wör07]. Although this approach requires a highly fabrication-tolerant design, it makes AWGs advantageous over bulky spectrometers. In addition, the cost and size of integrated OLCR and OCT systems will reduce significantly by using polarization-independent AWGs, thus eliminating the components for polarization control.

In this section, we discuss the impact of discrete output channels and polarization dependency of an AWG on SD-OLCR performance. We demonstrate a significant improvement in depth range when omitting the output channels from the AWG. The modulation effect of polarization on sensitivity roll-off in depth is

experimentally verified and, as a permanent solution to polarization-related signal fading problems, a polarization-independent AWG is demonstrated.

5.2 Depth range enhancement

A schematic of the SD-OLCR system with an AWG spectrometer is shown in Fig. 5.1. The free-space Michelson interferometer is illuminated with a broadband light source (Fianium, SC-450-PP) which is band-pass filtered (Thorlabs, FB800-10, bandwidth = 9.4 nm) in order to prevent overlap of different spectral orders of the AWG. Light from the source is directed to the reference and sample arms by a 50:50 beam splitter. The light returning from the two arms is combined and focused by an objective lens into a fiber coupler with a 10/90 splitting ratio. A Ti:Sapphire laser (Spectra-Physics, 3900S) is connected to the other input port of the coupler to be used in the polarization measurements. 90% of the light returning from the two arms is coupled into the AWG by a free-space coupling arrangement, which consists of two objective lenses and a polarizer. The same AWG as investigated in Chapter 4, with a center wavelength of 800 nm, a FSR of 19.4 nm, and a wavelength resolution $\delta\lambda$ of 0.16 nm, is used in this work. The device is composed of single-mode SiON channel waveguides with the design parameters listed in Table 2.4. The light dispersed in the arrayed waveguides (AW) is imaged by a camera lens (numerical aperture NA = 0.5, for the AWG with output channels) or a microscope objective lens (NA = 0.12, for the AWG without output channels) onto the charge-coupled device (CCD, Andor Technology, DV887ECS-BV). The CCD has 512 detector pixels with a 16 μm pitch.

For post processing of the acquired data, a Labview program was developed by an intern student[6]. The program controls the camera and acquires the interference spectrum continuously in real time. The FT of the spectrum is taking with a help of a Matlab code embedded into the Labview program.

[6] Lantian Chang

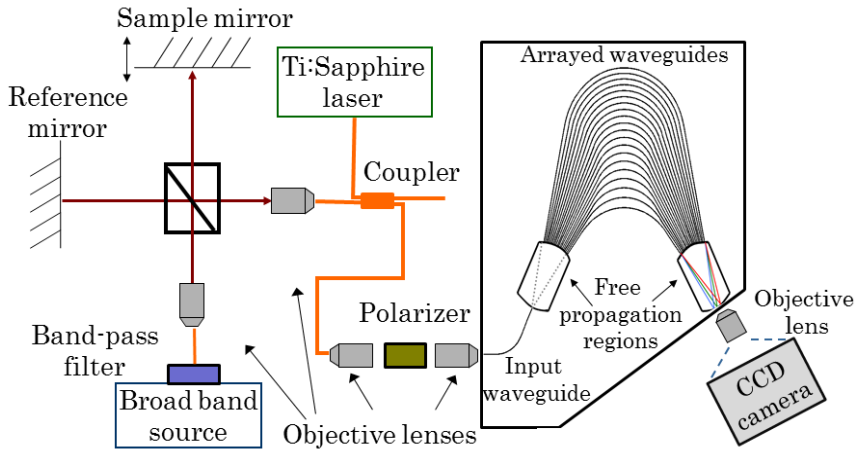

Fig. 5.1 Schematic of the experimental set-up of SD-OLCR with an AWG.

For the AWG with output channels, the wavelength resolution $\delta\lambda = 0.16$ nm leads to a theoretical maximum depth range in air of 1 mm. Figure 5.3a shows the depth ranging measurements of the AWG with output channels and a fit of the roll-off in depth (dashed line) for TE polarization. The designed depth range of 1 mm was achieved experimentally. The measured axial resolution was 31 µm, which is in good agreement with the theoretical limit of 30 µm (at 100 µm depth), as determined by the band-pass filter at the light source.

For enhancing the maximum depth range, the output channels of the AWG were removed by dicing the chip near the output facet of the second free propagation region (FPR). In order to image the light onto many pixels, the magnification of the objective lens was arranged to be ×10 and, thereby, 450 CCD pixels were addressed, which increased the number of sampling points from 125 (number of output waveguides) to 450. The CCD detected a 19.4 nm bandwidth centered at 800 nm, where each pixel was wavelength-separated by 0.043 nm.

The overall spectral resolution of this configuration (imaging the diced output plane of an AWG onto a CCD) can be defined by the combination of AW-limited resolution and the CCD pixel size if the diffraction caused by the imaging lens is neglected. The convolution of these two factors yields the overall spectral resolution of the imaging system. The AW-limited resolution of an AWG can be explained by using Fig. 5.2 which illustrates an optical imaging system comprised of two lenses with a focal length R, and a screen with an opening of width Md. It can be considered as a continuous equivalent of an AWG, with M the number of arrayed waveguides and d the spacing between them, except for removing all the sampling effects due to the discrete nature of the arrayed waveguides. According to

Fourier analysis the illumination at the output plane will be an image of the mode field profile of the input waveguide convolved with the sinc-type diffraction pattern of the screen opening.

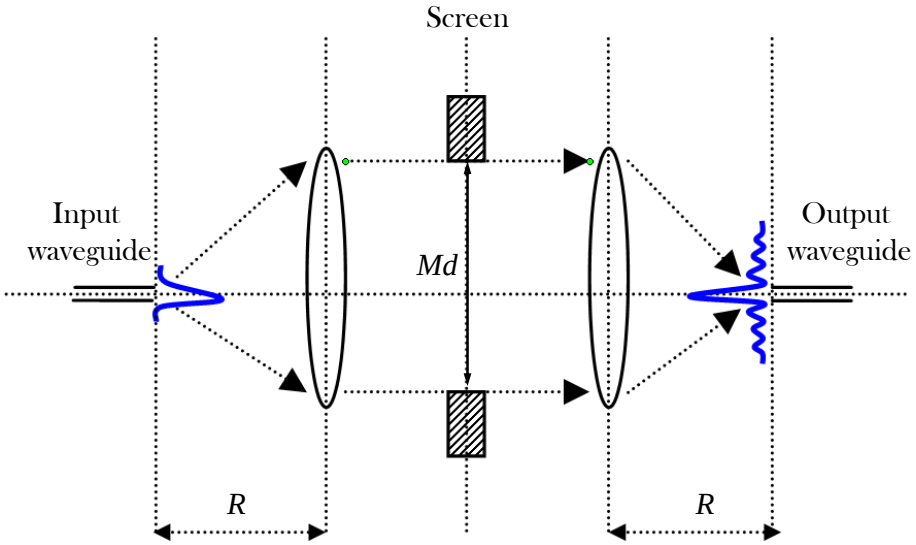

Fig. 5.2 Continuous equivalent of an AWG spectrometer, with two lenses with a focal length *R*, and a screen with an opening of width *Md*.

The minimum angular FWHM of the output mode profile is determined by the Rayleigh criterion which is given as

$$\Delta\theta_{\min} = \frac{\lambda}{Mdn_s}, \tag{5.1}$$

where n_s is the effective refractive index of the slab (lens) region. The angular dispersion of an AWG is given as

$$\frac{\partial\theta}{\partial\lambda} = \frac{m}{dn_s}, \tag{5.2}$$

where m is the grating order. From Eq. (5.2), $\Delta\theta$ can be extracted as

$$\Delta\theta = \Delta\lambda \frac{m}{dn_s}, \tag{5.3}$$

The relation between wavelength resolution and number of AWs can be obtained by setting Eq. (5.1) equal to Eq. (5.3), which yields [Tka90]

$$\Delta\lambda_{AW} = \frac{\lambda}{Mm}, \tag{5.4}$$

From Eq. (5.4) the AW-limited resolution was calculated as 0.04 nm for N = 500 and m = 40. The overall spectral resolution i.e., the convolution of the diffraction pattern of the AW for a single frequency and the finite size of the CCD pixel, was calculated as 0.0465 nm [Hu07]. Theoretically, this resolution results in an improved depth range of 3.45 mm.

Experimentally, the maximum depth range was enhanced from 1 mm to 3.3 mm, as shown in Fig. 5.3b and Fig. 5.3c, for TE and TM polarizations, respectively. The dashed lines in Fig. 5.3b and Fig. 5.3c are the fit of the OCT roll-off in depth. The least squares fitting procedure was applied to the signal roll-off function given in Eq. 2.7 with ω as the fitting parameter. The insets of Fig. 5.3b and Fig. 5.3c show the single-wavelength response of the AWG for TE and TM polarization, respectively, acquired by coupling the Ti:Sapphire laser into the AWG.

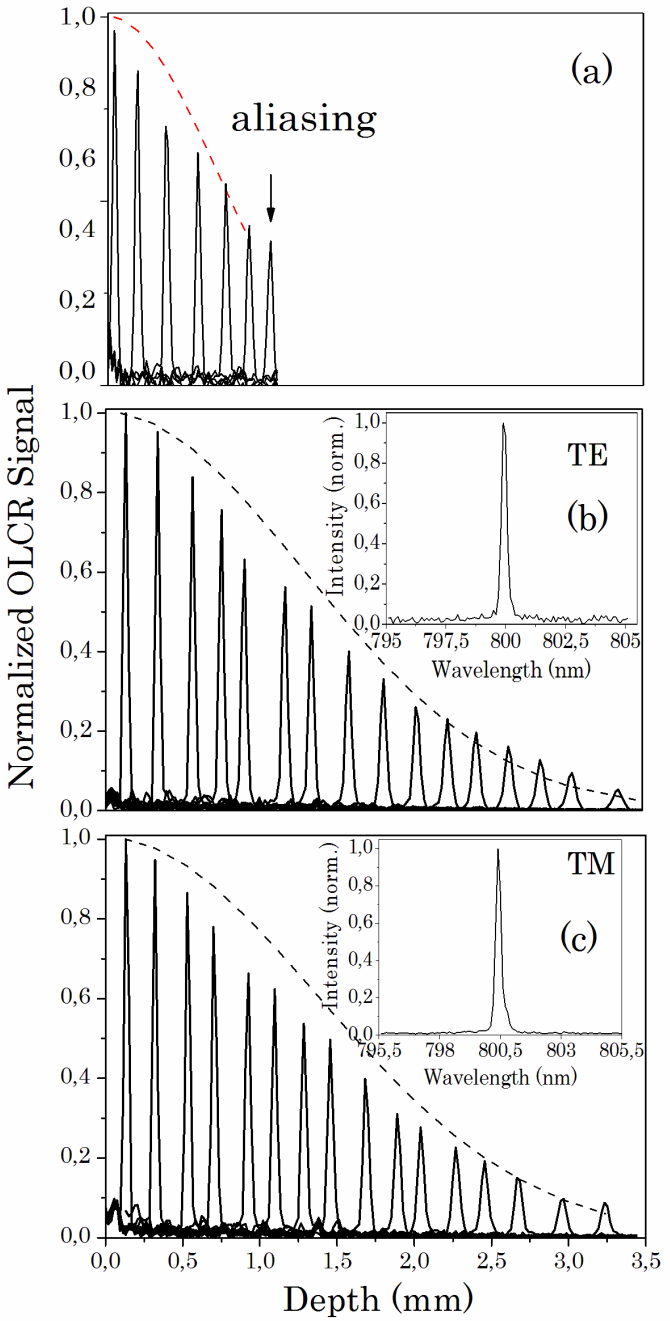

Fig. 5.3 Measured OLCR signal versus depth and fit of the roll-off (dashed line) for the AWG **(a)** with and **(b)**, **(c)** without output channels, for TE and TM polarization, respectively. The single-wavelength response of the AWG is shown in the inset of **(b)** for TE polarization and **(c)** for TM polarization.

5.3 Effect of AWG polarization dependency on OCT performance

The effect of partial light polarization on sensitivity roll-off was investigated for a TE/TM power ratio of 1. The single-wavelength response of the AWG for partial polarization is given in the inset of Fig. 5.4. The AWG was not designed to be polarization independent; consequently, a spectral shift of 0.5 nm was measured between TE and TM polarizations (see Chapter 2). A polarization-dependent AWG images a spectral peak at a given wavelength onto different positions for TE and TM polarizations as we discussed in Chapter 2. For mixed TE and TM polarization, the roll-off in depth modulates with the cosine term given in Eq. (2.15) which causes signal fading at specific depths. In Fig. 5.4, the red dashed line is the calculated value of signal intensity ($D(z)$ in Eq. (2.15)) for partial polarization. The OLCR peaks follow the beat pattern of $D(z)$ as predicted.

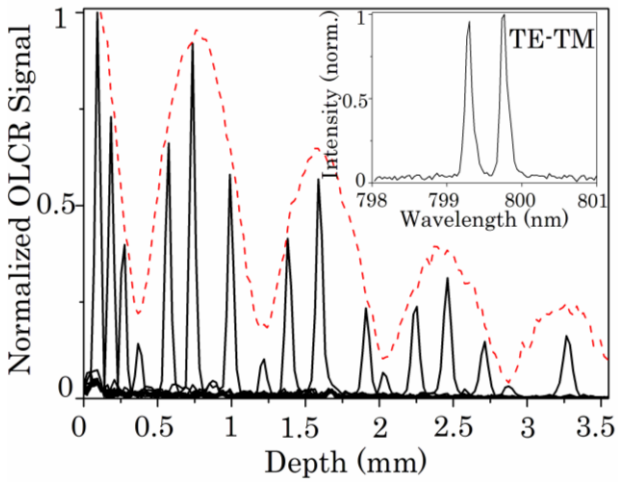

Fig. 5.4 Measured OLCR signal versus depth and calculated roll-off (dashed line) of the AWG without output channels for unpolarized light (TE/TM = 1). The inset is the single-wavelength response of the AWG for TE/TM = 1.

The polarization dependency of AWGs can be eliminated by proper waveguide design. As a proof of concept, a non-birefringent AWG centered at 1300 nm was designed with $\delta\lambda$ = 0.4 nm (results in z_{max} = 1 mm) and FSR = 20 nm. A material birefringence of 1.5×10^{-3} and fabrication tolerance of ±1% for width and height and $\pm 10^{-3}$ for core refractive index was used in the waveguide design. SiON channel waveguides with a width of 2.2 µm, height of 1 µm, and core refractive index of 1.52 were fabricated (Table 2.3, Design #2). The theoretical polarization-dependent shift was calculated as 5×10^{-6} nm and no significant shift was observed in the

transmission measurements for the center and outer channels, in Fig. 5.5. The output channels were removed by dicing and the OLCR measurements for partial polarization (TE/TM = 1) were performed using the set-up shown in Fig. 5.1 with an infrared camera (Sensor Unlimited, SU320M-1.7RT, 320 × 240 pixels, 40 µm pitch) and an infrared band-pass filter (Thorlabs, FB1300-12, bandwidth = 12 nm). An improved depth range of 4.6 mm was obtained by removing the output channels and imaging the output spectrum onto 300 horizontal pixels. No beat effect was observed, as shown in Fig. 5.6.

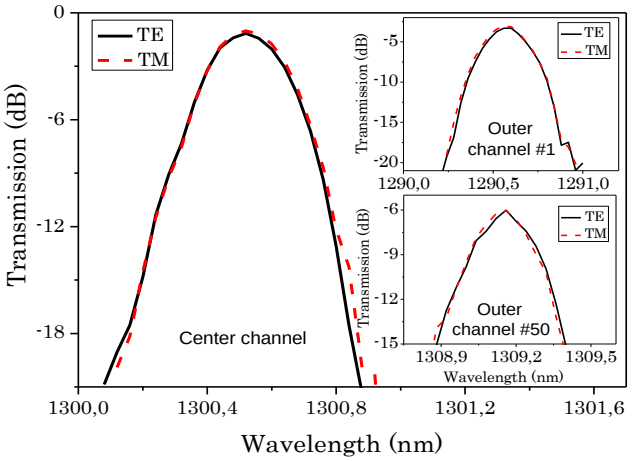

Fig. 5.5 Measurement results of the non-birefringent AWG for TE and TM polarizations. The insets show the transmission results of the outer channels. No significant polarization dependent shift is observed.

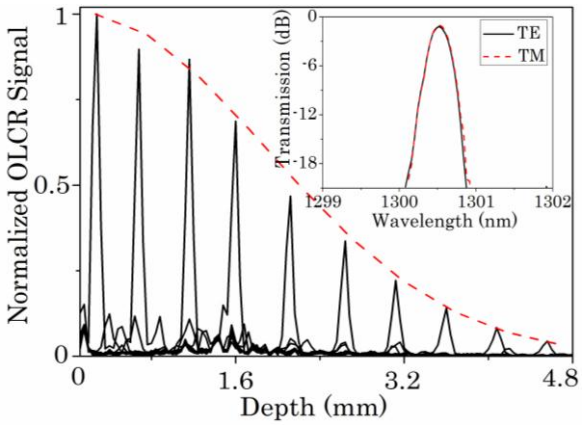

Fig. 5.6 Measured OLCR signal versus depth and calculated roll-off (dashed line) of the polarization-independent AWG without output channels for unpolarized light (TE/TM = 1). The inset is the transmission measurement result of the central channel for TE and TM polarizations.

5.4 Flat-focal-field AWG

Integrated spectrometers applied in sensing, imaging, and telecommunication are usually of the Rowland mounting type in which the input and output waveguides are located on the arc of the so-called Rowland circle [Row83]. The Rowland-circle construction for AWGs is depicted in Fig. 5.7. This arrangement has the advantage of reduced aberrations compare to other mount configurations [Pal05] and is useful whenever output channels guide the wavelengths diffracted by the spectrometer to their desired destinations, because the output channels can be arranged on the same curved image plane. Such a curved image plane, however, is not well suited for applications in which the output spectrum shall be continuously imaged directly onto a linear detector array. As discussed in Section 5.2, this provides improved spectral resolution compared to double sampling firstly by output channels and subsequently by the detector array [Cve09, Akc12]. Opposed to a curved image plane which would result in additional losses and aberrations at the outer detector channels, in this case a flat image plane would be desirable.

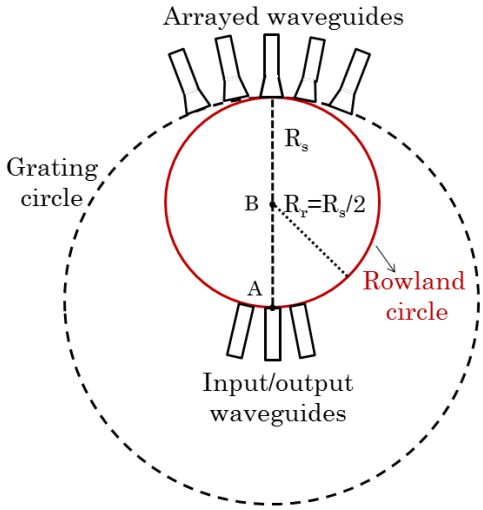

Fig. 5.7 Rowland circle construction for AWGs. A and B is the center of the grating and Rowland circles, respectively. R_s and R_r is the radius of curvature of the grating circle and the Rowland circle, respectively.

A spectrometer with a straight imaging plane is called a flat-focal-field spectrometer. Such spectrometers solve the aforementioned problems associated with Rowland mounting type spectrometers. The three-stigmatic-point method for the design of a flat-focal-field grating spectrometer was proposed by Velzel [Vel76]. Lu et al. designed and fabricated a polymer-based flat-focal-field AWG

spectrometer by using the three-stigmatic-point method; however the feasibility of the idea has been demonstrated with limited success as the fabricated AWG exhibited high crosstalk and insertion loss [Lu05]. In this section, an alternative way of designing a flat-focal-field AWG using an integrated field-flattening lens located in the second star coupler will be presented.

5.4.1 Integrated field-flattening lens design

In an ideal optical system (one without any aberrations), a planar object will be imaged onto a curved surface instead of a plane in the paraxial region. This aberration is known as Petzval field curvature [Kin78]. A field-flattening lens is a thin plano-concave negative lens which is placed close to the image plane of an optical system to flatten the curvature of its image surface by minimizing the Petzval aberration [Kin78]. In an AWG, the field curvature induced by the second star coupler (considered as a positive convex lens) can be compensated by placing a field-flattening lens in the second star coupler just before the output waveguides. By being close to the image plane it minimally affects the other aberrations.

In order to image each point on the curved surface onto a flat image plane, the focus should be shifted as a function of the lateral position y of the image point as shown in Fig. 5.8b. This condition necessitates a (field-flattening) lens thickness which is a function of the lateral position y of the image point as well. The design parameters of the lens can be derived by considering a parallel plate in a converging beam as shown in Fig. 5.8a. For rays propagating at small angles with respect to the optical axis, the plate thickness t needed for a focus shift of Δx is, independent of the angle, determined by the refractive indices n_2 and n_1 of the plate and the surrounding medium, respectively, as

$$t = \left(\frac{n_2}{n_2 - n_1}\right)\Delta x, \tag{5.5}$$

In case of a curved image surface the thickness of the plate (or field-flattening lens) becomes a function of y,

$$t(y) = \left(\frac{n_2}{n_2 - n_1}\right)d_a(y), \tag{5.6}$$

where $d_a(y)$ is the focus shift from a plane field, which can be calculated in the paraxial approximation as

$$d_a(y) \cong \Delta x(y) \cong \frac{y^2}{2R_r}, \tag{5.7}$$

where $\Delta x(y)$ is the the horizontal deviation from the flat image plane and R_r is the radius of the Rowland circle ($R_r = R_s/2$, with R_s the radius of curvature of the grating circle, see Fig. 5.9a). The radius of curvature of the imaging system (i.e. the Petzval curvature) is equal to R_r. Substituting (5.7) into (5.6) yields

$$t(y) = \frac{1}{2}\frac{y^2}{\left[\frac{(n_2 - n_1)}{n_2} R_r\right]}, \tag{5.8}$$

Equation (5.8) has the same form as (5.7), which allows us, assuming a plano-concave lens shape, to identify the denominator of (5.8) as the radius of curvature R_f of the field-flattening lens

$$R_f = \left(\frac{n_2 - n_1}{n_2}\right) R_r, \tag{5.9}$$

where n_2 and n_1 correspond to the effective refractive indices of the lens and the slab region.

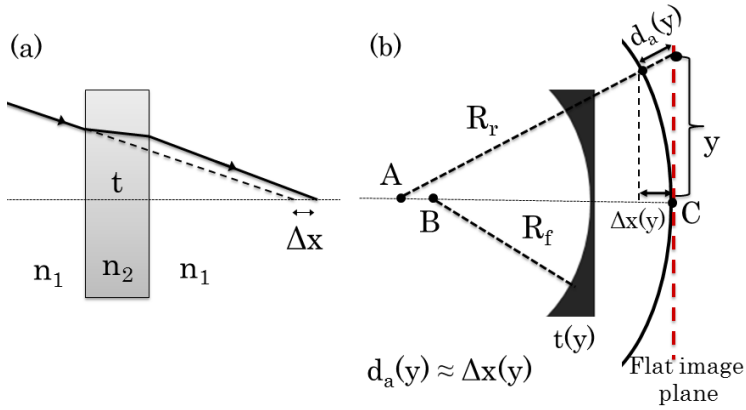

Fig. 5.8 (a) Focus shift (Δx) introduced by a parallel plate in a converging beam; t is the plate thickness, n_1 and n_2 are the refractive indices of the surrounding and plate layers, respectively. **(b)** Petzval image surface and field-flattening lens with relevant parameters; R_r (centered at A) and R_f (centered at B) are the radii of curvature of the imaging system and field-flattening lens, respectively, $\Delta x(y)$ is the horizontal deviation from the flat image plane, and $d_a(y)$ is the focus shift.

Three AWGs were designed, one without a field-flattening lens, and two with different lens designs, all having a free spectral range of 64.8 nm and a resolution of 0.8 nm. Output waveguides were used in order to make a direct comparison between measurement results of AWGs with and without lens. The lens structures

were not on the same mask. This allowed the fabrication in two runs of four devices in total: AWGs with their output waveguides arranged on a straight line, both with and without a field-flattening lens. The two devices without lens made it possible to check for unwanted process variations. The AWGs were fabricated using the SiON channel waveguide Design # 3 specified in Table 2.3. The schematic of the field-flattening lens in the second star coupler is shown in Fig. 5.9a.

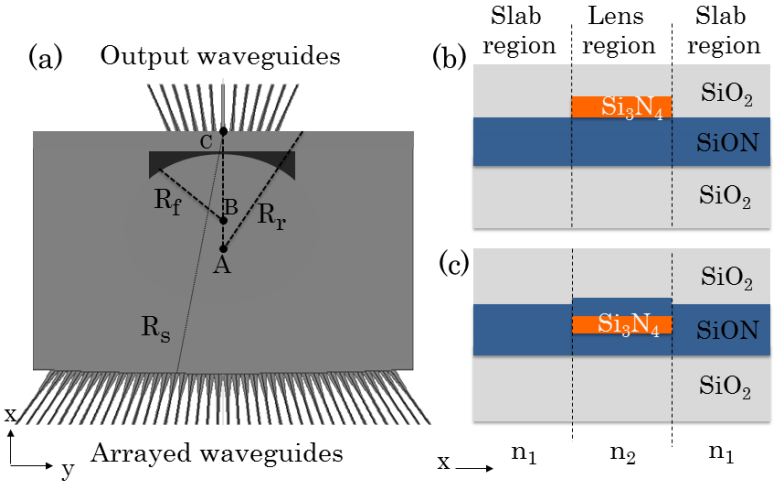

Fig. 5.9 (a) Field-flattening lens in the second star coupler of the AWG. R_r, R_s, and R_f are the radii of curvature of the Rowland circle, the slab region, and the lens, respectively. **(b)** Cross-section of the star coupler with silicon nitride (Si_3N_4) layer on top of the silicon oxynitride (SiON) layer, or **(c)** with Si_3N_4 between SiON layers. n_1 and n_2 are the effective refractive indices of the slab region with and without Si_3N_4 layer, respectively.

For the AWGs with field-flattening lens, the index difference between slab and lens region was introduced by applying a thin silicon nitride (Si_3N_4) layer in the lens region. The Si_3N_4 layer was deposited in LPCVD reactor at a substrate temperature of 800°C. SiH_2CL_2 and NH_3 served as precursors in the deposition process with the relative gas-flow ratio SiH_2CL_2/NH_3 of 0.33. The lens structure was etched in a Plasma Therm 790 RIE reactor applying a gas mixture of CHF_3 and O_2 (100 sccm / 2 sccm) at 28 mTorr pressure, 300 W plasma power, and 20°C substrate temperature. Two different lens designs were implemented; one with a 160-nm-thick Si_3N_4 layer deposited on top of a 1-µm-thick SiON layer (Fig. 5.9b) and one with a 120-nm-thick Si_3N_4 layer sandwiched between 500-nm-thick SiON layers (Fig. 5.9c). In the latter design the SiN layer thickness was reduced (120 nm) in order to obtain the same effective refractive index in the lens region and thereby the same lens radius for both designs. The thickness of the Si_3N_4 layer was chosen as a

compromise between excess loss and minimum lens size providing full coverage of all output waveguides. According to BPM simulation results, the latter design performed better in terms of mode-mismatch-induced excess loss, which was calculated to be 0.9 dB whereas it increased to 2.6 dB in the former design. The radius of curvature R_s of the grating circle was 5531 μm. The effective indices of the slab and the lens region were calculated to be 1.50 and 1.61, respectively, which results in a lens radius of R_f = 189 μm.

5.4.2 Results and discussions

The performance degradation of an AWG due to a non-compensated flat output plane, i.e. without a field-flattening lens, was investigated by comparing its BPM-simulated transmission responses with those of a conventional AWG (outputs placed on the Rowland circle). The results are shown in Fig. 5.10. Without field-flattening lens, large aberrations will be introduced, resulting in high adjacent crosstalk, additional insertion loss, and broader spectral shape at the outer channels. The simulations predict that the AWG with non-optimized flat output plane exhibits degradation in adjacent crosstalk, spectral shape, and insertion loss performance. An excess loss value of 0.5 dB and a 5-dB decrease of adjacent crosstalk was introduced at the outer channels. Such problems become more severe for AWGs with a large number of output waveguides (~2 dB of excess loss and ~16 dB of decrease in adjacent crosstalk for 200 output waveguides) as shown in Fig. 5.10d.

Optical transmission measurements of the realized devices were performed by using the same measurement set-up and characterization technique as described in Section 2.5. The performance improvement by the field-flattening lens was demonstrated by comparing the crosstalk, spectral shape, and insertion loss of the four AWGs, as shown in Fig. 5.11. For the lens design shown in Fig. 5.9b the adjacent crosstalk was improved by 5 dB and an excess loss value of 2.5 dB was introduced by the lens due to high mode mismatch. For the lens design given in Fig. 5.9c the adjacent crosstalk was improved by 2 dB and an excess loss value of only 0.4 dB was introduced by the lens. The overall transmission characteristic of the AWG is given in Fig. 5.12. The non-adjacent crosstalk values of -30 and -25 dB and excess loss values of 0.5 and 4.5 dB were measured for the central and outermost channels, respectively. A center wavelength shift of 17 nm was found to be caused by a higher than designed SiON refractive index and an incomplete etching of the Si_3N_4 layer (~15 nm of residual) in the regions where no lens structure was applied. The incomplete etching also resulted in a smaller index difference (n_2-n_1) between the slab and the lens region and BPM simulations confirmed this to reduce the experimentally observed improvement of adjacent

crosstalk from 6 dB to 2 dB (see Figs. 5.10d and 5.11e). For both lens designs the spectral shape of the transmission peaks became narrower and more symmetric compared to the AWG without lens. From these measurements it can be concluded that the lens design given in Fig. 5.9c is 1.6 dB superior to the lens design given in Fig. 5.9b in terms of excess loss. Although the demonstrated improvement of adjacent crosstalk is rather small, it is expected to be easily improved by optimizing the fabrication procedure.

In conclusion the flat image field of these AWGs makes it possible to butt-couple them to detector arrays, making them very attractive for on-chip OCT applications. Using such an AWG rather than a cleaved conventional one would improve the axial resolution and the signal roll-off with depth of the OCT system significantly.

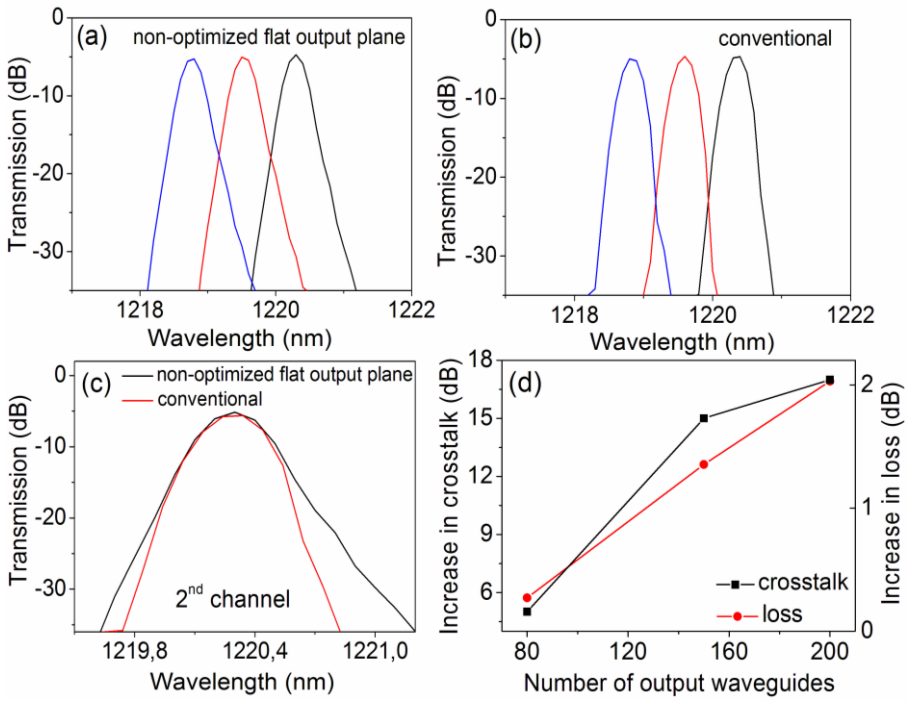

Fig. 5.10 Simulated effect of using a non-optimized flat output plane in an AWG. **(a-c)** 80-Channel device, edge channels (1-3) of **(a)** the flat-output-plane AWG without optimization, and **(b)** the conventional AWG. **(c)** Comparison of the results given in **(a)** and **(b)** for the 2nd channel. **(d)** Increase of crosstalk and loss versus number of output channels.

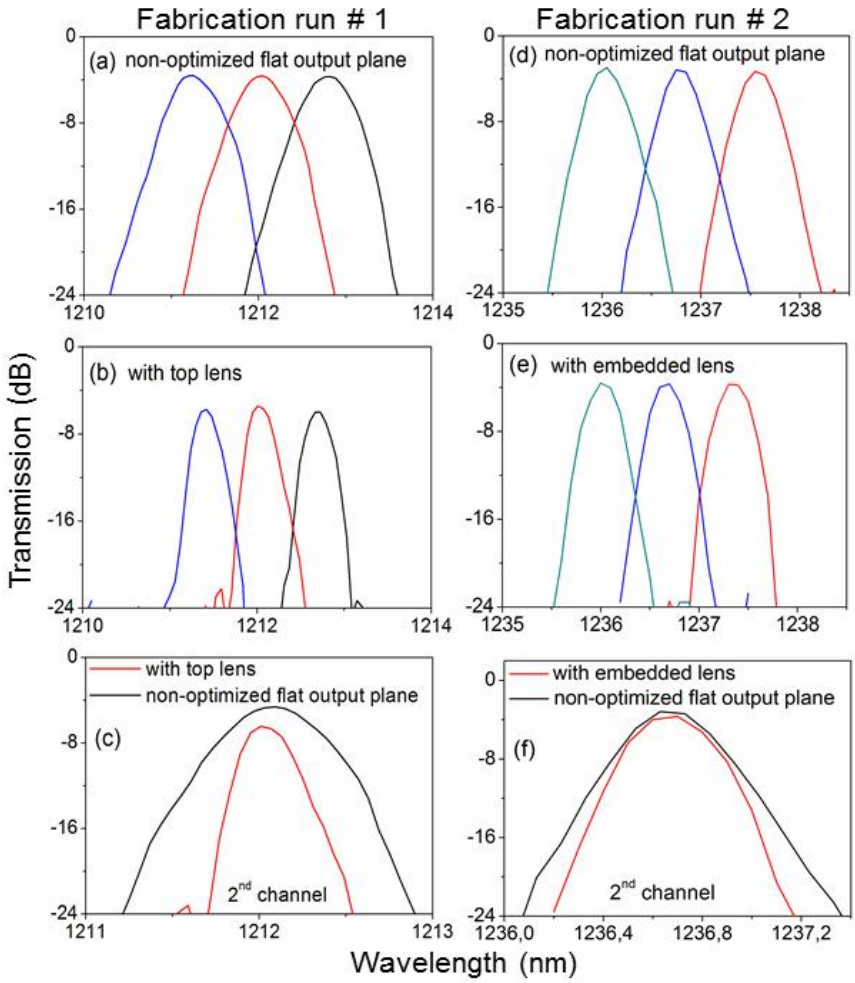

Fig. 5.11 Transmission measurement results for some edge channels of the realized AWGs: **(a, b, c)** the first fabrication run and **(d, e, f)** the second fabrication run. **(a, d)** with a non-optimized flat output plane **(b, c)** with a field-flattening lens where Si_3N_4 layer on top of SiON layer, and **(e, f)** with a field-flattening lens where Si_3N_4 layer embedded between SiON layers.; **(c, f)** comparison of the results given in **(a, b)** and **(d, e)** for the 2nd channel.

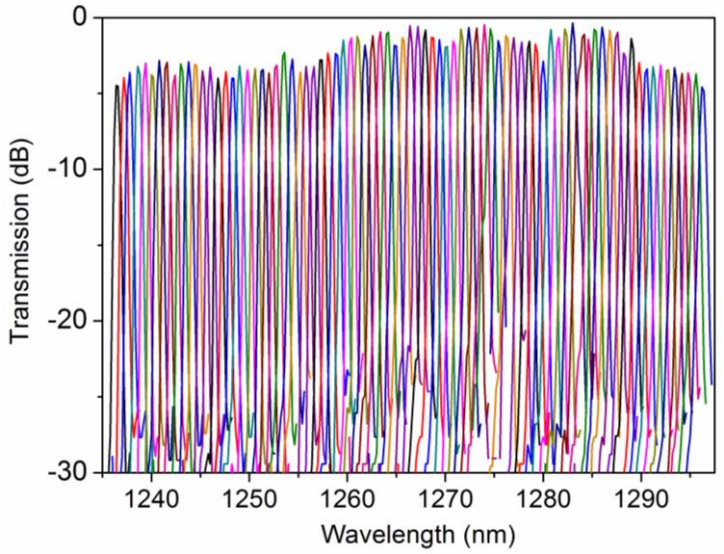

Fig. 5.12 The overall transmission characteristic of the AWG using the lens design given in Fig. 5.9c.

6 Conclusions and outlook

6.1 Conclusions

In the research presented in this thesis, we have focused on design, fabrication, and demonstration of on chip spectral-domain optical coherence tomography (SD-OCT) systems operating around the 800 nm and 1300 nm wavelength ranges to be used in retina and skin imaging, respectively. The on-chip SD-OCT systems consisted of arrayed waveguide gratings (AWGs) and integrated Michelson interferometers (MIs). Silicon oxynitride (SiON) was chosen as the material platform for the device fabrication. SiON-based single-mode channel waveguides were designed at both wavelength ranges to be used as the basic building blocks of the integrated AWGs and MIs.

For integrated MIs two types of wavelength-insensitive 3-dB couplers i.e. balanced and non-uniform adiabatic coupler were designed, fabricated and characterized. Due to fabrication problems, the realized couplers exhibited deviations from the designed 3-dB splitting ratio, which were more severe for the non-uniform adiabatic couplers. The theory and characterization of the couplers are presented in Chapter 3.

OCT imaging was performed using an AWG spectrometer, either in combination with an external MI or with a beam splitter integrated on the same chip. The first OCT image was taken by using the 1300-nm AWG in a fiber-based MI set-up. A maximum depth range of 1 mm and an axial resolution of 20 μm were achieved, and a three-layer scattering phantom was imaged with a SNR of 75 dB at 100 μm depth. OCT images of human skin were obtained using the 1250-nm AWG integrated with a beam splitter built with a non-uniform adiabatic coupler on the same chip. A maximum depth range of 1.4 mm and an axial resolution of 7.5 μm was obtained in tissue. The SNR measured close to the zero delay where both beam splitter arms are equal in length was 74 dB at 0.5 mW optical power on the sample, which includes 5 dB fiber-to-chip coupling loss, 7 dB on-chip coupler loss due to imperfect fabrication, 7.5 dB transmission loss of the standard microscope objectives, and 3 dB AWG excess loss. Although the current SNR of 74 dB is limited by the overall system losses (i.e. non-adiabatic coupler loss, fiber-to-chip coupling loss, objective lens losses, and AWG excess loss) as well as the increased background due to internal scatterings, it can be further increased up to 95 dB by reducing the (1) non-adiabatic coupler loss down to its theoretical value of 0 dB

with an optimized lithography and etching procedure, (2) fiber-to-chip coupling losses down to <0.5 dB either with a spot-size converter [Spu98] or a tapered input waveguide [Mit94], (3) losses arises from using microscope objectives down to <1 dB with proper objective lenses designed specifically for the near infrared range, and (4) AWG excess loss down to <0.5 dB by applying vertical tapers at the interfaces of arrayed waveguides with the FPRs [Sug00].

In Chapter 5 we demonstrated that the depth range of the SD-OCT system using an AWG can be improved towards the level of existing bulk-optics systems by removing the output waveguides of the AWG. The depth range is enhanced from 1 mm to 3.3 mm at 800 nm and to 4.6 mm at 1300 nm. Periodic signal fading that was previously observed in the sensitivity roll-off curve in depth ranging measurements is shown to be evoked by beat-frequency generation between the two polarizations of partially polarized signal light in a birefringent AWG. By carefully controlling the polarization state of light, the signal fading is eliminated. As a permanent solution to this problem, a polarization-independent AWG is demonstrated, which can reduce the size and cost of OCLR and optical coherence tomography systems further by eliminating the components for polarization control.

This work has also shown that SiON to be a very promising material for on-chip OCT applications. Additionally AWG spectrometers have a great potential for realizing large-depth-range and high-axial-resolution on-chip OCT applications by providing sufficiently high resolution and large bandwidth. Throughout this thesis several customized AWG design configurations have been presented, demonstrating the design flexibility of AWGs. In Chapter 2 we presented a new Mach-Zehnder (MZI) synchronized design for flattening the passband of an AWG over a broad wavelength range of 90 nm. A low-loss cascaded AWG system is demonstrated by using this MZI-synchronized flat-top AWG as a primary filter. In Chapter 5 we presented a new flat-focal-field AWG design that utilizes an integrated field-flattening lens placed in the second star coupler. As a proof of concept two 81-channel AWGs, one with and one without the lens, were designed, fabricated, and characterized.

In conclusion, considering the current performance of the partially-integrated SD-OCT systems and the potential of integrated optics, in the foreseeable future the fully-integrated OCT systems will be demonstrated and with their much lower cost, size, and higher stability they will become accessible to a wider group of medical doctors and researchers.

6.2 Outlook

Although the final goal of this PhD thesis has been fulfilled by performing OCT imaging using the partially-integrated SD-OCT system at 1250 nm, additional measurements with 800-nm partially-integrated SD-OCT systems have been planned in Medical University of Vienna after the submission of this thesis. Therefore in the near future these measurements will be carried out in Vienna.

After gaining a lot of experience in OCT measurements and device design, we have realized that the fabricated 800-nm SD-OCT system with the on-chip reference arm, has some drawbacks, namely more power in the reference arm than in the sample arm, 3 dB extra loss due to the Y combiner, and difficulty of *k*-mapping. Reference arm and sample arm powers can be equalized by placing a tunable coupler in the reference arm as depicted in Fig. 6.1. By thermal tuning of the coupler the reference arm intensity can be arranged in such a way that the fringe visibility of the interference signal is optimized. Additionally *k*-mapping can be easily applied in this configuration. Alternatively, the Y combiner can be eliminated by using a loop mirror in the reference arm.

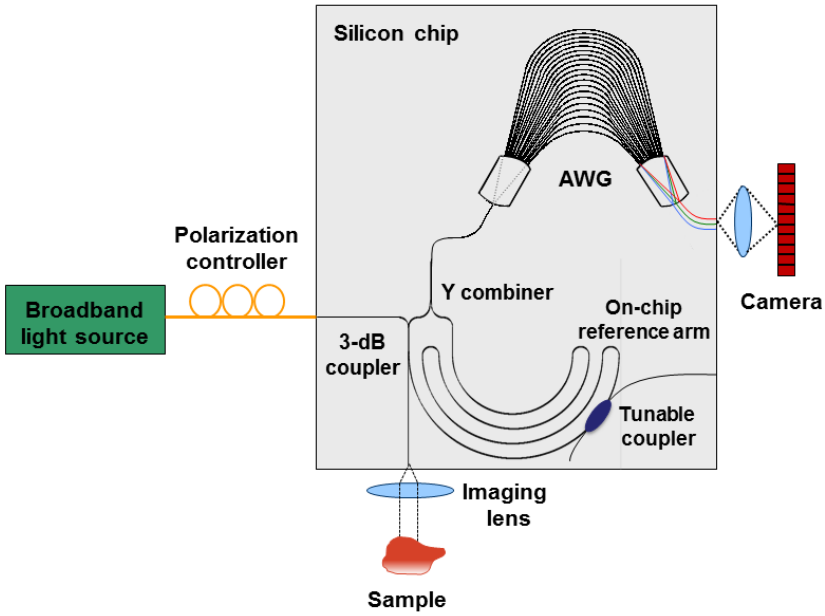

Fig. 6.1 On-chip spectral-domain OCT configuration with a tunable coupler placed on the reference arm in order to control the reference arm power.

Our latest results have demonstrated the feasibility and the great potential of on-chip SD-OCT systems. Therefore continuing in this field is certainly in my future

roadmap. Although spectrometer and MI are the key components of an SD-OCT system to be integrated on a chip, it is necessary to integrate the detector, the light source, and the lenses on the same chip for a fully-integrated SD-OCT system. Integration of these components would further decrease the size and increase the stability of OCT systems. However, realization of these components necessitates either a compatible fabrication technique for heterogeneous integration of active (e.g. InP/InGaAsP) and passive (e.g. SiON) components or accurate and stable wafer bonding techniques [Mat97, Bro07, Mon01]. Ismail et al. have proposed a SiON-compatible microlens fabrication technique which will eliminate the need for bulky lenses in the current configuration [Ism12]. For the integration of active component, wafer bonding techniques have been widely used to demonstrate high performance hybrid platforms and its higher flexibility is more preferable compared to monolithic integration due to the large mismatch in lattice and thermal expansion coefficient between passive and active materials [Yac02]. One possible approach for realizing an integrated light source could be directing the emitted light from active region using 45^{o} turning mirrors towards the passive layer which is bonded to the active layer by using the wafer bonding techniques described elsewhere [Roe06, Roe08].

Appendices

A1. Derivations of AWG design parameters

$$n_s d \sin(\theta_i) + n_c \Delta L + n_s d \sin(\theta_o) = m\lambda\,, \tag{A.1}$$

Considering only the center input waveguide is used (θ_i=0), Eq. (A.1) can be written as

$$n_c \Delta L + n_s d \sin(\theta_o) = m\lambda\,, \tag{A.2}$$

For the center wavelength θ_o=0 Eq. (A.2) becomes

$$\begin{aligned} n_c \Delta L &= m\lambda_c \\ \lambda_c &= \frac{n_c \Delta L}{m}\,, \end{aligned} \tag{A.3}$$

To get the angular dispersion of the AWG, both sides of Eq. (A.2) are differentiated with respect to λ which results in

$$\Delta L \frac{\partial n_c}{\partial \lambda} + n_s d \cos(\theta_o) \frac{\partial \theta_o}{\partial \lambda} = m\,, \tag{A.4}$$

Since θ_o is very small compare to other parameters $cos(\theta_o) \approx 1$. By using $\Delta L = m\lambda_c/n_c$, and using it in Eq. (A.4), the angular dispersion of the AWG becomes

$$\frac{\partial \theta_o}{\partial \lambda} = \frac{m}{d n_s n_c}\left(n_c - \lambda_c \frac{\partial n_c}{\partial \lambda}\right), \tag{A.5}$$

If we assume that the wavelength dependence of the refractive index is zero Eq. (A.5) can be written as

$$\frac{\partial \theta_o}{\partial \lambda} = \frac{m}{d n_s}\,, \tag{A.6}$$

Based on Eq. (A.6), the wavelength separation between two adjacent output waveguides can be found as

$$\delta\lambda = \frac{\Delta x}{R}\left(\frac{\partial\theta_o}{\partial\lambda}\right)^{-1} = \frac{d\Delta x n_s}{mR}, \tag{A.7}$$

Response of the AWG is periodical, i.e. after each change of 2π in phase ($\Delta\phi=\Delta\beta\times\Delta L$), the field will be imaged at the same position which is called the free spectral range (FSR). It can be extracted as

$$\Delta\phi = \Delta\beta\Delta L = \frac{2\pi}{\lambda^2}\Delta\lambda_{FSR}\Delta L, \tag{A.8}$$

By using $\Delta L=m\lambda_c/n_c$

$$\Delta\phi = \frac{2\pi}{\lambda_c{}^2}\Delta\lambda_{FSR}\Delta L\left(\frac{m\lambda_c}{n_c}\right), \tag{A.9}$$

If we solve Eq. (A.9) for $\Delta\lambda_{FSR}$

$$\Delta\lambda_{FSR} = \frac{\lambda_c}{m}, \tag{A.10}$$

The polarization dependent focus shift can also be extracted from Eq. (A.1). If we assume single input and single output waveguides (i = 1. j = 1).Eq. (A.1) becomes

$$n_s d\sin(\frac{\Delta x}{R}) + n_c\Delta L + n_s d\sin(\frac{\Delta x}{R}) = m\lambda, \tag{A.11}$$

Eq. (A.11) can be rewritten by using the small angle approximation, i.e. $\sin(\Delta x/R) \approx \Delta x/R$,

$$\frac{\Delta x n_s d}{R} + n_c\Delta L + \frac{\Delta x n_s d}{R} = m\lambda, \tag{A.12}$$

Considering the effective refractive index difference in core layer for TE and TM polarizations, Eq. (A.12) can be written for TE and TM as

$$\frac{\Delta x_{TE} n_s d}{R} + n_{cTE} \Delta L + \frac{\Delta x_{TE} n_s d}{R} = m\lambda \,, \tag{A.13}$$

$$\frac{\Delta x_{TM} n_s d}{R} + n_{cTM} \Delta L + \frac{\Delta x_{TM} n_s d}{R} = m\lambda \,, \tag{A.14}$$

Here we assume that the effective index of the slab region is the same for TE and TM polarizations. Subtracting Eq. (A.13) from Eq. (A.14) will give the formula of the polarization dependent focus shift as

$$\Delta x_{TE-TM} = \frac{R \Delta L \Delta n_c}{2 n_s d} \,, \tag{A.15}$$

Publications

Peer-reviewed journal articles

1. "Measuring local RF heating in MRI: simulating perfusion in a perfusionless phantom", **B. Imran Akca**, T. O. Tasci, O. Ferhanoglu, S. Guney, C. Yeung, and E. Atalar, Journal of Magnetic Resonance Imaging, vol. 26, pp. 1228-1235, 2007.
2. "A figure of merit for optimization of nanocrystal flash memory design", A. Dana, **B. Imran Akca**, A. Aydinli, R. Turan, and T.G. Finstad, Journal of Nanoscience and Nanotechnology, vol. 8, pp. 510–517, 2008.
3. "Electro-optic and electro-absorption characterization of InAs quantum dot waveguides", **B. Imran Akca**, A. Dana, A. Aydinli, M. Rossetti, L. Li, A. Fiore, and N. Dagli, Optics Express , vol. 16, pp. 3439-3444, 2008.
4. "Comparison of electron and hole charge-discharge dynamics in germanium nanocrystal flash memories", **B. Imran Akca**, Aykutlu Dana, Atilla Aydinli, and Rasit Turan, Applied Physics Letters, vol. 92, pp. 052103, 2008.
5. "Integrated approach to laser delivery and confocal signal detection", N. Ismail, **B. Imran Akca**, F. Sun, K. Wörhoff, R.M. de Ridder, M. Pollnau, and A. Driessen, Optics Letters, vol. 35, pp. 2741-2743, 2010.
6. "Spectral domain optical coherence tomography imaging with an integrated optics spectrometer", V. D. Nguyen[*], **B. Imran Akca**[*], K. Wörhoff, R.M. de Ridder, M. Pollnau, T.G. van Leeuwen, and J. Kalkman, Optics Letters, vol. 36, pp. 1293-1295, 2011. **([*]equally contributed).**
7. "Toward spectral-domain optical coherence tomography on a chip", **B. Imran Akca**, V. D. Nguyen, J. Kalkman, N. Ismail, G. Sengo, F. Sun, T. G. van Leeuwen, A. Driessen, M. Pollnau, K. Wörhoff, and R. M. de Ridder, IEEE Journal of Selected Topics in Quantum Electronics, vol. 18, pp. 1223-1233, 2012.
8. "Polarization-independent enhanced resolution arrayed waveguide grating used in spectral-domain optical low-coherence reflectometry", **B. Imran Akca**, L.Chang, G. Sengo, K. Wörhoff, R. M. de Ridder, and M. Pollnau, IEEE Photonics Technology Letters, vol. 24, pp. 848-850, 2012.
9. "Broad-spectral-range synchronized flat-top arrayed-waveguide grating applied in a 255-channel cascaded spectrometer", **B. Imran Akca**, C. R. Doerr, G. Sengo, K. Wörhoff, M. Pollnau, and R. M. de Ridder, Optics Express, vol. 20, pp. 18313-18318, 2012.
10. "Flat-focal-field arrayed-waveguide grating using an integrated field-flattening lens", **B. Imran Akca**, G. Sengo, M. Pollnau, K. Wörhoff, A. Driessen, and R. M. de Ridder, Optics Letters, vol. 37, pp.4281-4283, 2012.

11. "Miniature spectrometer and beam splitter for optical coherence tomography on a silicon chip", **B. Imran Akca**, B. Považay, A. Alex, K. Wörhoff, R. M. de Ridder, W. Drexler, and M. Pollnau, in preparation.

Conference presentations/papers

1. "Measuring local RF heating in MRI: simulating perfusion in a perfusionless phantom", **B. Imran Akca,** T. O. Tasci, O. Ferhanoglu, D. Bacanli, C. Yeung, and E. Atalar, ISMRM 14th Scientific Meeting and Exhibition, 8-14 May 2006, Seattle, WA, USA, (Poster presentation).
2. "Effect of tunnel dielectric thickness on performance of nanocrystals memory devices with silicon nanocrystals in silicon nitride studied by graded growth", A. Dâna, **B. Imran Akca**, A. Aydinli, and S. Tokay, EMRS, 28-30 May 2007, Strasbourg, France, (Oral presentation).
3. "Characterization of multilayer self-organized InAs quantum dot embedded waveguides at 1.3 and 1.5 μm", **B. Imran Akca**, A. Dana, A. Aydinli, M. Rossetti, L. Li, A. Fiore, and N. Dagli, CLEO Europe IQEC, 17-22 June 2007, Munich, Germany, (Oral presentation).
4. "Modulation of multilayer InAs quantum dot waveguides under applied electric field", **B. Imran Akca**, A. Dana, A. Aydinli, M. Rossetti, L. Li, A. Fiore, and N. Dagli, FiO (OSA Annual Meeting), 15-20 September 2007, San Jose, CA, USA, (Oral presentation).
5. "Integrated AWG spectrometer for on-chip optical coherence tomography and Raman spectroscopy", **B. Imran Akca**, N. Ismail, F. Sun, A. Driessen, K. Wörhoff, M. Pollnau, R. M. de Ridder, V. D. Nguyen, J. Kalkman, and T. G. van Leeuwen, ECIO, 7-9 April 2010, Cambridge, United Kingdom, (Oral presentation).
6. "Integrated arrayed waveguide grating spectrometer for on-chip optical coherence tomography", **B. Imran Akca**, N. Ismail, F. Sun, V. D. Nguyen, J. Kalkman, T. G. van Leeuwen, A. Driessen, K. Wörhoff, M. Pollnau, and R. M. de Ridder, CLEO, 16-21 May 2010, San Jose, CA, USA, (Poster presentation).
7. "Design of low-loss arrayed waveguide gratings for applications in integrated Raman spectroscopy", N. Ismail, **B. Imran Akca**, A. C. Baclig, P. J. Caspers, F. Sun, K. Wörhoff, R. M. de Ridder, M. Pollnau, and A. Driessen, CLEO, 16-21 May 2010, San Jose, CA, USA, (Oral presentation).
8. "High resolution silicon-oxynitride arrayed waveguide grating spectrometers", **B. Imran Akca**, N. Ismail, G. Sengo, F. Sun, K. Wörhoff, M. Pollnau, and R. M. de Ridder, Proc. of the 2010 Annual Symposium of the IEEE Photonics Benelux Chapter, 18-19 Nov 2010, pp. 125-128, Delft, The Netherlands, (Oral presentation).

9. "Toward miniaturized optical coherence tomography", **B. Imran Akca**, V. D. Nguyen, J. Kalkman, T.G. van Leeuwen, K. Wörhoff, R. M. de Ridder, and M. Pollnau, The Sense of Contact 13, 7 April 2011, Zeist, The Netherlands, (Poster presentation).
10. "Toward miniaturized optical coherence tomography", **B. Imran Akca**, V. D. Nguyen, J. Kalkman, T.G. van Leeuwen, K. Wörhoff, M. Pollnau, and R. M. de Ridder, CLEO, 1-6 May 2011, Baltimore, MD, USA, (Oral presentation).
11. "High-resolution integrated spectrometers in silicon-oxynitride", **B. Imran Akca**, N. Ismail, F. Sun, A. Driessen, K. Wörhoff, M. Pollnau, and R.M. de Ridder, CLEO, 1-6 May 2011, Baltimore, MD, USA, (Poster presentation).
12. "Integrated spectrometers for spectral-domain optical coherence tomography", **B. Imran Akca**, V. D. Nguyen, J. Kalkman, T.G. van Leeuwen, K. Wörhoff, R. M. de Ridder, and M. Pollnau CLEO/Europe, 22-26 May 2011, Munich, Germany, (Oral presentation).
13. "Biophotonic sensors on a microchip for trace-gas detection, DNA and enzyme analysis, Raman spectroscopy, and optical coherence tomography", M. Pollnau, **B. Imran Akca**, N. Ismail, C. Dongre, V. S. Pham, K. Wörhoff, R. M. de Ridder, and H. J. W. M., Joint Annual Meeting of the Swiss Physical Society and the Austrian Physical Society, 15-17 June 2011, Lausanne, Switzerland, (Oral presentation).
14. "Silicon oxynitride technology for integrated optical solutions in biomedical applications", K. Wörhoff, N. Ismail, **B. Imran Akca**, M. Pollnau, R. M. de Ridder, 13th International Conference on Transparent Optical Networks, 26-30 June 2011, Stockholm, Sweden, (Oral presentation).
15. "Towards spectral-domain optical coherence tomography on a silicon chip", **B. Imran Akca**, K. Wörhoff, V. D. Nguyen, J. Kalkman, T.G. van Leeuwen, R. M. de Ridder, and M. Pollnau, International Laser Physics Workshop, 11-15 July 2011, Sarajevo, Bosnia and Herzegovina, (Oral presentation).
16. "Towards spectral-domain optical coherence tomography on a silicon chip", **B. Imran Akca**, V. D. Nguyen, J. Kalkman, T.G. van Leeuwen, K. Wörhoff, R. M. de Ridder, and M. Pollnau, International Quantum Electronics Conference and Conference on Lasers and Electro-Optics Pacific Rim, 28 August - 1 September 2011, Sydney, Australia, (Oral presentation).
17. "Integrated AWG spectrometer for on-chip optical coherence tomography", **B. Imran Akca**, L. Chang, G. Sengo, V. D. Nguyen, J. Kalkman, T. G. van Leeuwen, K. Wörhoff, M. Pollnau, and R. M. de Ridder, ECIO, 18-20 April 2012, Sitges, Spain, (Oral presentation).
18. "Broad spectral range synchronized flat-top arrayed waveguide grating", **B. Imran Akca**, C. R. Doerr, M. Pollnau, and R. M. de Ridder, CLEO, 1-6 May 2012, San Jose, CA, USA, (Oral presentation).

19. “Towards Raman spectroscopy on a microchip”, **B. Imran Akca**, N. Ismail, L. Chang, K. Wörhoff, R.M. de Ridder, and M. Pollnau, SciX – The Great Scientific Exchange, Kansas City, Missouri, 2012, session "Emerging Raman Techniques and Applications", Final Program Abstracts, p. 117, No. 138 (Invited talk).

References

[Ada92] R. Adar, C. Henry, R. Kazarinov, R. Kistler, and G. Weber, "Adiabatic 3-dB couplers, filters, and multiplexers made with silica waveguides on silicon," J. Lightwave Technol. 10, 46-50 (1992).

[Akc12] B. I. Akca, L. Chang, G. Sengo, K. Wörhoff, R. M. de Ridder, and M. Pollnau, "Polarization-independent enhanced-resolution arrayed-waveguide grating used in spectral-domain optical low coherence reflectometry," IEEE Photon. Technol. Lett. 24, 848-850 (2012).

[Ale10] A. Alex, B. Povazay, B. Hofer, S. Popov, C. Glittenberg, S. Binder, and W. Drexler, "Multispectral in vivo three-dimensional optical coherence tomography of human skin," J Biomed Opt. 15, 026025(1-14) (2010).

[Ame96] M. R. Amersfoort, J. B. D. Soole, H. P. LeBlanc, N. C. Andreadakis, A. Rajhel, and C. Caneau, "Passband broadening of integrated arrayed waveguide filters using multimode interference couplers," Electron. Lett. 32, 449-451 (1996).

[And08] P. E. Andersen, T. M. Jørgensen, L. Thrane, A. Tycho and H. T. Yura, "Optical coherence tomography: biological and medical physics, biomedical engineering," 2008, Chapter 5, pp. 73-115, DOI: 10.1007/978-3-540-77550-8_3.

[Avr06] I. Avrutsky, K. Chaganti, I. Salakhutdinov, and G. Auner, "Concept of a miniature optical spectrometer using integrated optical and micro-optical components," Appl. Opt. 45, 7811 (2006).

[Bal10] E. Margallo-Balbas, M. Geljon, G. Pandraud, and P. J. French, "Miniature 10 kHz thermo-optic delay line in silicon," Opt. Lett. 35, 4027-4029 (2010).

[Bar04] Y. Barbarin, X. J. M. Leijtens, E. A. J. M. Bente, C. M. Louzao, J. R. Kooiman, and M. K. Smit, "Extremely small AWG demultiplexer fabricated on InP by using a double-etch process", IEEE Photon. Technol. Lett. 16, 2478-80 (2004).

[Bon99] G. L. Bona, R. Germann, F. Horst, B. J. Offrein, and H. W. M. Salemink, "Versatile silicon-oxynitride planar lightwave circuits for interconnect applications," in Proc. of Parallel Interconnects, 145-148 (1999).

[Bou01] S. Bourquin, P. Seitz, and R. P. Salathé, "Optical coherence tomography based on a two-dimensional smart detector array," Opt. Lett. 26, 512-514 (2001).

[Bou05] S. Bourquin, L. Laversenne, S. Rivier, T. Lasser, R. P. Salathé, M. Pollnau, C. Grivas, D. P. Shepherd, and R. W. Eason, "Parallel broadband fluorescent light source for optical coherence tomography," Proc. SPIE, Coherence Domain Optical Methods and Optical Coherence Tomography in Biomedicine IX, 5690, San Jose, CA, USA, 2005, pp. 209-213.

[Bre96] M. E. Brezinski, G.J.Tearney, B.E. Bouma, S.A. Boppart, M.R. Hee, E.A Swanson, J.F. Southern, J.G. Fujimoto, "Imaging of coronary artery

microstructure (in vitro) with optical coherence tomography," Am. J. Cardiology 77, 92-93 (1996).

[Bro07] J. Brouckaert, G. Roelkens, D. van Thourhout, and R. Baets, "Thin-Film III–V photodetectors integrated on silicon-on-insulator photonic ICs," J. Lightwave Technol. 25, 1053-1060 (2007).

[Cen04] B. Cense, N. Nassif, T. Chen, M. Pierce, S.-H. Yun, B. Park, B. Bouma, G. Tearney, and J. de Boer, "Ultrahigh-resolution high-speed retinal imaging using spectral-domain optical coherence tomography," Opt. Express 12, 2435–2447 (2004).

[Che03] M. Cherchi, "Wavelength-flattened directional couplers: a geometrical approach," Appl. Opt. 42, 7141-7148 (2003).

[Che07[a]] P. Cheben, J. H. Schmid, A. Delage, A. Densmore, S. Janz, B. Lamontagne, J. Lapointe, E. Post, P. Waldron, and D. X. Xu,, "A high-resolution silicon-on-insulator arrayed waveguide grating microspectrometer with sub-micrometer aperture waveguides," Opt. Express 15, 2299-2306 (2007).

[Che07[b]] P. Cheben, "Wavelength dispersive planar waveguide device: Echelle gratings and arrayed waveguide gratings," in Optical Waveguide: From Theory to Applied Technologies, M. L. Calvo and V. Laksminarayanan, eds. (Taylor & Francis, 2007), Chap. 5.

[Cho08] D. Choi, H. Hiro-Oka, H. Furukawa, R. Yoshimura, M. Nakanishi, K. Shimizu, and K. Ohbayashi, "Fourier domain optical coherence tomography using optical demultiplexers imaging at 60,000,000 lines/s," Opt. Lett. 33, 1318-1320 (2008).

[Chu09] R. W. Chuang and Z. L. Liao, "2 x 2 thermo-optic silicon oxynitride optical switch based on the integrated multimode interference waveguides," J. Electrochem. Soc. 157, H149-H152 (2009).

[Cul00] D. Culemann, A. Knuettel, and E. Voges, "Integrated optical sensor in glass for optical coherence tomography," IEEE J. Select. Topics Quantum Electron. 6, 730-734 (2000).

[Cve09] N. Cvetojevic, J. S. Lawrence, S. C. Ellis, J. Bland-Hawthorn, R. Haynes, and A. Horton, "Characterization and on-sky demonstration of integrated photonic spectrograph for astronomy," Opt. Express 17, 18643-18650 (2009).

[Dha10] A. P. Dham, B. D'Alessandro, and X. Fu, "Optical imaging modalities for biomedical applications," IEEE Rev. Biomedical Engineering 3, 69-92 (2010).

[Doe02] C. R. Doerr, L. W. Stulz, R. Pafchek, and S. Shunk, "Compact and low-loss manner of waveguide grating router passband flattening and demonstration in a 64-channel blocker/multiplexer," IEEE Photon. Technol. Lett. 14, 56-58 (2002).

[Doe03[a]] C. R. Doerr, R. Pafchek, and L. W. Stulz,, "Integrated band demultiplexer using waveguide grating routers," IEEE Photon. Technol. Lett. 23, 1088-1090 (2003).

[Doe03[b]] C. R. Doerr, R. Pafchek, and L. W. Stulz, "Compact and low-loss integrated box-like passband multiplexer," IEEE Photon. Technol. Lett. 15, 918-920 (2003).

[Dra91] C. Dragone, "An N x N optical multiplexer using a planar arrangement of two star couplers," IEEE Photon. Technol. Lett. 3, 812-815 (1991).

[Dra95] C. Dragone, "Frequency routing device having a wide and substantially flat passband," U. S. Patent 5412744, May 2 (1995).

[Dre01] W. Drexler, U. Morgner, R. K. Ghanta, F. X. Kaertner, J. S. Schuman, and J. G. Fujimoto, "Ultrahigh resolution ophthalmic optical coherence tomography," Nature Med. 7, 502-507 (2001).

[Fer95] A. F. Fercher, C. K. Hitzenberger, G. Kamp, and S. Y. Elzaiat, "Measurement of intraocular distances by backscattering spectral interferometry," Opt. Commun. 117, 43–48 (1995).

[Fuk04] T. Fukazawa, F. Ohno, and T. Baba, "Very compact arrayed-waveguide-grating demultiplexer using Si photonic wire waveguides," Jpn. J. Appl. Phys. 43, L673-L675 (2004).

[Ger00] R. Germann, H. W. M. Salemink, R. Beyeler, G. L. Bona, F. Horst, I. Maasarek, and B. J. Offrein, "Silicon oxynitride layers for optical waveguide applications," J. Electrochem. Soc. 147, 2237–2241 (2000).

[Gha91] A. Ghatak and K. Thygarajan, Optical Electronics, Cambridge University Press, Ch.14, pp.447, 1991.

[Gol90] D. S. Goldman, P. L. White, and N. C. Anheier, "Miniaturized spectrometer employing planar waveguides and grating couplers for chemical analysis," Appl. Opt. 29, 4583 (1990).

[Gon05] A. A. Goncharov, S. V. Kuzmin, V. V. Svetikov, K. K. Svidzinskii, V. A. Sychugov, and N. V. Trusov ,"Integrated optical demultiplexer based on the SiO_2–SiON waveguide structure," Quantum Electron. 35, 1163-1166 (2005).

[Ham11] D. X. Hammer, "Advances in retinal imaging," in Advances in Optical Imaging for Clinical Medicine, N. Iftimia, W. R. Brugge, and D. X. Hammer, eds. (Wiley, NJ, USA, 2011), pp. 85-161.

[Häu98] G. Häusler and M. W. Lindner, " 'Coherence radar' and 'spectral radar' —New tools for dermatological diagnosis," J. Biomed. Opt. 3, 21–31 (1998).

[Hib02] Y. Hibino, "Recent advances in high-density and large-scale AWG multi/demultiplexers with higher index-contrast silica-based PLCs," IEEE J. Select. Topics Quantum Electron. 8, 1090-1101 (2002).

[Hof09] B. Hofer, B. Povazay, B. Hermann, A. Unterhuber, G. Matz, and W. Drexler "Dispersion encoded full range frequency domain optical coherence tomography," Opt. Express 17, 7-24 (2009).

[Hu07] Z. Hu, Y. Pan, and A. M. Rollins, "Analytical model of spectrometer- based two-beam spectral interferometry," Appl. Opt. 46, 8499-8505 (2007).

[Hua91] D. Huang, E. A. Swanson, C. P. Lin, J. S. Schuman, W. G. Stinson, W. Chang, M. R. Hee, T. Flotte, K. Gregory, C. A. Puliafito, and J. G. Fujimoto, "Optical coherence tomography," Science 254, 1178-1181 (1991).

[Hua94] W. P. Huang, "Coupled-mode theory for optical waveguides: an overview," J. Opt. Soc. Am. 11, 963- 983 (1994).

[Ino02] Y. Inoue, M. Oguma, T. Kitoh, M. Ishii, T. Shibata, Y. Hibino, H. Kawata, and T. Sugie, "Low-crosstalk 4-channel coarse WDM filter using silica-based planar-lightwave-circuit," in Proc. Optical Fiber Communication Conf. Exhibit 2002 (OFC 2002), Paper TuK6, pp. 75-76.

[Ism11] N. Ismail, L. P. Choo-Smith, K. Wörhoff, A. Driessen, A. C. Baclig, P. J. Caspers, G. J. Puppels, R. M. de Ridder, and M. Pollnau, "Raman spectroscopy with an integrated arrayed-waveguide grating," Optics Lett. 36, 4629-4631 (2011).

[Ism12] N. Ismail, L. Chang, G. Sengo, R. M. de Ridder, M. Pollnau, and K. Wörhoff, "Polymer microlenses for collimating light from single-mode silicon oxynitride optical waveguides," in *16th European Conference on Integrated Optics, ECIO 2012, 18-20 April 2012*, Sitges-Barcelona, Spain.

[Jia12] Y. Jiao, B. W. Tilma, J. Kotani, R. Nötzel, M. K. Smit, S. He, and E. A. Bente, "InAs/InP(100) quantum dot waveguide photodetectors for swept-source optical coherence tomography around 1.7 μm," Opt. Express 13, 3675-3692 (2012).

[Jun05] W. Jung, J. Zhang, J. Chung, P. Wilder-Smith, M. Brenner, J. S. Nelson, and Z. Chen, "Advances in oral cancer detection using optical coherence tomography", IEEE J. Select. Topics in Quantum Electron. 11, 811-817 (2005).

[Kin78] R. Kingslake, Lens Design Fundamentals (Academic Press, 1978).

[Kog76] H. Kogelnik and R.V. Schumidt, "Switched directional couplers with alternating Δβ,'' IEEE J. Quantum Electron. QE-12, 396-401 (1976).

[Koh97] M. Kohtoku, H. Sanjoy, S. Oku, Y. Kadota, Y. Yoshikuni, and Y. Shibata, "InP based 64-channel arrayed waveguide grating with 50 GHz channel spacing and up to -20 dB crosstalk," Electron. Lett. 33, 1786–1787 (1997).

[Lee04] T. H. Lee, K. H. Tu, and C. T. Lee, "Novel structure of an arrayed-waveguide grating multiplexer with flat spectral response," Microw. Opt. Technol. Lett. 41, 444-445 (2004).

[Lei04] R. Leitgeb, W. Drexler, A. Unterhuber, B. Hermann, T. Bajraszewski, T. Le, A. Stingl, and A. Fercher, "Ultrahigh resolution Fourier domain optical coherence tomography," Opt. Express 122, 156–2165 (2004).

[Lei04*] L. Leick, K. Zenth, C. Laurent-Lund, T. Koster, L.-U.A Andersen, L. Wang, B. H. Larsen, L. P. Nielsen, and K. E. Mattsson, "Low loss, polarization insensitive SiON components,"in Proc. OFC 2004 Los Angeles, 2004, MF40.

[Lim99] D. Lim, B.E. Little, K. Lee, M. Morse, H. Fujimoto, H.A. Haus and L.C. Kimerling, "Micron-sized channel dropping filters using Si waveguide devices," in Proc. SPIE, 3847, 65 (1999).

[Lis10] U. L. Mueller-Lisse, M. Bader, M. Bauer, E. Engelram, Y. Hocaoglu, M. Püls, O.A. Meissner, G. Babaryka, R.Sroka, C.G. Stief, M.F. Reiser and U.G. Mueller-Lisse, "Optical coherence tomography of the upper urinary tract: Review of initial experience ex vivo and in vivo," Medical Laser App. 25, 44-52 (2010).

[Lit97] B. E. Little and T. E. Murphy, "Design rules for maximally flat wavelength-insensitive optical power dividers using Mach-Zehnder structures," IEEE Photon. Technol. Lett. 9, 1607-1609 (1997).

[Lou55] W. H. Louisell, "Analysis of the single tapered mode coupler," The Bell Syst. Tech. J. 853-870 (1955).

[Lu 05] S. Lu, C. Yang, Y. Yan, G. Jin, Z. Zhou, W. H. Wong, and E. Y. B. Pun, "Design and fabrication of a polymeric flat focal field arrayed waveguide grating," Opt. Express 13, 9982-9994 (2005).

[Mat97] D. L. Mathine, "The integration of III–V opto-electronics with silicon circuitry," IEEE J. Sel. Topics Quantum Electron. 3, 952–959 (1997).

[Mil54] S. E. Miller, "Coupled wave theory and waveguide applications," Bell Syst. Tech. J. 33, 661-719 (1954).

[Mit94] O. Mitomi, K. Kasaya, and H. Miyazawa, "Design of a single-mode tapered waveguide for low-loss chip-to-fiber coupling," IEEE J. Quantum Electron. 30, 1787–1793 (1994).

[Mon01] C. Monat, C.Seassal, X. Letartre, P. Viktorovitch, P. Regreny, M. Gendry, P. Rojo-Romeo, G.Hollinger, E. Jalaguier, S. Pocas, B. Aspar, "InP 2D photonic crystal microlasers on silicon wafer: room temperature operation at 1.55um," Electronics Lett. 37, 764-765 (2001).

[Ngu10] V. D. Nguyen, N. Ismail, F. Sun, K. Wörhoff, T. G. van Leeuwen, and J. Kalkman, "SiON integrated optics elliptic couplers for Fizeau-based optical coherence tomography," IEEE J. Lightwave Technol. 28, 2836-2842 (2010).

[Oka95] K. Okamoto and H. Yamada, "Arrayed-waveguide grating multiplexer with flat spectral response," Opt. Lett. 20, 43-45 (1995).

[Oka96] K. Okamoto and A. Sugita, "Flat spectral response arrayed-waveguide grating multiplexer with parabolic waveguide horns," Electron. Lett. 32, 1661-1662 (1996).

[Pal05] C. Palmer, Diffraction Grating Handbook, 6th edition, Newport Corporation (2005).

[Pit98] C. Pitris, M. E. Brezinski, B. E. Bouma, G. J. Tearney, J. F. Southern and J. G. Fujimoto, "High resolution imaging of the upper respiratory tract with optical coherence tomography," Am. J. Respir. Crit. Care Med. 157, 1640-1644 (1998).

[Pit99] C. Pitris, A. Goodman, S. A. Boppart, J. J. Libus, J. G Fujimoto, M. E. Brezinski, "High-resolution imaging of gynecologic neoplasms using optical coherence tomography," Obstetrics & Gynecology 93, 135-139 (1999).

[Pot08] B. Potsaid, I. Gorczynska, V. J. Srinivasan, Y. Chen, J. Jiang, A. Cable, and J. G. Fujimoto, "Ultrahigh speed spectral/Fourier domain OCT ophthalmic imaging at 70,000 to 312,500 axial scans per second," Opt. Express 16, 15149–15169 (2008).

[Pot10] B. Potsaid, B. Baumann, D. Huang, S. Barry, A. E. Cable, J. S. Schuman, J. S. Duker, and J. G. Fujimoto, "Ultrahigh speed 1050 nm swept source/Fourier domain OCT retinal and anterior segment imaging at 100,000 to 400,000 axial scans per second," Opt. Express 18, 20029-20048 (2010).

[Roe06] G. Roelkens, J. Brouckaert, D. Van Thourhout, R. Baets, R. Nötzel, and M. Smit, "Adhesive bonding of InP/InGaAsP dies to processed SOI wafers using DVS-bis-BCB, " J. Electrochem. Soc. 153, G1015 (2006).

[Roe08] G. Roelkens, J. Brouckaert, L. Liu, J. Van Campenhout, F. Van Laere, D. Van Thourhout, and R. Baets, "Wafer bonding and heterogeneous integration: technology and integrated devices," ECIO, Netherlands, pp. 87-90 (2008).

[Row83] H. A. Rowland, "On concave gratings for optical purposes," Phil. Mag. 16, 197-210 (1883).

[San96] D. Sander, O. Blume, and J. Müller, "Microspectrometer with slab-waveguide transmission gratings," Appl. Opt. 35, 4096 (1996).

[San01] D. Sander and J. Mueller, "Selffocussing phase transmission grating for an integrated optical microspectrometer," Sens. Actuat. A 88, 1 (2001).

[Sch00] B. Schauwecker, G. Przyrembel, B. Kuhlow, and C. Radehaus, "Small-size silicon-oxynitride AWG demultiplexer operating around 725 nm," IEEE Photon. Technol. Lett. 12, 1645-1646 (2000).

[Shi02] T. Shimoda, K. Suzuki, S. Takaesu, and A. Furukawa, "Low-loss, polarization independent, silicon-oxynitride waveguides for high-density integrated planar lightwave circuits," Proc. 28th Europ. Conf. Opt. Commun. (ECOC'02), Copenhagen, Denmark, paper 4.2.2 (2002).

[Smi88] M. K. Smit, "New focusing and dispersive planar component based on an optical phased array," Electron. Lett. 24, 385-386 (1988).

[Smi96] M. K. Smit and C. van Dam, "PHASAR-based WDM-devices: Principles, design and applications," IEEE J. Select. Topics Quantum Electron. 2, 236-250 (1996).

[Spu98] M. M. Spühler, B. J. Offrein, G. Bona, R. Germann, I. Massarek, and D. Erni "A very short planar silica spot-size converter using a nonperiodic segmented waveguide," IEEE J. Lightwave Technol. 16, 1680–1685 (1998).

[Sug00] A. Sugita, A. Kaneko, K. Okamoto, M. Itoh, A. Himeno, and Y. Ohmori, "Very low insertion loss arrayed-waveguide grating with vertically tapered waveguides," IEEE Photon. Technol. Lett. 12, 1180–1182 (2000).

[Swa92] E. A. Swanson, D. Huang, M. R. Hee, J. G. Fujimoto, C. P. Lin, and C. A. Puliafito, "High-speed optical coherence domain reflectometry," Opt. Lett. 17, 151-153 (1992).

[Tka90] H. Takahashi, S. Suzuki, K. Kato, and I. Nishi, "Arrayed-waveguide grating for wavelength division multi/demultiplexer with nanometre resolution," Electron. Lett. 26, 87-88 (1990).

[Tak99] K. Takada, H. Yamada, and K. Okamoto, "320-channel multiplexer consisting of a 100 GHz-spaced parent AWG and 10 GHz-spaced subsidiary AWGs," Electron. Lett. 35, 824-826 (1999).

[Tak00] K. Takada, M. Abe, T. Shibata, M. Ishii, Y. Inoue, H. Yamada, Y. Hibino, and K. Okamoto, "10 GHz-spaced 1010-channel AWG filter achieved by tandem connection of primary and secondary AWGs," in Proc. Eur. Conf. Optical Communications (ECOC 2000), Munich, Germany, 2000, Postdeadline Paper PD3-8.

[Tak01] K. Takada, M. Abe, T. Shibata, and K. Okamoto, "10 GHz-spaced 1010-channel tandem AWG filter consisting of one primary and ten secondary AWGs," IEEE Photon. Technol. Lett. 13, 577-578 (2001).

[Tak02[a]] K. Takada, M. Abe, T. Shibata, and K. Okamoto, "1-GHz-spaced 16-channel arrayed-waveguide grating for a wavelength reference standard in DWDM network systems," IEEE J. Lightwave Technol. 20, 850-853 (2002).

[Tak02[b]] K. Takada, M. Ade, T. Shibita, and K. Okamoto, "A 25-GHz-spaced 1080-channel tandem multi/demultiplexer covering the S-, C-, and L-bands using an arrayed-waveguide grating with Gaussian passbands as primary filter," IEEE Photon. Technol. Lett. 14, 648-650 (2002).

[Tak02[c]] K. Takada, M. Abe, T. Shibata, and K. Okamoto, "Low-loss 10-GHz-spaced tandem multi/demultiplexer with more than 1000 channels using a 1×5 interference multi/demultiplexer as a primary filter," IEEE Photon. Technol. Lett. 14, 59-61 (2002).

[Tak05] K. Takada, M. Abe, T. Shibata, and K. Okamoto, "5 GHz-spaced 4200-channel two-stage tandem demultiplexer for ultra-multi-wavelength light source using supercontinuum generation," Electron. Lett. 38, 572-573 (2005).

[Tea97[a]] G. J. Tearney, M. E. Brezinski, J. F. Southern, B. E. Bouma, S. A. Boppart, J. G. Fujimoto, "Optical biopsy in human gastrointestinal tissue using optical coherence tomography," Am J Gastroenterol. 92, 1800-1804 (1997).

[Tea97[b]] G. J. Tearney, M. E. Brezinski, J. F. Southern, B. E. Bouma, S. A. Boppart, J.G.Fujimoto, "Optical biopsy in human urologic tissue using optical coherence tomography," J. Urology 157, 1915-1919 (1997).

[Til12] B. W. Tilma, Y. Jiao, J. Kotani, E. Smalbrugge, H. P. M. M. Ambrosius, P. J. Thijs, X. J. M. Leijtens , R. Nötzel, M. K. Smit, and E. A. J. M. Bente, "Integrated tunable quantum-dot laser for optical coherence tomography in the 1.7 um wavelength region," IEEE J. Quantum Electron. 48, 87-98 (2012).

[Tri97] P. D. Trinh, S. Yegnanarayanan, F. Coppinger, and B. Jalali, “Silicon-on-insulator (SOI) phased-array wavelength multi-demultiplexer with extremely low polarization sensitivity,” IEEE Photon. Technol. Lett. 9, 940-942 (1997).

[Vel76] C. H. F. Velzel, “A general theory of the aberration of diffraction gratings and gratinglike optical instruments,” J. Opt. Soc. Am. 66, 346-353 (1976).

[Woj04] M. Wojtkowski, V. Srinivasan, T. Ko, J. Fujimoto, A. Kowalczyk, and J. Duker, “Ultrahigh-resolution, high-speed, Fourier domain optical coherence tomography and methods for dispersion compensation,” Opt. Express 12, 2404–2422 (2004).

[Wör99] K. Wörhoff, P. V. Lambeck, and A. Driessen, "Design, tolerance analysis, and fabrication of silicon oxynitride based planar optical waveguides for communication devices", I Lightwave Technol. 17, 1401-1407 (1999).

[Wör07] K. Wörhoff, C. G. H. Roeloffzen, R. M. de Ridder, A. Driessen, and P. V. Lambeck, “Design and application of compact and highly tolerant polarization-independent waveguides,” IEEE J. Lightwave Technol. 25, 1276-1282 (2007).

[Yac02] B. G. Yacobi, S. Martin, K. Davis, A. Hudson, M. Hubert, “Adhesive bonding in microelectronics and photonics,” J. Appl. Phys.: Appl. Phys. Rev. 91,6227–6262 (2002).

[Yar73] A. Yariv, “Coupled mode theory for guided wave optics,” IEEE J. Quantum Electron. QE-9, 919-933 (1973).

[You87] R. C. Youngquist, S. Carr, and D. E. N. Davies, “Optical coherence domain reflectometry: a new optical evaluation technique,” Opt. Lett. 12, 158-160 (1987).

[Yun03] S. H. Yun, G. J. Tearney, B. E. Bouma, B. H. Park, J. F. de Boer, “High-speed spectral-domain optical coherence tomography at 1.3 μm wavelength,” Opt. Express 11, 3598-3604 (2003).

[Yur10] G. Yurtsever, P. Dumon, W. Bogaerts, and R. Baets, “Integrated photonic circuit in silicon on insulator for Fourier domain optical coherence tomography,” Proc. SPIE, Optical Coherence Tomography and Coherence Domain Optical Methods in Biomedicine XIV, vol. 7554, San Francisco, CA, USA, 2010, pp. 1-5.

[Zah05] Z. Yaqoob, J. Wu, and C. Yang, “Spectral domain optical coherence tomography: a better OCT imaging strategy,” BioTechniques 39, S6-S13 (2005).

[Zir92] M. Zirngibl, C. Dragone, and C. H. Joyner, “Demonstration of a 15×15 arrayed waveguide multiplexer on InP,” IEEE Photon. Technol. Lett. 4, 1250–1253 (1992).

Acknowledgements

I am indebted to the following people for their contributions to this thesis:

To my supervisor Markus Pollnau for first of accepting me to his research group and providing me the financial support to carry out my PhD as well as helping me to improve my academic writing skills.

To my promoter, René M. de Ridder, who provided me with the kind of criticism, attention to detail, and support that took this thesis to a better level. He is not just a good scientist but also a very kind and thoughtful person.

To Alfred Driessen, for supervising me in my first year in a very effective and productive way.

To Kerstin Wörhoff for depositing SiON layers and for providing the answers on all things device fabrication.

To Fehmi Çivitçi, Nur Ismail, Lantian Chang, So van Pham, and Fei Sun for sharing their broad knowledge with me. Besides their great personalities, I owe this thesis to the fruitful discussions that we had. In particular I owe a special thank to my office mates Nur-the most humble scientist in IOMS- and So-the master of meditation- for their great support at all times. I would like to dedicate Chapter 5 to Lantian and Fehmi due to their great support and encouragements.

To the Laser subgroup members; Abu Shanmugam Aravazhi, Laura Agazzi, Edward Bernhardi, Dimitri Geskus, Marko van Dalfsen, Jonathan Bradley, Sergio Vázquez-Córdova, and Yean-Sheng Yong for their hospitality and kindness as well as for introducing me to the different cultures. In particular I owe a big thank to my ex-neighbors Edward and Laura for the unforgettable Italian cakes and South African hospitality.

To Anton Hollink, Meindert Dijkstra, and Gabriel Sengo for being always so kind and helpful to me. I am deeply saddened by the loss of Anton, he was the strongest person I have ever seen.. Rest in peace Anton, I will miss you so much…

To Sonia Garcia Blanco -the most positive person- for sharing her contagious positiveness with me..

To Manfred Hammer for his support in optical waveguide theory.

To Hugo Hoekstra for being so generous and kind to me. Without his financial support I couldn't be able to finalize my research.

To Günay Yurtsever for his invaluable helps which helped me to understand the OCT theory in a better way. Thanks a lot for your generosity and kindness Günay.

To Duc Van Nguyen for his kindness and technical support during our collaboration with Amsterdam Academic Medical Center. Despite the fact that I had the most difficult times in my PhD due to this collaboration, I would like to thank Prof. Ton van Leeuwen and Jeroen Kalkman as well for at least initiating the on-chip OCT project.

To Boris Považay for being so smart and humorous which helped me to solve the most difficult problems in a very quick and enjoyable way. I owe him a big thank.

To Christopher Doerr for the fruitful discussions that we made by email. I feel very lucky to meet such a generous, smart, and humble scientist.

To Prof. Wolfgang Drexler and his group members for their amazing hospitality during my stay in Vienna, it was the best collaboration one could ever image.

To Feridun Ay and Prof. Atilla Aydınlı for their great support at any time and any field of my life.

To the rest of my graduation committee members: Prof. Dr. Ir. Wiendelt Steenbergen and Assoc. Prof. Dr. Ir. Cees Otto from the University of Twente for their valuable effort spent reviewing this thesis.

To my friends; Michelle Bernhardi, Saara-Maarit Reijn, Maurizio Burla, Hao van der Bui, Buket Kaleli Kemaneci, Efe Kemaneci, Berk Gökberk, Pinar Santemiz, Hayrettin Gürkök, Muharrem Bayraktar, Mustafa Akın Sefünç, Seçkin Pulatkan, and Yakup Kılıç for their faithful friendships. With their amazing support I never felt alone in the Netherlands.

To my husband, Akın- my love and my greatest support. Every single word of this thesis is dedicated to you…I couldn't have made it without you, thank you for being in my life…

To my beloved parents and my siblings for their love and continuous support. Mom&dad thank you so much for being so wonderful, I dedicated my thesis to you..

Thank you all
İmran Akça
08.11.2012